HAL
open science

Structure électronique et transport quantique dans les nanostructures de Graphène

Omid Faizy Namarvar

To cite this version:

Omid Faizy Namarvar. Structure électronique et transport quantique dans les nanostructures de Graphène. Autre [cond-mat.other]. Université de Grenoble, 2012. Français. NNT : 2012GRENY031 . tel-00870405

HAL Id: tel-00870405

https://theses.hal.science/tel-00870405v1

Submitted on 7 Oct 2013

HAL is a multi-disciplinary open access archive for the deposit and dissemination of scientific research documents, whether they are published or not. The documents may come from teaching and research institutions in France or abroad, or from public or private research centers.

L'archive ouverte pluridisciplinaire **HAL**, est destinée au dépôt et à la diffusion de documents scientifiques de niveau recherche, publiés ou non, émanant des établissements d'enseignement et de recherche français ou étrangers, des laboratoires publics ou privés.

UNIVERSITÉ DE GRENOBLE

THÈSE

Pour obtenir le grade de

DOCTEUR DE L'UNIVERSITÉ DE GRENOBLE

Spécialité: **PHYSIQUE/PHYSIQUE DE MATIERE CONDENSEE & RAYONNEMENT**

Arrêté ministériel : 7 août 2006

Présentée par

Omid Faizy Namarvar

Thèse dirigée par Didier Mayou

préparée au sein de l'**Institut Néel, CNRS-UJF**
dans **l'École Doctorale de Physique de Grenoble**

Structure Electronique et Transport Quantique dans les Nanostructures de Graphène

Thèse soutenue publiquement le **20 Juillet 2012**,
devant le jury composé de :

Matthias Ernzerhof (Rapporteur)
Professeur, Université de Montréal
Laurent Simon (Rapporteur)
Directeur de Recherche, Institut de Sciences des Matériaux de Mulhouse
Annick Loiseau (Président)
Directeur de Recherche, LEM Chatillon
Didier Mayou (Directeur de thèse)
Directeur de Recherche, Institut Néel, Grenoble
Laurence Magaud (Membre)
Directeur de Recherche, Institut Néel, Grenoble
Guy Trambly de Laissardière (Membre)
Maître de Conférences, Université de Cergy-Pontoise

UNIVERSITÉ DE GRENOBLE

THÈSE

Pour obtenir le grade de

DOCTEUR DE L'UNIVERSITÉ DE GRENOBLE

Spécialité: **PHYSIQUE/PHYSIQUE DE MATIERE CONDENSEE & RAYONNEMENT**

Arrêté ministériel : 7 août 2006

Présentée par

Omid Faizy Namarvar

Thèse dirigée par Didier Mayou

préparée au sein de l'**Institut Néel, CNRS-UJF**
dans **l'École Doctorale de Physique de Grenoble**

Structure Electronique et Transport Quantique dans les Nanostructures de Graphène

Thèse soutenue publiquement le **20 Juillet 2012**,
devant le jury composé de :

Matthias Ernzerhof (Rapporteur)
Professeur, Université de Montréal
Laurent Simon (Rapporteur)
Directeur de Recherche, Institut de Sciences des Matériaux de Mulhouse
Annick Loiseau (Président)
Directeur de Recherche, LEM Chatillon
Didier Mayou (Directeur de thèse)
Directeur de Recherche, Institut Néel, Grenoble
Laurence Magaud (Membre)
Directeur de Recherche, Institut Néel, Grenoble
Guy Trambly de Laissardière (Membre)
Maître de Conférences, Université de Cergy-Pontoise

To the memory of my grandfather,

El-haj Mohammad Faizy Namarvar

ACKNOWLEDGEMENTS

I thank the director of the Institut Néel, Prof. Alain Schuhl and also the former director, Dr. Alain Fontaine. I thank also the head of our department (MCMF) Dr. Alain Ibanez and the former head Prof. Benoît Boulanger. I thank the Nanosciences Fondation for the financial support of this thesis. I should thank ”Ecole Doctorale de Physique”, especially its director, Prof. Frank Hekking, for offering great courses during my thesis.

I would like to express my warmest thanks to my supervisor Dr. Didier Mayou, you have been a great director for me. I would like to thank you for orienting my research and for letting me grow as a research scientist.

I would also like to thank my committee members; Dr. Annick Loiseau, Dr. Laurence Magaud, Professor Matthias Ernzerhof, Dr. Laurent Simon and Dr. Guy Trambly de Laissardière. I want to thank you for letting my defense to be an enjoyable moment, and for your comments and suggestions.

I would especially like to thank again Dr. Guy Trambly de Laissardière for his strong instructions for working with numerical codes. Also I thank Dr. Claudio Attaccalite, Pouya Sabouri and Dr. Dan-Gabriel Calugaru for their kind helps on computational and IT problems.

I would like to thank my dear wife Hoda for her personal support and great patience at all times and thank for her understanding and love during the past few years. My kind wife is my source of strength and without her support this thesis would never have started much less finished.

I thank especially my kind parents who have given me their unequivocal support throughout, as always, for which my mere expression of thanks likewise does not suffice. Words can not express how grateful I am to my parents for all of the sacrifices that they have made on my behalf. I thank my dude brothers, Morteza and Mostafa and our new family member, my nephew, little Ayhan. I should thank also my wife's family for the kind support they provided us through our marriage. I would like to thank very much Didiers family, his nice wife Pascale and his lovely daughter Shadika, we had great moments with them.

I thank my friends in Grenoble, Iraj Hosseini and his family, Hadi Arjmandi and Mostafa Tahmasebi. I remember also my best friends; Amir Niazi, Behrad Kaleibary, Ahad Ebrahimzadeh, Reza Najafi, Abbas Delraz, Mohammad Barzgari, Masoud Talebi and Mir Mohammad Damadi.

Finally I thank my God, good Father, devoted Mother and my wife Hoda again, for helping me through all the difficulties.

TABLE OF CONTENTS

DEDICATION ii

ACKNOWLEDGEMENTS iii

LIST OF FIGURES viii

ABSTRACT xv

CHAPTER

I. Introduction to the Electronic Structure of Graphene 1

1.1 Preface 1
1.2 Chemistry 4
1.3 The Crystal and Band Structure 10
1.3.1 Graphene's honeycomb lattice 10
1.4 Electronic properties and Band Structure of Graphene 14
1.4.1 Tight-Binding Model for Electrons on Honeycomb Lattice 14
1.5 Tight-Binding Model of Monolayer Graphene 17
1.5.1 Diagonal Matrix Elements 18
1.5.2 Off-Diagonal Matrix Elements 20
1.5.3 The Low-Energy Electronic Bands of Monolayer Graphene 23
1.5.4 Density of States 27
1.6 Massless Chiral Quasiparticles in Monolayer Graphene 31
1.6.1 The Dirac-Like Hamilitonian 31
1.6.2 Pseudospin and Chirality in Graphene 34
1.7 Chiral tunneling and Klein paradox in Graphene 37

II. Electronic Structure of twisted double-layer Graphene 45

2.1 Introduction 46
2.1.1 Stacking Arrangements 46
2.2 The Tight-Binding Model of AA and AB Bilayers of Graphene . 47
2.3 Rotated Bilayer Graphene 54
2.3.1 Rotationaly Stacked Commensurate Bilayers 56
2.4 Tight-Binding Model and Hamiltonian 58
2.5 Velocity renormalization and electron life time 63
2.5.1 Velocity renormalization 65
2.5.2 Electron lifetime 68
2.6 Density of States 69

III. QuantumTransport in Graphene Nanostructures 78

3.1 Introduction to Bulk Transport 79
3.1.1 Drude Model 80
3.1.2 Resistance, coherent and incoherent transport 82
3.1.3 Introduction to Kubo formalism 84
3.1.4 Conductivity and dissipation 85
3.1.5 Conductivity and quantum diffusion 88
3.2 Transport in rotated bilayer 89
3.2.1 Introduction 89
3.2.2 Monolayer of Graphene 90
3.2.3 Main results 91
3.2.4 Model and discussion 95
3.3 Landauer approach 98
3.3.1 Green's Function and Fisher-Lee Formula 101
3.4 Anomalous STM images of resonant states on Graphene 105
3.4.1 Model 106
3.4.2 General trends 109
3.4.3 Numerical studies and discussion 111

IV. Adsorbates on Graphene 119

4.1 Introduction 119
4.2 Formalism for Adsorbates on Graphene and Dirac Point Resonances 121

4.2.1 Tight Binding Hamiltonian for Adsorbates on Graphene 122
4.2.2 Effective Hamiltonian for Adsorbates on Graphene . . 123
4.2.3 The $\mathcal{T}$-Matrix Formalism 124
4.3 Density of states around an adsorbate 127
4.3.1 Green's function of the host (graphene) 127
4.3.2 Spatial Variation of the DOS 130
4.4 Charge Transfer and the Electrostatic Potential around adsorbate 131

APPENDICES 137
A.1 Green's Functions 139
A.1.1 Green's Functions for the Schrödinger equation 140
A.1.2 Some properties of Green's functions 143
A.1.3 Green's function and density of states 144
A.2 Multiple scattering expansion 146
A.2.1 Dyson equation 146
A.2.2 Self-Energy 149
B.1 Tight-Binding Model and Hamiltonian 152
B.2 Effective Hamiltonian: 155
B.3 Self-Energy 158
B.4 Calculations of DOS 163

LIST OF FIGURES

Figure

1.1 sp hybridization. The shading denotes the negative amplitude of the wave function. $|2s\rangle + |2p_x\rangle$ is elongated in the positive direction of x. From [34] 5

1.2 sp^2 (left) and sp^3 (right) hybridized orbitals 6

1.3 Energy of the hybridized $s - p$ states, in blue (top curve) we show the energy of the π state, (1.3), and in red (bottom curve) the energy of the σ state, (1.6), as a function of the hybridization parameter A. $A = 0$ corresponds to the sp^2 and $A = 1/2$ corresponds to the sp^3 configuration. From [12] 8

1.4 Basic hypridization energies for $s-p$ bonds: (**a**) $V_{ss\sigma}$, (**b**) $V_{sp\sigma}$, (**c**) $V_{pp\sigma}$, (**d**)$V_{pp\pi}$. From [12] 9

1.5 Calculation of the hybridization of two $s-p$ orbitals in terms of the basic hybridization energies shown in Fig 1.4 .Adopted from [12] 10

1.6 (a) Honeycomb lattice. The vectors $\boldsymbol{\delta}_1, \boldsymbol{\delta}_2$ and $\boldsymbol{\delta}_3$ connect nn carbon atoms, separated by a distance $a = 0.142nm$. The vectors $\mathbf{a}_1$ and $\mathbf{a}_2$ are basis vectors of the tri- angular Bravais lattice. (b) Reciprocal lattice of the triangular lattice. Its primitive lattice vectors are $\mathbf{b}_1 = \mathbf{a}_1^*$ and $\mathbf{b}_2 = \mathbf{a}_2^*$. The shaded region represents the first Brillouin zone (BZ), with its centre Γ and the two inequivalent corners K (black squares) and K' (white squares). The thick part of the border of the first BZ represents those points which are counted in the definition such that no points are doubly counted. The first BZ, defined in a strict manner, is, thus, the shaded region plus the thick part of the border. For completeness, it is shown the three inequivalent cristallographic points M, M', and M'' (white triangles). 11

1.7 The honeycomb crystal structure of monolayer graphene. In the nearest-neighbor approximation, one can consider hopping from an A site (white) to three adjacent B sites (black), labeled B_1, B_2, B_3, with position vectors $\boldsymbol{\delta}_1, \boldsymbol{\delta}_2, \boldsymbol{\delta}_3$ respectively, relative to the A site 21
1.8 The low-energy band structure of monolayer graphene (1.57) taking into account nearest-neighbor hopping with parameter $\gamma_0 = 3.033$ eV, nearest-neighbor overlap parameter $s_0 = 0.129$, and orbital energy $s_0 = 0.129$ [11]. The plot shows the bands calculated in the vicinity of the first Brillouin zone, with conduction and valence bands touching at six corners of the Brillouin zone, two of them are labeled K_+ and K_- . Label Γ indicates the center of the Brillouin zone. Adopted from[27] 25
1.9 The low-energy band structure of monolayer graphene (1.57) taking into account nearest-neighbor hopping with parameter $\gamma_0 = 3.033$ eV, nearest-neighbor overlap parameter $s_0 = 0.129$, and orbital energy $s_0 = 0.129$ [14]. The plot shows a cut through the band structure Fig. 1.7, plotted along the k_x axis intersecting points K_- , Γ , and K_+ in the Brillouin zone, shown as the dotted line in the inset 26
1.10 (a) Graphene band structure. (b) Enlargment of the band structure close to the K and K' points showing the Dirac cones. Adpated from Wilson, 2006 [17] 27
1.11 Density of states per unit cell as a function of energy (in units of γ_0) . Also shown is a zoom-in of the density of states close to the neutrality point of one electron per site. For the case γ'(second-nearest hopping)=0, the electron-hole nature of the spectrum is apparent and the density of states close to the neutrality point can be approximated by $\rho(\epsilon) \propto |\epsilon|$ 30
1.12 Schematic representation of the pseudospin degree of freedom: (**a**) electronic density solely on the A sublattice can be viewed as a pseudospin up state, whereas (**b**) density solely on the B sublattice corresponds to a pseudospin down state; (**c**) in graphene, electronic density is usually shared equally between A and B sublattices, so that the pseudospin part of the wave function is a linear combination of up and down, with amplitudes dependent on the direction of the electronic momentum **p**; (**d**) at valley K_+, the pseudospin $\langle \boldsymbol{\sigma} \rangle_e$ in the conduction band is parallel to the momentum, whereas the pseudospin $\langle \boldsymbol{\sigma} \rangle_h$ in the valence band is anti-parallel to the momentum. Adopted from [27] 36

1.13 Anisotropic scattering of chiral electrons in graphene: (**a**) angular dependence $w(\varphi) = \cos^2(\varphi/2)$ of the scattering probability off an A-B symmetric potential in monolayer graphene and (**b**) $w(\varphi) = \cos^2(\varphi)$ in bilayer graphene. From [27] 37
1.14 Klein tunneling in graphene. Top: schematic of the scattering of Dirac electrons by a square potential. Bottom: definition of the angles ϕ and θ used in the scattering formalism in regions I,II, and III (adapted from [31]). 39
1.15 **Klein-like quantum tunnelling in graphene systems:** Transmission probability T through a 100-nm-wide barrier as a function of the incident angle for single- (**a**) and bi-layer (**b**) graphene. The electron concentration n outside the barrier is chosen as 0.5×10^{12} cm^2 for all cases. Inside the barrier, hole concentrations p are 1×10^{12} and 3×10^{12} cm^2 for red and blue curves, respectively (such concentrations are most typical in experiments with graphene). This corresponds to the Fermi energy E of incident electrons $\approx$ 80 and 17meV for single- and bi-layer graphene, respectively, and $\lambda \approx 50nm$. The barrier heights V_0 are (**a**) 200 and (**b**) 50 meV (red curves) and (**a**) 285and (**b**) 100meV (blue curves). [adopted from Katsnelson et al. [29] 41
2.1 (**a**) Three distinct stacking arrangements A, B and C in multilayer graphene and representative sublattices α and β in the A, B, and C layers. (**b**) The stacking triangle where each added layer cycles around. From [56] . . . 47
2.2 (a) The geometric structure, (b) the first Brillouim zone and (c) the low-lying sub bands of AA-stacked graphene. α_0= 2.598 eV is the nearest-neighbor hopping integral and two important interlayer interactions are α_1= 0.361eV and α_3 = -0.032 eV . From [55] 48
2.3 Ab initio (black curves) and tight-binding (red curves) band structure along $K\Gamma MK$ of (a) graphene and (c) AA-stacked. Corresponding energy dispersion around the K point for (b) graphene, (d) and AA-stacked bilayer. From [58] 49
2.4 Schematic representation of the crystal structure of AB-stacked bilayer graphene: (**a**) plan view with $A1$ (white) and $B1$ atoms (black) on the lower layer, $A2$ (black) and $B2$ atoms (gray) on the upper layer. Vectors $\mathbf{a}_1$ and $\mathbf{a}_2$ are primitive lattice vectors of length equal to the lattice constant a, and the shaded rhombus is a unit cell; (**b**) side view where the parameter γ_0 shows nearest-neighbor coupling within each layer, γ_1 nearest-neighbor coupling between the $B1$ and $A2$ atoms on different layers. From [57] 51

2.5 The low-energy band structure of bilayer graphene taking into account nearest-neighbor hopping with parameter $\gamma_0 = 3.033$ eV, nearest-neighbor overlap parameter $s_0 = 0.129$, orbital energy $\epsilon_{2p} = 0$ [11], and interlayer coupling $\gamma_1 = 0.39$ eV. The plot shows the bands calculated along the k_x axis intersecting points K_-, Γ , and K_+ in the Brillouin zone, shown as the dotted line in the right inset. The left inset shows the band structure in the vicinity of the point K_- . From [57] 53
2.6 Commensurate cell vectors of (n, m) bilayer: 57
2.7 Moiré pattern for small θ ($\theta \leq 10°$) left: (6.7) bilayer: $\theta = 5.08°$, $N = 508$ atoms; right: (5.9) bilayer: $\theta = 18.73°$, $N = 604$ atoms. Full (dashed) line circle AB (AA) region. 58
2.8 Commensurate bilayer cell $(n, m) = (5, 9)$ for a rotation of $\theta = 18.73°$. . 59
2.9 Modulus of the inter-layer coupling in versus modulus of the wave-vector 63
2.10 Velocity ratio $v_b i/v_{\text{mono}}$ for a commensurate (n, m) bilayer cell versus rotation angle θ: Red circles: VASP calculations by Laurence Magaud, cross: TB calculations by Guy Trambly de Laissardière, the blue line is the model of Lopez dos Santos et al.: $v_b i/v_{\text{mono}} = 1-9[\tilde{t}/(v_{\text{mono}}K\ \sin(\theta/2))]$, with $\tilde{t} = 0.11$eV and $v_{\text{mono}}K = 2\sqrt{3}\gamma_0\pi = 9.8$ eV . From [50]. And the green line is our model. 67
2.11 Relative variation of the LDOS on top layer for two angles. Tight-binding results are in the top and corresponding analytical results are below. 71
2.12 3D relative variation of DOS $\frac{\Delta\rho(E,\vec{R})}{\rho(E)}$. The green and red points correspond to A and B atoms with a difference of about ±15%. Blue points corresponds to our analytical model which reproduce the average values of relative variation of DOSs on A and B atoms. 72
3.1 Diffusivity $D = X^2(E, t)/t$ versus time t for $E = 0.1$eV. The angles corresponding to the different bilayers are $\theta(3, 4) = 9.54°$, $\theta(6, 7) = 5.09°$, $\theta(8, 9) = 3.89°$, $\theta(12, 13) = 2.65°$ 92
3.2 DOS in the bilayer and in the monolayer with pure or defect (1% vacancy) in the one layer. The angles corresponding to the different bilayers are $\theta(3, 4) = 9.54°$, $\theta(6, 7) = 5.09°$, $\theta(8, 9) = 3.89°$, $\theta(12, 13) = 2.65°$ 93
3.3 Conductivity in the bilayer and in the monolayer with pure or defect (1% vacancy) in the one layer. The angles corresponding to the different bilayers are $\theta(3, 4) = 9.54°$, $\theta(6, 7) = 5.09°$, $\theta(8, 9) = 3.89°$, $\theta(12, 13) = 2.65°$ 94

3.4 Conductivity in rotated bilayer versus the squared angle in degree for different energies: (a) E= -0.05 eV, (b)E=-0.1 eV, (c) E=0.25 eV and (d) E= 0.3 eV 96
3.5 Wave guide geometry used in the Landauer formalism. The disordered conductor of length L and section $S = W^{d-1}$ is perfectly connected to ideal leads defined as wave guides propagating incoming, reflected and transmitted plane waves. 99
3.6 A unit impulse in lead p generates an incident wave which is partially transmitted to each of other leads. Taken from [9] 101
3.7 Mapping of a real $3D$ device (top: hydrogen molecule in between gold leads) into the effective $1D$ system (bottom: effective atomic chain). The *effective channels* arise from the central device (here the hydrogen molecule) and pursue into a nonballistic section (blue, violet, and red pseudoatoms), until they achieve an asymptotic ballistic behaviour (yellow). Taken from [14] 103
3.8 Logarithm of the conductance G in units of $\frac{2e^2}{h}$ as a function of distance for different models [15]. $G = \frac{2e^2}{h}T$ where T is the transmission. At large distances the transmission decreases exponentially with distance between the tip and the surface. At short distance the transmission is close to 1. Picture is taken from [15] 106
3.9 our schematic model of STM tip approaching on adatom. 107
3.10 Two different models of adsorbate on graphene. One is representative of an adsorbate in a top position where the adsorbate is right above one carbon (Fig left). The other model is representative of an adsorbate in a hollow position (Fig right). In that case the adsorbate is right above the center of an hexagon of carbon atoms. 112
3.11 (TOP POSITION) DOS of the adsorbate without STM for the case of an adatom on top position, for different values of onsite energy (a) ϵ_d = 0.26eV and (b) ϵ_d = 0.0eV. Transmission T for the case of an adatom on top position for different values of coupling x between the apex atom of the tip and the adatom (c) on-site energy ϵ_d = 0.26eV and (d) ϵ_d = 0.0. Here different colors corresponds to different values of x as *red* $\equiv x =$ 0.01eV, *blue* $\equiv x =$ 0.1eV, *green* $\equiv x =$ 0.5eV and *yellow* $\equiv x =$ 1.0eV, . 113

3.12 (HOLLOW POSITION) DOS of the adsorbate without STM for the case of an adatom in a hollow position for different values of on-site energy (a) ϵ_d = 0.0eV and (b) ϵ_d = 0.26eV. Transmission T for the case of adatom in a hollow for different values of coupling x between the apex orbital of the tip and the adatom (c) on-site energy ϵ_d = 0.0eV and (d) ϵ_d = 0.260. Here different colors corresponds to different values of x as *red* $\equiv$ x = 0.01eV, *blue* $\equiv$ x = 0.1eV, *green* $\equiv$ x = 0.5eV and *yellow* $\equiv$ x = 1.0eV,. 114
3.13 (METALLIC SUBSTRATE) DOS of the adsorbate without STM (a) and the transmission (b) for the case of metallic substrate here we take $\epsilon_d = 0$. 116
4.1 Relaxed geometries of adsorbates on graphene. C, H, F, and O atoms are black, blue, green, and red respectively (a) Adsorbed hydrogen atom. H and C atoms to which H binds are 1.47 and 0.35 Å above graphene plane. (b) Adsorbed fluorine. F and C atoms to which F binds are 1.83 and 0.36 Å above graphene plane. (c) Adsorbed hydroxyl group. H, O, and C atoms to which O binds are 2.78, 1.83, and 0.41 Å above graphene plane. (d) Adsorbed oxygen. O and C atoms to which O binds are 1.51 and 0.27 Å above graphene plane. The C atoms to which the O binds are separated by 1.47 Å . The x axis is parallel to the line joining the C atoms to which the O binds. Adopted from [2] 121
4.2 Calculated square modulus of the $\mathcal{T}$ -matrix vs. electron energy ϵ for an H, F, or O atom or OH group adsorbed on graphene in the geometries shown in Fig. 4.1. $\mathcal{T}$ and ϵ are in units of t = 2.7 eV. The Dirac point of graphene is at $\epsilon = 0$. For H, F, and OH $\mathcal{T} = \langle 1|\mathcal{T}|1\rangle$. For O the square of the Frobenius norm of the matrix $\mathcal{T} = \langle m|\mathcal{T}|n\rangle$ is plotted. The EMOs included in this calculation are linear combinations of the atomic valence orbitals of the adsorbed species and the $2s$, $2p_x$, and $2p_y$ valence orbitals of each of the carbon atoms shown in Fig. 4.1 for the respective adsorbed species. Thus the local rehybridization of the graphene from the sp^2 to sp^3 bonding is included in the model. The overlaps $\sigma_{\alpha j}$ between the EMOs and the $2p_z$ orbitals of the carbon atoms to which the adsorbed moieties bond are included in the calculations. Taken from [2] 126
4.3 The spatial variation of charge per unit cell area versus distance (unit of Angstrom) from Hydrogen adatom in graphene sheet ($\varepsilon_d = 0.26eV$ all the parameters are in the text). 133
4.4 The spatial variation of average electrostatic potential in eV versus in-plane distance from Hydrogen adsorbate 134

A.1 Convention employed in this book for the representation of Greens functions. We take $\mathcal{G}^A(\boldsymbol{r}', \boldsymbol{r}) = \mathcal{G}^R(\boldsymbol{r}, \boldsymbol{r}')^*$ 140
A.2 Diagrammatic expansion of the Green function before averaging over disorder[From [1]] 147
A.3 Diagrammatic expansion of the average Green function. From [1] . . . 147
A.4 Diagrammatic expansion of the self-energy as a sum of irreducible diagrams . From [1] 149
C.1 Scattered wave after interaction with the potential at point $\boldsymbol{r}'$. In the Fraunhoffer approximation, we have $|\boldsymbol{r}'| \ll |\boldsymbol{r}|$ 169
C.2 Scattering by a localized potential. The total flux $F = F_{int} + F_{out} + F_s$ crossing the surface S is zero. Since $F_{in} = \int \boldsymbol{k} \cdot dS = 0$ must vanish. This result constitutes the optical theorem [adopted form [1]] 170
C.3 (a) In the Born approximation, the wave interacts with the potential only once. (b) Beyond this approximation, the wave is scattered many times by the potential 176

Introduction

En 2004-2005 une nouvelle ére en science des matériaux a débuté avec l'avènement du graphène. Le graphène est un matériau constitué d'une couche atomique d'atome de carbone en hybridation sp^2 dans un réseau nid d'abeille. Le graphène possède des propriétés physiques remarquables: c'est le matériau le plus resistant, il possède une conductivité thermique record et une très haute mobilité électronique. Les porteurs de charge sont des fermions de Dirac sans masse qui présentent une conductivité minimale près du point de Dirac, un effet Hall quantique anormal, un effet tunnel prsentant le paradoxe de Klein, une conductivité optique universelle Le graphène offre de nombreuses perspectives pour différentes applications : encre conductrice, transistors terahertz, ecrans flexibles, photodetecteurs ultra rapide etc..Cette thèse concerne la structure électronique et le transport lectronique dans certaines nanostructures produites avec le graphène.

Nous considérons en particulier le cas des bicouches tournées de graphène. Ces systèmes ont été dcouverts en particulier dans le graphène produit sur le carbure de silicium et présentent des propriétés originales par rapport aux bicouches dans l' empilement AB qui existe par exemple dans le graphite. Nous analysons au moyen d'une thorie perturbative et aussi par des approches numériques la densité d'états dans ces systémes.Nous montrons que la densité d'états présente des oscillations avec la même période que celle du Moiré produit par ces bicouches. Nous analysons aussi le rôle des défauts sur les propriétés de transport en particulier dans le cas ou les défauts sont répartis uniquement sur une des deux couches. Ici aussi notre approche combine théorie perturbative du couplage interplans et approches purement numérique en liaisons fortes.

Nous considérons aussi le role joué par les adatomes comme l'hydrogène par exemple. Nous analysons la modification de la densité d'états induite autour de l'adatome et les variations correspondantes de densité de charge et de potentiel électrostatique. Ces systèmes tendent à produire des états resonants près de l'énergie de Dirac qui dependent beaucoup aussi de la position top ou hollow de l' adsorbat. Pour des orbitales de type "s" la resonance est plus marquée si l'adatome est en position hollow. Nous montrons que limage par experience STM (microscopie à effet tunnel) depend beaucoup de la distance entre l'adsorbat et la pointe du STM. Dans un régime de champ proche la résonance de l'adsorbat peut même apparaître comme un creux dans le signal dI/dV du STM.

La thése comprend 4 chapitres et trois appendices organisés comme suit:

Le premier chapitre présente une introduction à quelques propriétés fondamentales du graphène. Après une brève description de la structure cristallographique nous présentons une description chimique de l'hybridation et des bandes du graphène. Nous dérivons la structure de bande dans l'espace réciproque. Nous présentons aussi la description continue de la structure électronique avec l'équation de Dirac qui est valable près des points de Dirac. Nous terminons par une description de l'effet tunnel et du paradoxe de Klein.

Dans le second chapitre nous considérons les biplans tournés de graphène. Le biplan standard est le biplan en empilement Bernal (AB) tel qu'on peut le trouver dans le graphite. Un autre arrangement possible est l'empilement AA où les deux plans sont en exact superposition. Cependant lors des 4-5 dernières années il a été reconnu par la communauté scientifique que les biplans tournés existent aussi notamment dans le graphène épitaxié sur le carbure de silicium. Ces biplans tournés constituent maintenant une structure élémentaire importante dans le monde du graphène. Ils peuvent être décrits géométriquement en par-

tant d'un biplan AA et en effectuant une translation et une rotation dun angle θ. Cependant les propriétés de ces biplans dependent essentiellement de l'angle de rotation θ et faiblement de la translation. Dans un biplan tourné la superposition des deux plans engendre un Moiré avec une période longue inversement proportionelle à l'angle, de 14 nanomètres pour un angle de 1degré. Pour un angle assez faible $\theta \leq 15°$ on peut identifier des zones localement AB et localement AA.

Dans une première étape nous calculons le Hamiltonien de couplage entre états des deux plans tournés. A partir de ce couplage nous pouvons calculer en théorie de perturbation la self-energy et la densité d'états dans un plan en fonction de la position. Les calculs analytiques sont présentés en detail dans l'appendice B et le chapitre 2 détaille surtout la discussion physique des résultats.

Dans le troisiéme chapitre nous considérons les phénoménes de transport pour les deux systèmes étudiés dans cette thèse : biplans tournés et adatomes présentant une resonance prés du point de Dirac. Nous présentons rapidement le formalisme de Kubo et le formalisme de Landauer.

Nous discutons les propriétés de transport de biplans tournés en particulier dans le cas où le dsordre se trouve sur un seul des deux plans. En utilisant la self-energy calculée dans le chapitre 2 nous estimons la conductivité par une formule simple. Cette formule se compare bien à des résultats numériques en liaisons fortes.

Nous analysons aussi le cas de l'image STM pour un état resonant produit par un adsorbat du graphène. Nous considrons le cas ou la pointe STM s'approche de l'adsorbat. Dans ce régime de champ proche la théorie usuelle perturbative ne s'applique plus et le signal STM ne représente plus la densité d'état locale. Au lieu de celà nous trouvons que

la transmission T(E) en fonction de l'énergie peut presenter un creux au lieu d'une amplification près de l'énergie de la résonance. Nous comparons aussi deux cas correspondant à un adatome en position top ou hollow. La résonance est plus marquée en position hollow et en consequence l'effet d'antiresonance à courte distance est aussi plus marqué.

Dans le quatrième chapitre nous considérons le probléme d'impuretés résonantes (par exemple l'hydrogéne). Nous considérons un atome en position top c'est à dire à la vertical d'un atome de carbone Deux paramètres importants sont l'énergie de site de l'orbitale de l'adatome et son intégrale de saut avec l'atome de carbone immédiatement dessous. Notre objectif principal ici est de discuter le transfert de charge et le potentiel électrostatique qu'il engendre. Nous utilisons des résultats récents sur la fonction de Green non diagonale sur les adsorbats pour calculer la modification de la densité d'états et la charge résultante ainsi que le potentiel. Nous présentons les premiers résultats obtenus par notre approche en modèle continu.

Finalement la thèse comporte aussi trois appendices.

L'appendice A introduit les concepts de base de la théorie de perturbation pour les fonctions de Green et la self-energy, dans le problème de la diffusion multiple par des impuretés.

L'appendice B présente de façon détaillée les calculs fort longs concernant le chapitre 2 : calcul de la self-energy et surtout calcul perturbatif de la densité d'états.

L'appendice C introduit les concepts fondamentaux de la théorie de la diffusion qui sont utiles pour le chapitre 4

Introduction

In 2004-2005 a new era in the material science was opened: the era of graphene or, more generally, of two-dimensional materials. Graphene is the one-atom thin layer of sp^2 bonded carbon atoms arranged in a honeycomb lattice. It possesses unique physical properties: graphene is the strongest and the most stretchable known material, has the record thermal conductivity and the very high intrinsic mobility and is completely impermeable. The charge carriers in graphene are massless Dirac fermions and its unique electronic structure leads to a number of interesting physical effects, such as the minimal electrical conductivity, anomalous quantum Hall effect, Klein tunneling, the universal optical conductivity and the strong nonlinear electro- magnetic response. Graphene offers and promises a lot of different applications, including conductive ink, terahertz transistors, ultrafast photodetectors, bendable touch screens, strain tensors and many others. Nowadays, graphene is in the focus of research activity of condensed matter physicists in the whole world. This thesis deals with some properties of electronic structure and electronic transport in graphene.

We consider in particular the case of twisted bilayers of graphene. These systems have been discovered especially in graphene produced on Silicon Carbide and present original properties when compared with standard AB bilayers that occur for example in graphite. We analyze by perturbative theory and by numerical methods the density of states. We show that the electronic density of states presents periodic oscillations with the period of the geometric Moiré produced by these systems. We analyze also the role of defects on transport properties and in particular we consider the case where the defects are only in

one layer. We discuss how defects on this layer affects the conductivity of the bilayer. Here also we use simple analytical models and numerical approaches.

We consider also the role played by atomic impurities like Hydrogen adatom on the graphene plane. We analyze the modification of density of states induced around the adatom and the corresponding modifications of charge density and electrostatic potential. These systems tend to produce a resonant state close to the Dirac energy which depends much on whether the adatom is in a top or hollow position. For hydrogen like orbital (s orbital) the resonance is stronger in the hollow position. We show that the image obtained through STM experiments for these resonant state depends very much on the distance of the STM tip to the adatom. In a near field regime the resonance can even appear as a dip in the STM signal dI/dV.

The thesis contains four chapters and three appendixes which are organized as follows :

In the first chapter we present an introduction to some fundamental physical properties of Graphene. After a brief description of the crystalline structure we use elementary chemistry and hybridization description of bands in Graphene. We derive the band structure of Graphene and its representation in reciprocal lattice. We present also the Dirac equation which is a continuum description of the band structure valid close to the Dirac points (low energy description). We end by a description of chiral tunneling and Klein paradox in Graphene.

In the second chapter we consider twisted bilayers of graphene. The standard bilayer of Graphene is the Bernal stacking which is the so-called A-B bilayer that occurs in graphite. Another possible arrangement is the AA stacking, where the two lattices are

in exact superposition. However, during the last 4-5 years, it has been recognized by the scientic community that bilayers consisting of two rotated layers also occur, especially in epitaxial Graphene. These rotated bilayers represent an important elementary structure in the Graphene world. They can be obtained starting from a AA bilayer by performing a translation and a rotation of an angle θ. Yet the properties of these bilayers depend essentially on the angle θ and weakly on the translation.In a rotated bilayer the superposition of the two honeycomb lattices generates a Moiré pattern with a longer period. An important feature of this system is the emergence, for $\theta \leq 15°$ of a so-called Moiré pattern. This is a hexagonal interference pattern, consisting of regions of locally AA and AB stacking, the periodicity of which represents a new structural length scale of the system. At rst step, we calculate the coupling Hamiltonian between states of two layers by using the tight-binding method and its parametrization found from previous works of the group at Institut Nel. From this coupling between the two planes we get general relation for modulation of density of states (Moiré Pattern) and also self-energy. The detailed calculations are presented in appendix B and chapter 2 focuses mainly on the physical discussion of the models and of the results.

The third chapter deals specifically with transport phenomenon in our two basic systems : graphene bilayers and graphene with adatoms presenting usually a resonant state. We have briefly reviewed at first Kubo and Landauer transport theories as well as some semi-classical models.

We discuss transport properties of twisted graphene especially in the case where disorder is only in one layer. By using the self-energy formula which we calculated in second chapter we get an estimate of the conductivity which we compare with numerical calcula-

tions of quantum diffusion. In particular we discuss the role of the rotation angle θ on the conductivity of the bilayer.

We analyze theoretically the STM images of a resonant state of an Adsorbate on graphene . We consider the case where the STM tip comes close to the adatom on the surface of Graphene. In this near-field regime the standard perturbative theory of the STM signal is not valid and we show that the STM image does not represent the local density of states. Instead we find that the resonance of the transmission $T(E)$ as a function of the energy of states E, which is characteristic of a resonant state, can be replaced by a dip as a function of the energy (anti-resonance). We compare also two cases corresponding to adatom in a top position (i.e. right above a carbon atom) and adatom in a hollow position (i.e. right above the center of an hexagon).

Chapter four is about impurity problem on Graphene. We consider an adatom on graphene in a top position. This adatom as one s-orbital like Hydrogen for example. Two important parameters are the on-site energy of the s-orbital and the coupling parameter between the s-orbital and the carbon atom right below. Our main objective is to discuss the charge transfer and electrostatic potential around this impurity. To this end we start from some recent works about adsorbates on Graphene, to calculate spatial variation of Density of States around impurity. This allows to have some first results for the variation of electrostatic potential generated by this density of states around impurity.

Finally three appendixes are included at the end of the document. Appendix A introduces some basic concepts of perturbation theory such as Greens function and self-energy on the example of multiple scattering by impurities. Appendix B presents the detailed and quite long, calculations regarding chapter two on rotated bilayers. This allows us to

focus chapter two on the main physical aspects of the model and the on the main consequences for electronic structure. Appendix C is about scattering theory and introduces some fundamentals concept such as the T matrix that are used especially in chapter four.

CHAPTER I

Introduction to the Electronic Structure of Graphene

Abstract Graphene research is currently a tremendous field in condensed matter. Due to its peculiar electronic spectrum with Dirac-like quasiparticles, and the actuality that it is a unique example of one atom thick membrane, Graphene has properties that have no match in standard solid-state textbooks. We introduce the special aspects of the physics/-chemistry of carbon that affect the properties of Graphene; the basic features of Graphene's band structure including the π and σ bands.

1.1 Preface

Graphene, a one thick carbon material, has created a prodigious interest in the condensed matter community and in the media since its isolation in 2004 [1]. On the one hand, Graphene has unique properties that derive from its hexagonal lattice structure such as the Dirac-like spectrum (that mimics effects of matter under extreme conditions), its low dimensionality (that leads to enhanced quantum and thermal fluctuations), and its membrane-like nature (that mixes aspects of soft and hard condensed matter). More-

over, because of the strength and specificity of its covalent bonds, Graphene is one of the strongest materials in nature (albeit one of the softest), with literally none extrinsic substitutional impurities, leading to the highest electronic mobilities among metals and semiconductors [2]. Accordingly, Graphene is being considered for plenty of applications that range from conducting paints, and flexible displays, to high speed electronics. Actually, it can be said that possibly, not since the invention of the transistor out of germanium in the 1950s, a material has had this kind of impact in the solid-state literature. Nevertheless, unlike ordinary semiconductors such as germanium, gallium-arsenide, and silicon, Graphenes unusual properties have to be understood before it can really have an impact in technological applications.

Any material has a hierarchy of energy scales that range from the atomic physics ($\approx 10eV$), to many-body effects ($\approx 10^{-3}eV$).To understand the behavior of a material it is necessary to understand how these different energy scales influence its macroscopic properties. While structural properties such as strength against strain, shear and bending may depend on the covalent bonds formed by the atoms, magnetism and superconductivity are ruled by the particular way electrons interact with each other through Coulomb forces. Besides, while the properties of metals and semiconductors depend on the physics close to the Fermi energy (a direct consequence of Paulis exclusion principle), the nature of the vibrational spectrum depends on the particular way ions interact among themselves and how the electrons screen these interactions.

One of the abundant achievements of the application of quantum mechanics to the theory of metals is the understanding that while different materials can be structurally very different from each other, their long-wavelength and low-energy physics is basically iden-

tical and depend on very few parameters. This so-called renormalization towards the Fermi energy [3] is one of the biggest theoretical accomplishments of the twentieth century and is the basis of Landau's theory of the Fermi liquid [4]. In systems where the low-energy physics is governed by Galilean invariance the most significant parameter is the effective mass of the carriers that acts as to generate a scale from which it is possible to compute most of the substantial physical quantities such as specific heat, magnetic susceptibility, electronic compressibility, and so on. The most fundamental difference between Graphene and other materials is that its low-energy physics is not Galilean invariant, but instead Lorentz invariant, just like systems in particle and high-energy physics with Dirac particles as elementary excitations [5]. In this case, the renormalization towards the Fermi energy is dissimilar from other materials [6] because, in the absence of a mass (which in Graphene means the absence of a gap in the electronic spectrum), all physical quantities depend on a characteristic effective velocity that plays a role analogous to the speed of light plays in relativistic quantum mechanics. Nevertheless, unlike true relativistic Fermionic systems [7], the Dirac quasiparticles in Graphene still propagate with a velocity that is much smaller than the speed of light, the speed that Coulomb interactions propagate. Therefore, the Coulomb field can be considered instantaneous in first approximation, rendering the electrodynamics of Graphene electrons a join between a relativistic and a non-relativistic problem. Without any doubt, this unusual situation requires a re-evaluation of the Fermi liquid theory for this material.

1.2 Chemistry

The electronic arrangement of atomic carbon is $1s^2\,2s^2\,2p^2$. In a solid, however, carbon setup $s-p$ hybridized orbitals.

In $s-p$ hybridization, a linear combination of the $2s$ orbital and one of the $2p$ orbitals of a carbon atom, for example $2p_x$,is formed [34]. From these two atomic orbitals of a carbon atom, two hybridized sp atomic orbitals, denoted by $|sp_1\rangle$, and $|sp_2\rangle$,expressed by the linear combination of $|2s\rangle$ and $|2p_x\rangle$ wave functions of the carbon atom.

Figure 1.1 shows a schematic view of the directed valence of the $|2s\rangle+|2p_x\rangle = \sqrt{2}|sp\rangle$, orbital. The shading denotes a negative amplitude of the wave function. Here, the radial wave function of the $2s$ orbitals has a node around $r = 0.2$Å(0.02 nm) because of the orthogonality with $1s$ orbitals, while that of the $2p$ orbitals has no nodes except for $r = 0$ in the radial direction [34].

Figure 1.1 defines a positive amplitude of the $2s$ wave function for a given radius for $r > 0.2$ Å for simplicity.The sign of the wave-functionis not essential to physical properties as long as the definition of the sign is consistent within the discussion. In this definition,the wave function of $|2s\rangle + |2p_x\rangle$ is elongated in the positive direction of x (Fig. 1.1), while that of $|2s\rangle - |2p_x\rangle$ is elongated in the negative direction of x.

Thus, when nearest-neighbor atoms are in the direction of the x axis, the overlap of $|sp_1\rangle$ with the wave function at $x > 0$ becomes larger compared with the original $|2p_x\rangle$ function, so giving rise to a larger binding energy. If $|2p_y\rangle$ for $|2p_x\rangle$ selected, the wave function shows a valence in the direction of the y axis.

The $1s$ electrons setup a deep valence band and necessarily all properties of carbon-based materials can be characterized in terms of the 2s and $2p_x$, $2p_y$ and $2p_z$ orbitals that

can be written as [8; 12]:

Figure 1.1: *sp* hybridization. The shading denotes the negative amplitude of the wave function. $|2s\rangle + |2p_x\rangle$ is elongated in the positive direction of x. From [34]

$$\langle \vec{r}|s\rangle = R_s(r) \times 1,$$

$$\langle \vec{r}|p_x\rangle = R_p(r) \times \sqrt{3}\ \sin\theta\ \cos\phi,$$

$$\langle \vec{r}|p_y\rangle = R_p(r) \times \sqrt{3}\ \sin\theta\ \sin\phi,$$

$$\langle \vec{r}|p_z\rangle = R_p(r) \times \sqrt{3}\ \cos\theta, \tag{1.1}$$

Where $R_s(r) = (2 - r/a_0)e^{-r/(2a_0)}$, and $R_p(r) = (r/a_0)e^{-r/(2a_0)}$ are the radial wave-functions, in which $a_0 = 0.529167$Å is termed the first *Bohr radius* of Hydrogen. One special way to parametrize a hybridized $s - p$ state is introduced by Pauling [9]:

$$|0\rangle = A|s\rangle + \sqrt{1 - A^2}\,|p_z\rangle \tag{1.2}$$

Where A is a parameter that explains the degree of hybridization between s and p states. This basic orbital is shown in Fig. 1.1. The energy associated with this orbital can be acquired from the hydrogen atom spectrum [12]:

$$E_0 = \epsilon_\pi = \langle 0|H_0|0\rangle = A^2 E_s + (1 - A^2)E_p \tag{1.3}$$

where H_0 is the hydrogen atom Hamiltonian, $E_s \approx -19.38eV$ is the energy of the $2s$-state and $E_p \approx -11.07eV$ is the energy of the $2p$-state. All the other 3 orthogonal orbitals can be set up starting from (1.2). A special simple parametrization is the following [10]:

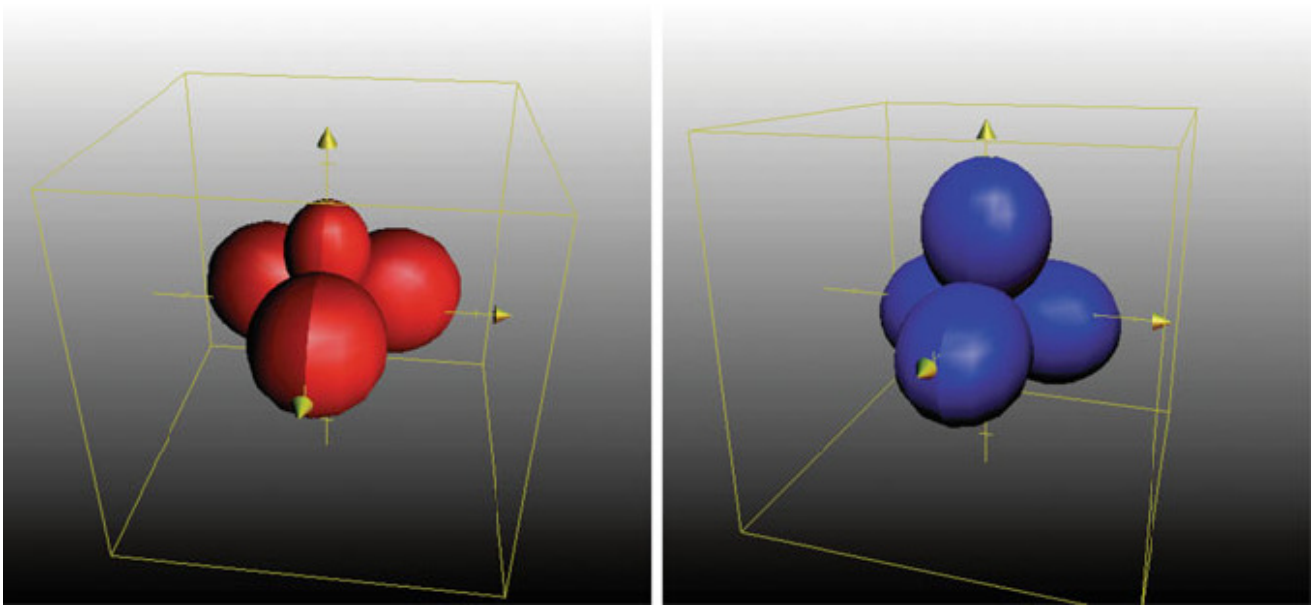

Figure 1.2: sp^2 (left) and sp^3 (right) hybridized orbitals

$$\begin{aligned}
|1\rangle &= \sqrt{(1-A^2)/3}\,|s\rangle + \sqrt{2/3}\,|p_x\rangle - (A/\sqrt{3})\,|p_z\rangle, \\
|2\rangle &= \sqrt{(1-A^2)/3}\,|s\rangle - \sqrt{1/6}\,|p_x\rangle - \sqrt{1/2}\,|p_y\rangle - (A/\sqrt{3})\,|p_z\rangle, \\
|3\rangle &= \sqrt{(1-A^2)/3}\,|s\rangle - \sqrt{1/6}\,|p_x\rangle + \sqrt{1/2}\,|p_y\rangle - (A/\sqrt{3})\,|p_z\rangle,
\end{aligned} \tag{1.4}$$

Notice that A controls the angle between the z axis and these states. It can be seen that the direction of largest amplitude for one of these orbitals (say, $\langle\vec{r}|1\rangle$) is given by [12]:

$$\frac{\partial}{\partial\theta}\langle\vec{r}|1\rangle(\phi = 0) = \sqrt{2}\cos\theta_m + A\ \sin\theta_m = 0,$$

$$\theta_m = -\arctan(\sqrt{2}/A) \tag{1.5}$$

Therfore, for $A = 0$ the hybridized state $|1\rangle$ is perpendicular to the other orbitals that keep on in the $x - y$ plane. This is the so-called sp^2 hybridization (see Fig. 1.2). For $A = 1/2$ the orbitals have tetragonal structure building an angle of 109.47° with the z axis. This is the sp^3 hybridization (see Fig. 1.2). In free space, the states $|1\rangle$, $|2\rangle$ and $|3\rangle$ are certainly degenerate and their energy is given by [12]:

$$E_1 = E_2 = E_3 = \langle 1|H_0|1\rangle = \epsilon_\sigma = \frac{1 - A^2}{3}E_s + \frac{2 + A^2}{3}E_p\,. \tag{1.6}$$

The energy of these states is shown in Fig. 1.3. In the sp^3 case ($A = 1/2$) all orbitals are degenerated while in the sp^2 case the orbitals are separated by an energy of approximately 2.77eV.

The attendance of another carbon atom induces a hybridization between the different orbitals. This hybridization depends on the distance between the atoms and also on the orientation of the orbitals relative to each other.

The distance l dependence is usually well described by an exponential behavior [12]:

$$V_\alpha(l) \approx {V_\alpha}^0\, e^{-k_\alpha l} \tag{1.7}$$

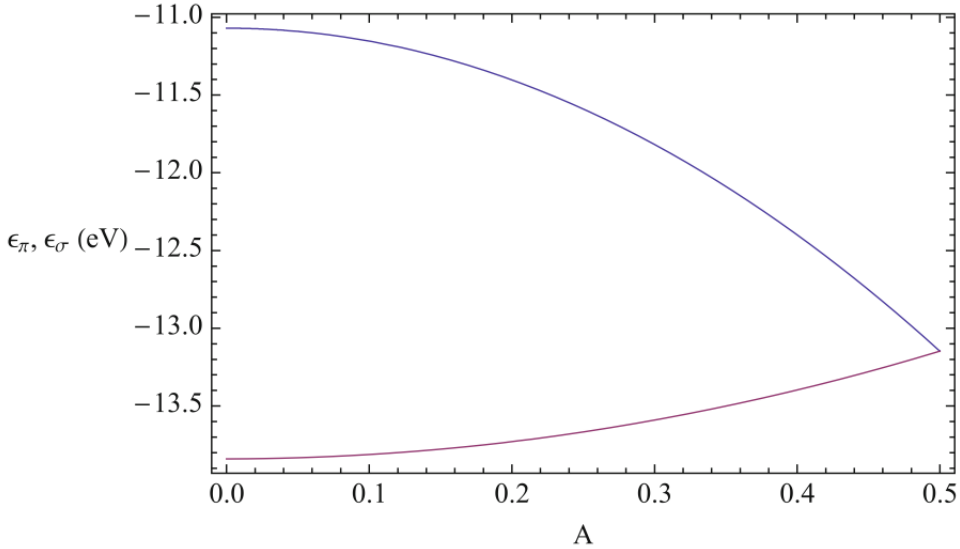

Figure 1.3: Energy of the hybridized $s-p$ states, in blue (top curve) we show the energy of the π state, (1.3), and in red (bottom curve) the energy of the σ state, (1.6), as a function of the hybridization parameter A. $A = 0$ corresponds to the sp^2 and $A = 1/2$ corresponds to the sp^3 configuration. From [12]

where $k_\alpha = d\ln(V_\alpha)/dl$ and α labels the different orientations of the orbitals.

One can also compute inter-atomic hybridization energies such as the hybridization between two $|2\rangle$ states oriented as in Fig. 1.5:

$$V_\sigma = -\frac{2}{3}V_{pp\sigma} + \frac{1-A^2}{3}V_{ss\sigma} - \frac{2}{3}\sqrt{2(1-A^2)}V_{sp\sigma}\ . \tag{1.8}$$

In terms of orientation, there are four different types of elementary hybridization between different orbitals (shown in Fig. 1.4): $V_{ss\sigma}(\approx -5eV$ for $l = 1.42$ Å); $V_{sp\sigma}(\approx +5.4eV$for $l = 1.42$Å); $V_{pp\sigma}(\approx +8.4eV$ for $l = 1.42$Å); $V_{pp\pi}(\approx -2.4eV$ for graphene $l = 1.42$Å) [11].

Any hybridization energy can be gained from those basic hybridizations shown in Fig.

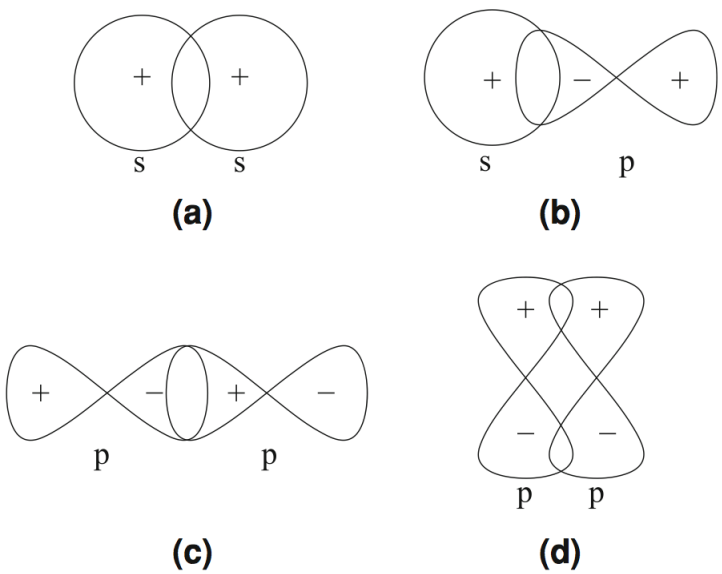

Figure 1.4: Basic hypridization energies for $s - p$ bonds: (**a**) $V_{ss\sigma}$, (**b**) $V_{sp\sigma}$, (**c**) $V_{pp\sigma}$, (**d**)$V_{pp\pi}$. From [12]

1.4 as linear combinations. We consider the intra-atomic hybridization between $|2\rangle$ and $|3\rangle$. This is given by the matrix element [12]:

$$V_{intra} = \langle 2|H_0|3\rangle = \langle 2|\left(\sqrt{\frac{1-A^2}{3}}E_s|s\rangle - \frac{E_p}{\sqrt{6}}|p_x\rangle + \frac{E_p}{\sqrt{2}}|p_y\rangle - \frac{A}{\sqrt{3}}E_p|p_z\rangle\right)$$

$$= \frac{1-A^2}{3}(E_s - E_p). \tag{1.9}$$

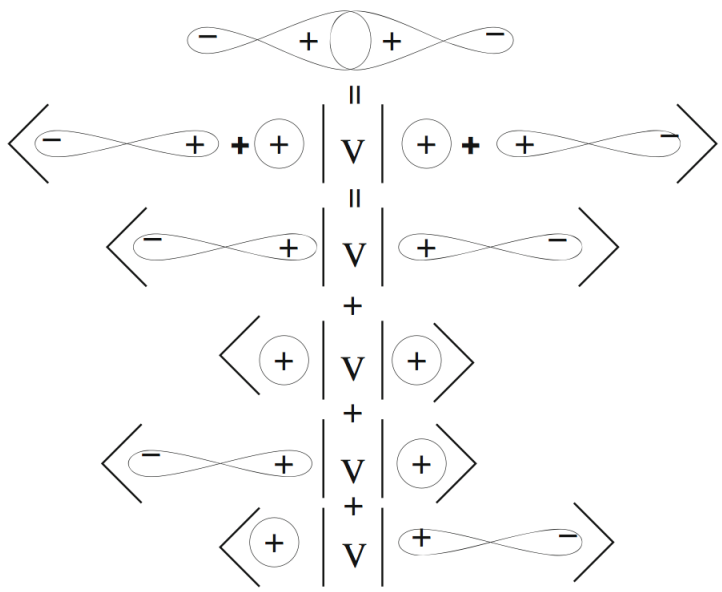

Figure 1.5: Calculation of the hybridization of two $s - p$ orbitals in terms of the basic hybridization energies shown in Fig 1.4 .Adopted from [12]

1.3 The Crystal and Band Structure

1.3.1 Graphene's honeycomb lattice

The carbon atoms in graphene compact in a honeycomb lattice with sp^2 hybridisation. The honeycomb lattice is not a Bravais lattice since two neighbouring sites are not equivalent. Fig. 1.6 (a) demonstrates actually that a site on the A sublattice has nearest neighbours (nn) in the directions south, north-west, and north-east, although a site on the B sublattice has nns in the directions north, south-west, and south-east. Both A and B sublattices, however, are triangular Bravais lattices, and one may look at the honeycomb lattice as a triangular Bravais lattice with a two-atom basis (A and B). The distance be-

tween nn carbon atoms is 0.142 nm, which is the average of the single $(C-C)$ and double $(C=C)$ covalent σ bonds, as in the case of benzene.

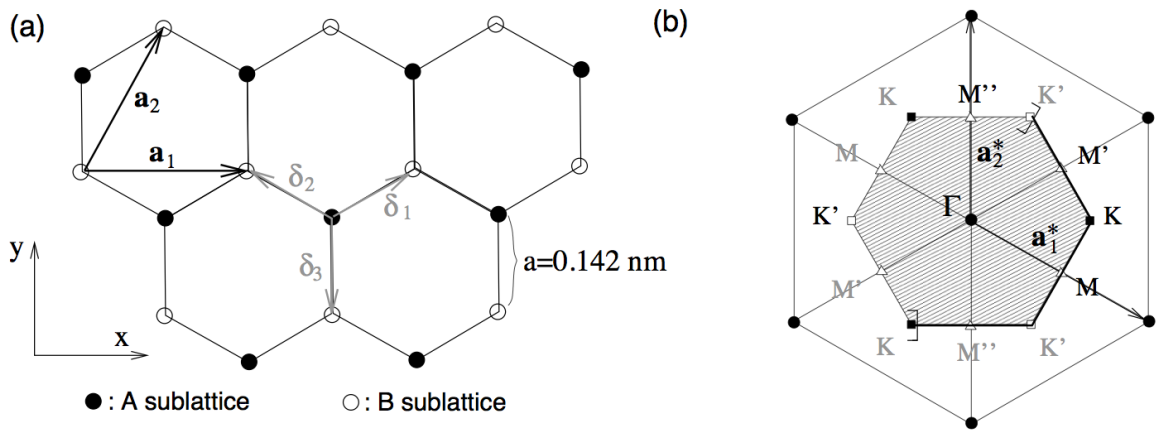

Figure 1.6: (a) Honeycomb lattice. The vectors $\boldsymbol{\delta}_1, \boldsymbol{\delta}_2$ and $\boldsymbol{\delta}_3$ connect nn carbon atoms, separated by a distance $a = 0.142nm$. The vectors $\mathbf{a}_1$ and $\mathbf{a}_2$ are basis vectors of the triangular Bravais lattice. (b) Reciprocal lattice of the triangular lattice. Its primitive lattice vectors are $\mathbf{b}_1 = \mathbf{a}_1^*$ and $\mathbf{b}_2 = \mathbf{a}_2^*$. The shaded region represents the first Brillouin zone (BZ), with its centre Γ and the two inequivalent corners K (black squares) and K' (white squares). The thick part of the border of the first BZ represents those points which are counted in the definition such that no points are doubly counted. The first BZ, defined in a strict manner, is, thus, the shaded region plus the thick part of the border. For completeness, it is shown the three inequivalent cristallographic points M, M', and M'' (white triangles).

The three vectors which link a site on the A sublattice with a nn on the B sublattice are given by

$$\boldsymbol{\delta}_1 = \frac{a}{2}\Big(\sqrt{3}\mathbf{e}_x + \mathbf{e}_y\Big), \qquad \boldsymbol{\delta}_2 = \frac{a}{2}\Big(-\sqrt{3}\mathbf{e}_x + \mathbf{e}_y\Big), \qquad \boldsymbol{\delta}_3 = -a\mathbf{e}_y \ , \tag{1.10}$$

and the triangular Bravais lattice is spanned by the basis vectors

$$\mathbf{a}_1 = \sqrt{3}\, a\, \mathbf{e}_x \qquad \mathbf{a}_2 = \frac{\sqrt{3}a}{2}\left(\mathbf{e}_x + \sqrt{3}\mathbf{e}_y\right) \ . \tag{1.11}$$

The modulus of the basis vectors yields the lattice spacing, parameter $\widetilde{a} = \sqrt{3}a = 0.24nm$, and the area of the unit cell is $A_{uc} = \sqrt{3}\widetilde{a}^2/2 = 0.051nm^2$. The density of carbon atoms is, then, $n_C = 2/A_{uc} = 39nm^{-2} = 3.9 \times 10^{15}cm^{-2}$. Since there is one π electron per carbon atom that is not involved in a covalent σ bond, there are as many valence electrons as carbon atoms, and their density is, therefore, $n_\pi = n_C = 3.9 \times 10^{15}cm^{-2}$. The carrier density in graphene, which one measures in electrical transport measurements, is the different between the true n_π and this value for neutral Graphene.

The reciprocal lattice, which is defined with respect to the triangular Bravais lattice, is shown in Fig. 1.6 (b). It is spanned by the vectors

$$\mathbf{b}_1 = \frac{2\pi}{\sqrt{3}a}\left(\mathbf{e}_x - \frac{\mathbf{e}_y}{\sqrt{3}}\right) \quad \text{and} \quad \mathbf{b}_2 = \frac{4\pi}{3a}\mathbf{e}_y \tag{1.12}$$

Physically, all sites of the reciprocal lattice exemplify equivalent wave vectors. Any wave be it a vibrational lattice excitation or a quantum-mechanical electronic wave packet propagating on the lattice with a wave vector differing by a reciprocal lattice vector has in fact the same phase up to a multiple of 2π, due to the relation (for $i, j = 1, 2$) between direct and reciprocal lattice vectors.

$$\mathbf{a}_i \cdot \mathbf{b}_j = 2\pi\delta_{ij} \tag{1.13}$$

The first Brillouin zone [BZ, shaded region and thick part of the border of the hexagon in Fig. 1.6 (b)] shows a set of inequivalent points in the reciprocal space, i.e. of points

which may not be connected to one another by a reciprocal lattice vector, or else of physically distinguishable lattice excitations. The long wavelength excitations are situated in the vicinity of the Γ point, in centre of the first BZ. As well, one distinguishes the six corners of the first BZ, which consist of the inequivalent points K(+**K**) and K'(-**K**) represented by the vectors

$$\pm\mathbf{K} = \pm\frac{4\pi}{3\sqrt{3}a}\mathbf{e}_x\,. \tag{1.14}$$

The four remaining corners [shown in gray in Fig. 1.6 (b)] may indeed be connected to one of these points via a translation by a reciprocal lattice vector. These cristallographic points play an important role in the electronic properties of graphene because their low-energy excitations are centered around the two points K and K', as is discussed in detail in the following section. The inequivalence of the two BZ corners, K and K', has nothing to do with the presence of two sublattices, A and B, in the honeycomb lattice. The form of the BZ is a basic property of the Bravais lattice, independent of the possible presence of more than one atom in the unit cell. For completeness, It has also shown, in Fig. 1.6 (b), the three crystallographically inequivalent M points in the middle of the BZ edges.

1.4 Electronic properties and Band Structure of Graphene

Three electrons per carbon atom in graphene creat strong covalent σ bonds, and one electron per atom gives the π bonds, on the other word it can be said: the three sp^2-hybridized orbitals are oriented in the xy plane and have mutual 120 angles. The remaining unhybridized $2p_z$ orbital is perpendicular to the plane [35]. The π electrons are responsible for physics at low energies, whereas the σ electrons arrange energy bands far away from the Fermi energy. In this part we discuss the energy bands of π electrons within the tight-binding approximation, which was for the first time calculated for the hexagonal lattice by P. R. Wallace [13]. It does not consider the σ electrons, here. The section consists of two parts. The first one is devoted to the calculation of the π energy bands in graphene, which it is considered the problem of two atoms per unit cell. After a brief discussion of Blochs theorem, and a formal solution of the tight-binding model, one calculates the energy dispersion of π electrons in graphene, taking into account nearest-neighbour (nn) and next-nearest-neighbour (nnn) hopping and nn overlap corrections. The second section we discuss the low-energy properties of electrons in graphene.

1.4.1 Tight-Binding Model for Electrons on Honeycomb Lattice

By introducing a general explanation of the tight-binding model for a system with n atomic orbitals j in the unit cell, labeled by index $j = 1...n$. Further details may be found in the book by [14]. It is supposed that the system has translational invariance. Then the model may be written using n different Bloch functions $\phi_j(\mathbf{k}, \mathbf{r})$ that depend on the position vector $\mathbf{r}$ and wave vector $\mathbf{k}$. They are given by [27] (I should notice that the most of well-known calculations in this part are taken from [27])

$$\phi_j(\mathbf{k},\mathbf{r}) = \frac{1}{\sqrt{N}} \sum_{i=1}^{N} e^{i\mathbf{k}\cdot\mathbf{R}_{j,i}}\, \phi_j\left(\mathbf{r} - \mathbf{R}_{j,i}\right) \tag{1.15}$$

where the sum is over N different unit cells, labeled by index $i = 1...N$, and $\mathbf{R}_{j,i}$ denotes the position of the j th orbital in the ith unit cell. In general, an electronic wave function $\psi_j\left(\mathbf{k},\mathbf{r}\right)$ is given by a linear superposition of the n different Bloch functions,

$$\psi_j(\mathbf{k},\mathbf{r}) = \sum_{l=1}^{n} c_{j,l}(\mathbf{k})\, \phi_l(\mathbf{k},\mathbf{r}) \tag{1.16}$$

where $c_{j,l}(\mathbf{k})$ are coefficients of the expansion. The energy $E_j(\mathbf{k})$ of the j th band is given by

$$E_j(\mathbf{k}) = \frac{\langle\psi_j|\mathcal{H}|\psi_j\rangle}{\langle\psi_j|\psi_j\rangle} \tag{1.17}$$

where $\mathcal{H}$ is the Hamiltonian. Substituting the expansion of the wave function (1.16) into the energy gives

$$E_j(\mathbf{k}) = \frac{\sum_{i,l}^{n}\ c_{ji}^{*}\ c_{jl}\ \langle\phi_i|\mathcal{H}|\phi_l\rangle}{\sum_{i,l}^{n}\ \ c_{jl}^{*}\ c_{jl}\ \langle\phi_i|\phi_l\rangle} \tag{1.18}$$

$$= \frac{\sum_{i,l}^{n} H_{il}\ c_{ji}^{*}\ c_{jl}}{\sum_{i,l}^{n}\ S_{il}\ c_{ji}^{*}\ c_{jl}} \tag{1.19}$$

where transfer integral matrix elements H_{il} and overlap integral matrix elements S_{il} are given by

$$H_{il} = \langle\phi_i|\mathcal{H}|\phi_l\rangle, \qquad S_{il} = \langle\phi_i|\phi_l\rangle \tag{1.20}$$

One minimizes the energy E_j with respect to the coefficient c^*_{jm} by calculating the derivative

$$\frac{\partial E_j}{\partial c^*_{jm}} = \frac{\sum_l^n H_{ml}\, c_{jl}}{\sum_{i,l}^n \; S_{il} \; c^*_{ji} \; c_{jl}} - \frac{\sum_{i,l}^n H_{il}\, c^*_{ji}\, c_{jl} \;\; \sum_l^n S_{ml}\, c_{jl}}{\left(\sum_{i,l}^n \; S_{il} \; c^*_{ji} \; c_{jl} \; \right)^2}. \tag{1.21}$$

The second term holds a factor equal to the energy E_j itself, (1.19). Then setting $\frac{\partial E_j}{\partial c^*_{jm}} = 0$ and omitting the common factor $\sum_{i,l}^n \; S_{il} \; c^*_{ji} \; c_{jl}$ gives

$$\sum_{l=1}^{n} H_{ml}\, c_{jl} = E_j \sum_{l=1}^{n} S_{ml}\, c_{jl}\,. \tag{1.22}$$

This can be written as a matrix equation. Consider the specific model of two orbitals per unit cell, $n = 2$. Then one can choose the possible values of m (either $m = 1$ or $m = 2$) and write out the summation in (1.22) explicitly:

$$m = 1 \quad \Rightarrow \quad H_{11} c_{j1} + H_{12} c_{j2} = E_j\,(S_{11} c_{j1} + S_{12} c_{j2}) \;\;, \tag{1.23}$$

$$m = 2 \quad \Rightarrow \quad H_{21} c_{j1} + H_{22} c_{j2} = E_j\,(S_{21} c_{j1} + S_{22} c_{j2}) \;\;. \tag{1.24}$$

These two equations can be joined into a matrix equation

$$\begin{pmatrix} H_{11} & H_{12} \\ H_{21} & H_{22} \end{pmatrix} \begin{pmatrix} c_{j1} \\ c_{j2} \end{pmatrix} = E_j \begin{pmatrix} S_{11} & S_{12} \\ S_{21} & S_{22} \end{pmatrix} \begin{pmatrix} c_{j1} \\ c_{j2} \end{pmatrix} \;\;. \tag{1.25}$$

For general values of n, introducing H as the transfer integral matrix, integral matrix, S as the overlap and ψ_j as a column vector,

$$H = \begin{pmatrix} H_{11} & H_{12} & \cdots & H_{1n} \\ H_{21} & H_{22} & \cdots & H_{2n} \\ \vdots & \vdots & \ddots & \vdots \\ H_{n1} & H_{n2} & \cdots & H_{nn} \end{pmatrix}, \quad S = \begin{pmatrix} S_{11} & S_{12} & \cdots & S_{1n} \\ S_{21} & S_{22} & \cdots & S_{2n} \\ \vdots & \vdots & \ddots & \vdots \\ S_{n1} & S_{n2} & \cdots & S_{nn} \end{pmatrix}, \quad \psi_j = \begin{pmatrix} c_{j1} \\ c_{j2} \\ \vdots \\ c_{jn} \end{pmatrix}. \tag{1.26}$$

lets the relation (1.22) to be signified as

$$H\,\psi_j = E_j\,S\,\psi_j\ . \tag{1.27}$$

The energies E_j can be driven by solving the secular equation

$$\det\left(H - E_j\,S\right) = 0\ , \tag{1.28}$$

Already the transfer integral matrix H and the overlap integral matrix S are known. Here, ”det” mounts for the determinant of the matrix. In the following, one will delete the subscript $j = 1 \cdots n$ in (1.27), (1.28), notice that ”the number of solutions is equal to the number of different atomic orbitals per unit cell” [27].

1.5 Tight-Binding Model of Monolayer Graphene

One applies the tight-binding model mentioned in previous section to monolayer graphene, taking into consideration one $2p_z$ orbital per atomic site. Since there are two atoms in the unit cell of graphene, labeled A and B in Fig. 1.6, the model has two Bloch functions, $n = 2$. To be easier, one replaces index $j = 1$ with $j = A$, and $j = 2$ with $j = B$. By

continuing to determine the transfer integral matrix H and the overlap integral matrix S.

1.5.1 Diagonal Matrix Elements

Substituting the expression for the Bloch function (1.15) into the expression of the transfer integral (1.20) allows us to compute the diagonal matrix element corresponding to the A sublattice as

$$H_{AA} = \frac{1}{N}\sum_{i=1}^{N}\sum_{j=1}^{N} e^{i\mathbf{k}\cdot(\mathbf{R}_{A,j}-\mathbf{A}_{A,i})}\langle\phi_A(\mathbf{r}-\mathbf{R}_{A,i})|\mathcal{H}|\phi_A(\mathbf{r}-\mathbf{R}_{A,j})\rangle \ , \tag{1.29}$$

where $\mathbf{k} = (k_x, k_y)$ is the wave vector in the graphene plane. Equation (1.29) contains a double summation over all the A sites of the lattice. If one supposes that the dominant contribution arises from the same site $j = i$ within each unit cell, then:

$$H_{AA} \approx \frac{1}{N}\sum_{i=1}^{N}\langle\phi_A(\mathbf{r}-\mathbf{R}_{A,i})|\mathcal{H}|\phi_A(\mathbf{r}-\mathbf{R}_{A,j})\rangle \ , \tag{1.30}$$

The matrix element $\langle\phi_A|\mathcal{H}|\phi_A\rangle$ in the summation has the same value on every A site, i.e. it is independent of the site index i. One firms it to be equal to a parameter

$$\epsilon_{2p} = \langle\phi_A(\mathbf{r}-\mathbf{R}_{A,i})|\mathcal{H}|\phi_A(\mathbf{r}-\mathbf{R}_{A,j})\rangle \ , \tag{1.31}$$

that is equal to the energy of the $2p_z$ orbital. Therefore keeping just the same site contribution,

$$H_{AA} \approx \frac{1}{N}\sum_{i=1}^{N}\epsilon_{2p} = \epsilon_{2p} \ , \tag{1.32}$$

It is possible to take into consideration the contribution of other terms in the double summation (1.15), such as next-nearest neighbor contributions [15; 16]. They generally have a small effect on the electronic band structure and will not be discussed here. The B sublattice has the same structure as the A sublattice, and the carbon atoms on the two sublattices are chemically identical. This means that the diagonal transfer integral matrix element corresponding to the B sublattice has the same value as that of the A sublattice:

$$H_{BB} = H_{AA} = \epsilon_{2p} \ , \tag{1.33}$$

A calculation of the diagonal elements of the overlap integral matrix continues in a similar way as for those of the transfer integral. In this case, the overlap between a $2p_z$ orbital on the same atom is equal to unity,

$$\langle \phi_A(\mathbf{r} - \mathbf{R}_{A,i}) | \phi_A(\mathbf{r} - \mathbf{R}_{A,j}) \rangle = 1 \ , \tag{1.34}$$

Then supposing that the same site contribution governs,

$$S_{AA} = \frac{1}{N} \sum_{i=1}^{N} \sum_{j=1}^{N} e^{i\mathbf{k}\cdot(\mathbf{R}_{A,j} - \mathbf{A}_{A,i})} \langle \phi_A(\mathbf{r} - \mathbf{R}_{A,i}) | \phi_A(\mathbf{r} - \mathbf{R}_{A,j}) \rangle \ , \tag{1.35}$$

$$\approx \frac{1}{N} \sum_{i=1}^{N} \langle \phi_A(\mathbf{r} - \mathbf{R}_{A,i}) | \phi_A(\mathbf{r} - \mathbf{R}_{A,j}) \rangle \ , \tag{1.36}$$

$$= \frac{1}{N} \sum_{i=1}^{N} 1 \ , \tag{1.37}$$

$$= 1 \ . \tag{1.38}$$

Again, as the B sublattice has the alike structure as the A sublattice,

$$S_{BB} = S_{AA} = 1 \ , \tag{1.39}$$

1.5.2 Off-Diagonal Matrix Elements

Substituting the relation for the Bloch function (1.15) into the definition of the transfer integral (1.20) lets us to write out an off-diagonal matrix element as

$$H_{AB} = \frac{1}{N} \sum_{i=1}^{N} \sum_{j=1}^{N} e^{i\mathbf{k}\cdot(\mathbf{R}_{B,j}-\mathbf{R}_{A,i})} \langle \phi_A(\mathbf{r}-\mathbf{R}_{A,i}) | \mathcal{H} | \phi_B(\mathbf{r}-\mathbf{R}_{B,j}) \rangle \ , \tag{1.40}$$

It expresses processes of hopping between the A and B sublattices, and includes a summation over all the A sites ($i = 1 \cdots N$) at positions $\mathbf{R}_{A,i}$ and all the B sites ($j = 1 \cdots N$) at $\mathbf{R}_{B,i}$.

In the following, one can suppose that the dominant contribution to the off-diagonal matrix element (1.40) comes out from hopping between nearest neighbors only. If one focuses on an individual A atom, i.e. we take into account a fixed value of the index i, it has three neighboring B atoms, Fig. 1.7, that we will label with a new index l ($l = 1 \cdots 3$). Each A atom has three such neighbors, so it is feasible to write the nearest-neighbors contribution to the off-diagonal matrix element (1.40) as

$$H_{AB} \approx \frac{1}{N} \sum_{i=1}^{N} \sum_{l=1}^{3} e^{i\mathbf{k}\cdot(\mathbf{R}_{B,j}-\mathbf{R}_{A,i})} \langle \phi_A(\mathbf{r}-\mathbf{R}_{A,i}) | \mathcal{H} | \phi_B(\mathbf{r}-\mathbf{R}_{B,l}) \rangle \ , \tag{1.41}$$

The matrix element between neighboring atoms, $\langle\phi_A|\mathcal{H}|\phi_B\rangle$, has the same value for each neighboring pair, i.e., it is independent of indices i and l . By setting of it equal to a parameter, $t = \langle\phi_A(\mathbf{r}-\mathbf{R}_{A,i})|\mathcal{H}|\phi_B(\mathbf{r}-\mathbf{R}_{B,l})\rangle$. Since t is negative [14], it is usual practice to express it in terms of a positive parameter $\gamma_0 = -t$, where

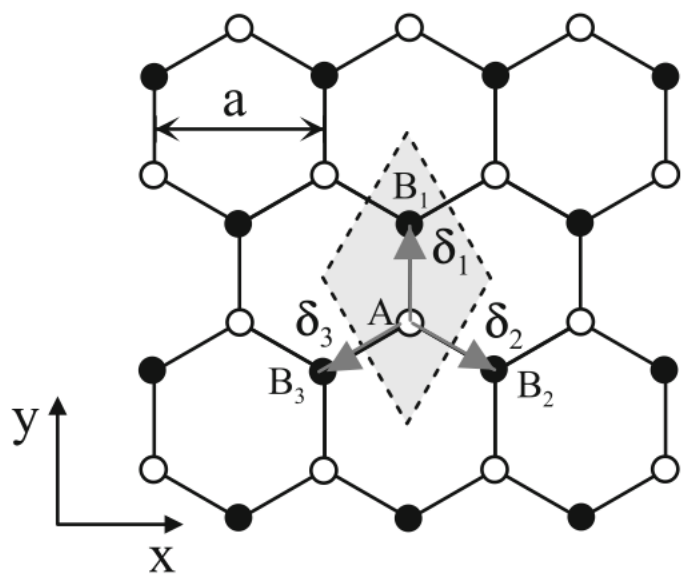

Figure 1.7: The honeycomb crystal structure of monolayer graphene. In the nearest-neighbor approximation, one can consider hopping from an A site (white) to three adjacent B sites (black), labeled B_1, B_2, B_3, with position vectors $\boldsymbol{\delta}_1, \boldsymbol{\delta}_2, \boldsymbol{\delta}_3$ respectively, relative to the A site

$$\gamma_0 = -\langle\phi_A(\mathbf{r}-\mathbf{R}_{A,i})|\mathcal{H}|\phi_B(\mathbf{r}-\mathbf{R}_{B,l})\rangle \ . \tag{1.42}$$

Therefore one can write the off-diagonal transfer integral matrix element as

$$H_{AB} \approx -\frac{1}{N}\sum_{i=1}^{N}\sum_{l=1}^{3} e^{i\mathbf{k}\cdot(\mathbf{R}_{B,l}-\mathbf{R}_{A,i})}\gamma_0 \ , \tag{1.43}$$

$$= -\frac{\gamma_0}{N}\sum_{i=1}^{N}\sum_{l=1}^{3} e^{i\mathbf{k}\cdot\boldsymbol{\delta}_l} \equiv -\gamma_0\, f(\mathbf{k}) \ , \tag{1.44}$$

$$f(\mathbf{k}) = \sum_{l=1}^{3} e^{i\mathbf{k}\cdot\boldsymbol{\delta}_l} \ , \tag{1.45}$$

here the position vector of atom B_l relative to the A_i atom is denoted $\boldsymbol{\delta}_l = \mathbf{R}_{B,l} - \mathbf{R}_{A,i}$, and by using of the fact that the summation over the three neighboring B atoms is the same for all A_i atoms. For the three B atoms shown in Fig. 1.7, the three vectors are

$$\boldsymbol{\delta}_1 = \left(0, \frac{a}{\sqrt{3}}\right), \quad \boldsymbol{\delta}_2 = \left(\frac{a}{2}, -\frac{a}{2\sqrt{3}}\right), \quad \boldsymbol{\delta}_3 = \left(-\frac{a}{2}, -\frac{a}{2\sqrt{3}}\right), \tag{1.46}$$

It shotld be mentioned that $|\boldsymbol{\delta}_1| = |\boldsymbol{\delta}_2| = |\boldsymbol{\delta}_3| = \frac{a}{\sqrt{3}}$ is the carbon-carbon bond length. Then the function $f(\mathbf{k})$ explaining nearest-neighbor hopping may be calculated as

$$f(\mathbf{k}) = \sum_{l=1}^{3} e^{i\mathbf{k}\cdot\boldsymbol{\delta}_l} \ , \tag{1.47}$$

$$= e^{ik_y \frac{a}{\sqrt{3}}} + e^{ik_x \frac{a}{2}} e^{-ik_y \frac{a}{2\sqrt{3}}} + e^{-ik_x \frac{a}{2}} e^{-ik_y \frac{a}{2\sqrt{3}}} \ , \tag{1.48}$$

$$= e^{ik_y \frac{a}{\sqrt{3}}} + 2e^{-ik_y \frac{a}{2\sqrt{3}}} \cos(k_x\, a/2) \ . \tag{1.49}$$

The other off-diagonal matrix element H_{BA} is the complex conjugate of H_{AB}:

$$H_{AB} \approx -\gamma_0 f(\mathbf{k}) \ , \qquad H_{BA} \approx -\gamma_0 f^*(\mathbf{k}) \ . \tag{1.50}$$

A derivation of an off-diagonal element of the overlap integral matrix continues in a similar way as for the transfer integral:

$$S_{AB} = \frac{1}{N} \sum_{i=1}^{N} \sum_{j=1}^{N} e^{i\mathbf{k}\cdot(\mathbf{R}_{B,j}-\mathbf{R}_{A,i})} \langle \phi_A(\mathbf{r}-\mathbf{R}_{A,i}) | \phi_B(\mathbf{r}-\mathbf{R}_{B,j}) \rangle \ , \tag{1.51}$$

$$\approx \frac{1}{N} \sum_{i=1}^{N} \sum_{l=1}^{3} e^{i\mathbf{k}\cdot(\mathbf{R}_{B,l}-\mathbf{R}_{A,i})} \langle \phi_A(\mathbf{r}-\mathbf{R}_{A,i}) | \phi_B(\mathbf{r}-\mathbf{R}_{B,l}) \rangle \ , \tag{1.52}$$

$$= s_0 \, f(\mathbf{k}) \ , \tag{1.53}$$

in which the parameter $s_0 = \langle \phi_A(\mathbf{r}-\mathbf{R}_{A,i}) | \phi_B(\mathbf{r}-\mathbf{R}_{B,l}) \rangle$ and $S_{BA} = S^*_{AB} = s_0 \, f^*(\mathbf{k})$. The presence of nonzero s_0 takes into consideration the possibility that orbitals on adjacent atomic sites are not strictly orthogonal.

1.5.3 The Low-Energy Electronic Bands of Monolayer Graphene

Summarizing the results of this part, the transfer integral matrix elements (1.33) and (1.50), and the overlap integral matrix elements (1.39) and (1.53) give

$$H_1 = \begin{pmatrix} \epsilon_{2p} & -\gamma_0 \, f(\mathbf{k}) \\ \gamma_0 \, f(\mathbf{k}) & \epsilon_{2p} \end{pmatrix} , \qquad S_1 = \begin{pmatrix} 1 & s_0 \, f(\mathbf{k}) \\ s_0 \, f^*(\mathbf{k}) & 1 \end{pmatrix} . \tag{1.54}$$

where it is used the subscript "1" to emphasis that these matrices apply to monolayer Graphene. The corresponding energy E can be determined by solving the secular equation $\det(H1 - ES_1) = 0$, (1.28):

$$\det\begin{pmatrix} \epsilon_{2p} - E & -(\gamma_0 + E\, s_0)\, f(\mathbf{k}) \\ -(\gamma_0 + E\, s_0)\, f^*(\mathbf{k}) & \epsilon_{2p} - E \end{pmatrix} = 0 \ , \tag{1.55}$$

$$\Rightarrow \ (E - \epsilon_{2p})^2 \ - \Big([E - \epsilon_{2p}]s_0 + \epsilon_{2p}\, s_0 + \gamma_0\Big)^2 \ |f(\mathbf{k})| = 0 \ , \tag{1.56}$$

Solving this quadratic equation hands over the energy:

$$E_{\pm} = \frac{\epsilon_{2p} \pm \gamma_0\, |f(\mathbf{k})|}{1 \mp s_0\, |f(\mathbf{k})|} \ , \tag{1.57}$$

This expression appears in Saito et al [14], where parameter values $\gamma_0 = 3.033$ eV, $s_0 = 0.129$, $\epsilon_{2p} = 0$ are quoted. The latter value ($\epsilon_{2p} = 0$) denotes that the zero of energy is set to be equal to the energy of the $2p_z$ orbital. The resulting band structure $E_{\pm}$ is illustrated in Fig. 1.8 in the vicinity of the Brillouin zone. A special cut through the band structure is illustrated in Fig. 1.9, where the bands are plotted as a function of wave vector component k_x along the line $k_y = 0$, a line that passes through the center of the Brillouin zone, labeled , and two corners of the Brillouin zone, labeled K_+ and K_- (see the inset of Fig. 1.9). The Fermi level in pure graphene is located at zero energy. There are two energy bands that it is mentioned to as the conduction band (E_+) and the valence band (E_-). The interesting characteristic of the band structure is that there is no band gap between the conduction and valence bands. Instead the bands cross at the six corners of the Brillouin zone [27], Fig. 1.7. Brillouin zone has corners which are known as K points, and two of them are

explicitly labeled K_+ and K_- in Fig. 1.7. Close to these points, the dispersion is linear and electronic properties may be described by a Dirac-like Hamiltonian. We discuss more in details in next section. Note also that the band structure displays a large asymmetry between the conduction and valence bands that is most distinct in the vicinity of the Γ point.

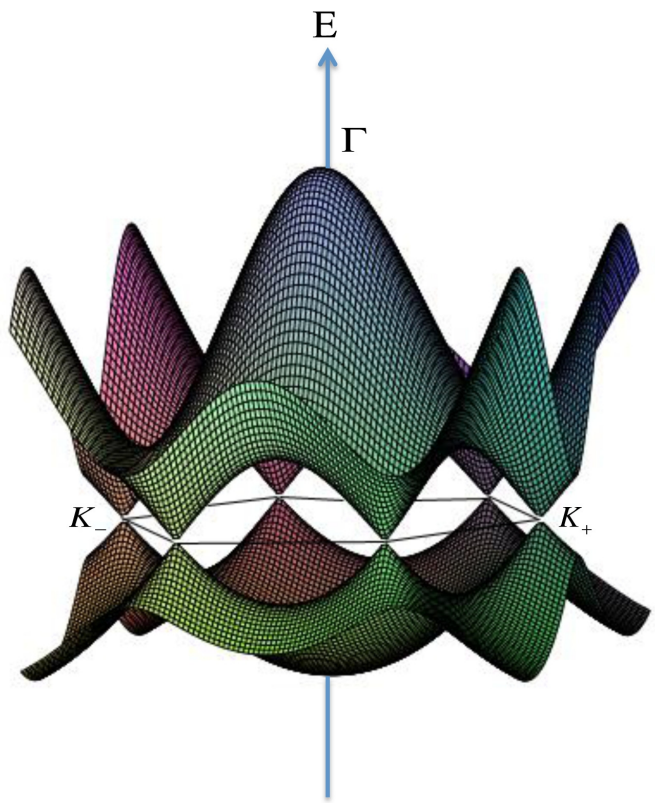

Figure 1.8: The low-energy band structure of monolayer graphene (1.57) taking into account nearest-neighbor hopping with parameter $\gamma_0 = 3.033$ eV, nearest-neighbor overlap parameter $s_0 = 0.129$, and orbital energy $s_0 = 0.129$ [11]. The plot shows the bands calculated in the vicinity of the first Brillouin zone, with conduction and valence bands touching at six corners of the Brillouin zone, two of them are labeled K_+ and K_- . Label Γ indicates the center of the Brillouin zone. Adopted from[27]

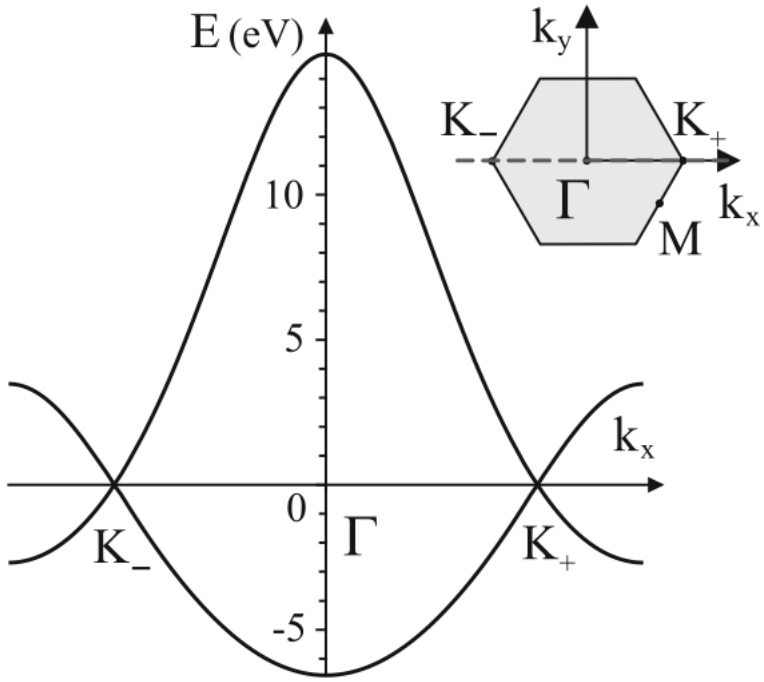

Figure 1.9: The low-energy band structure of monolayer graphene (1.57) taking into account nearest-neighbor hopping with parameter $\gamma_0 = 3.033$ eV, nearest-neighbor overlap parameter $s_0 = 0.129$, and orbital energy $s_0 = 0.129$ [14]. The plot shows a cut through the band structure Fig. 1.7, plotted along the k_x axis intersecting points K_- , Γ , and K_+ in the Brillouin zone, shown as the dotted line in the inset

This comes out from the nonzero overlap parameter s_0 appearing in (1.57). For a comparison see Fig 1.10 in the case $s_0 = 0$

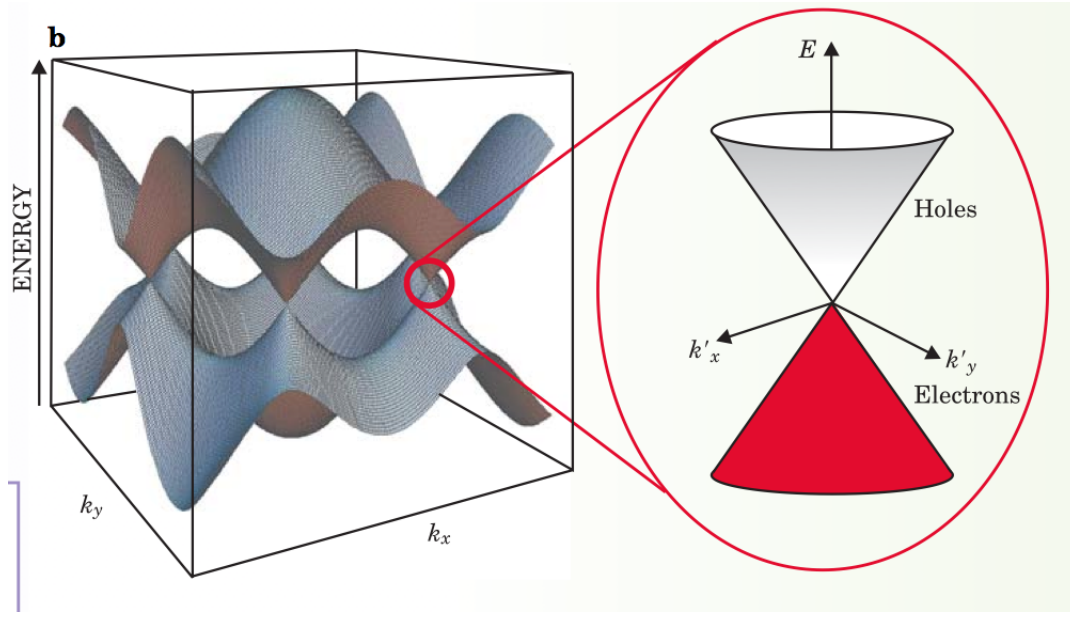

Figure 1.10: (a) Graphene band structure. (b) Enlargment of the band structure close to the K and K' points showing the Dirac cones. Adpated from Wilson, 2006 [17]

The tight-binding model described here cannot be used to determine the values of parameters such as γ_0 and s_0. They must be determined either by an alternative theoretical method, such as density-functional theory, or by comparison of the tightbinding model with experiments [27]. Note, however, that the main qualitative features described in this chapter do not depend on the precise values of the parameters quoted.

1.5.4 Density of States

It is well known that the total DOS, define as:

$$N(E) = \sum_k \delta(E - E(k)) \ , \tag{1.58}$$

is proportional to the imaginary part of the single-particle, time-independent Green's function connecting a state to itself, i.e.

$$N(E) = -\frac{1}{\pi}\Im\left\{ \mathrm{Tr}\left[\lim_{\epsilon\to 0^+} \mathcal{G}(\mathbf{r}, \mathbf{r}; E + i\epsilon) \right]\right\} \ , \tag{1.59}$$

The definition of the Green's function operator is

$$\hat{\mathcal{G}(z)} = \frac{1}{z\hat{I} - \hat{H}} = \sum_k \frac{|k\rangle\langle k|}{z - E(k)} \ , \tag{1.60}$$

where $z = E + i\epsilon$. The Green's function connecting a lattice site l to itself is then

$$\mathcal{G}(l, l; z) = \sum_k \frac{\langle l|k\rangle\langle k|l\rangle}{z - E(k)} \ , \tag{1.61}$$

which can be converted to a continuous sum over the first Brillouin zone. The DOS is then only the imaginary part of the trace of this function in the limit as $\epsilon \to 0^+$. For hexagonal lattice, Horiguchi [18] showed that the Green's function and therefore the DOS are expressible analytically in terms of complete elliptic integrals of the first kind. The hexagonal or honeycomb lattice is composed of two site types, which form two interpenetrating triangular lattices. The Hamiltonian eigenfunctions can thus be split into two groups, one summing over sites of type A and the other over sites of type B. The two sites result in two energy bands. If consider just nearest neighbour hopings γ_0, the matrix representation of the operator $z\hat{I} - \hat{H}$ by equation (1.54), in terms of these eigenfunctions and by assumption

of $\epsilon_{2p} = 0$, is

$$H_1 = \begin{pmatrix} 0 & -\gamma_0 f(\mathbf{k}) \\ -\gamma_0 f^*(\mathbf{k}) & 0 \end{pmatrix} \quad , \tag{1.62}$$

The DOS is then calculated by taking the trace of the inverse of the matrix $z\hat{I} - \hat{H}$. Hence the total DOS becomes

$$N(E) = -\frac{1}{\pi}\Im\left[\lim_{\epsilon\to 0^+}\int_{1stBZ} d\mathbf{k}\,\frac{z}{z^2 - {\gamma_0}^2|f^*(\mathbf{k})|^2}\right] \quad , \tag{1.63}$$

it is possible to derive an analytical expression for the density of states per unit cell, which has the form [31]

$$\rho(E) = -\frac{4}{\pi^2}\frac{|E|}{{\gamma_0}^2}\frac{1}{\sqrt{Z_0}}\mathbf{F}\left(\frac{\pi}{2}, \sqrt{\frac{Z_1}{Z_0}}\right) \quad , \tag{1.64}$$

Where

$$Z_0 = \begin{cases} \left(1 + |\frac{E}{\gamma_0}|\right)^2 - \frac{[(E/\gamma_0)^2-1]^2}{4}, & -\gamma_0 \leqslant E \leqslant \gamma_0 \\ 4|\frac{E}{\gamma_0}| & -3\gamma_0 \leqslant E \leqslant \gamma_0 \ \vee \ \gamma_0 \leqslant E \leqslant 3\gamma_0 \end{cases} \tag{1.65}$$

and

$$Z_1 = \begin{cases} 4|\frac{E}{\gamma_0}|, & -\gamma_0 \leqslant E \leqslant \gamma_0 \\ \left(1 + |\frac{E}{\gamma_0}|\right)^2 - \frac{[(E/\gamma_0)^2-1]^2}{4}, & -3\gamma_0 \leqslant E \leqslant \gamma_0 \ \vee \ \gamma_0 \leqslant E \leqslant 3\gamma_0 \end{cases} \tag{1.66}$$

where $\mathbf{F}(\pi/2, x)$is the complete elliptic integral of the first kind. Close to the Dirac

point, the density of states per unit cell is given by(with a degeneracy of 4 included)

$$\rho(E) = -\frac{2A_c}{\pi}\frac{|E|}{v^2{}_F} \quad , \tag{1.67}$$

where A_c is the unit cell area given by $A_c = 3\sqrt{3}a^2/2$ and $v_F = 3\gamma_0/2 \approx 1 \times 10^6 m/s$. It is interesting to say that the density of states for graphene is different from the density of states of carbon nanotubes (Saito et al.,). The latter shows $1/\sqrt{E}$ singularities due to the 1D nature of their electronic spectrum, which happens due to the quantization of the momentum in the direction perpendicular to the tube axis. From this view, Graphene nanoribbons, which also have momentum quantization perpendicular to the ribbon length, have properties similar to carbon nanotubes.

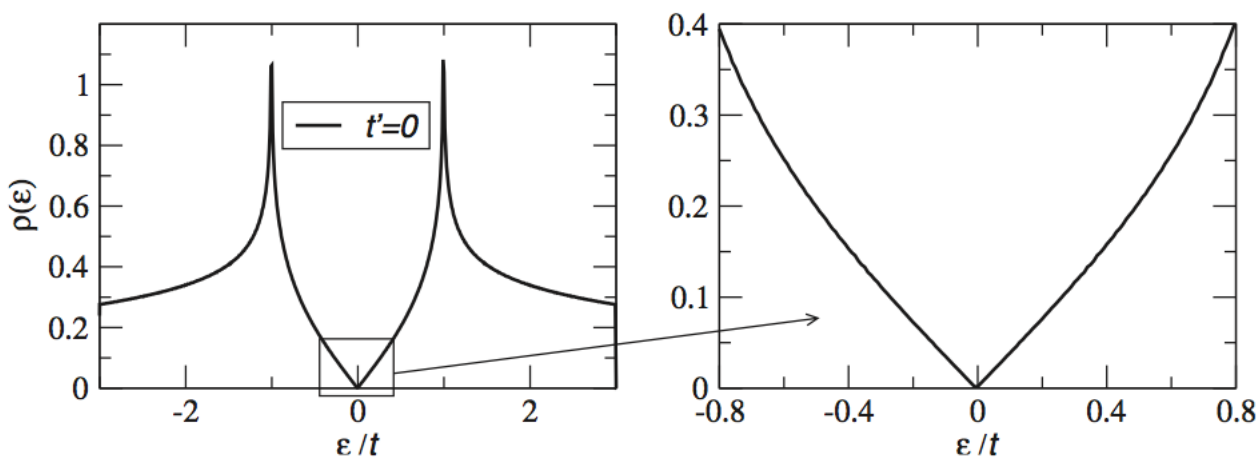

Figure 1.11: Density of states per unit cell as a function of energy (in units of γ_0) . Also shown is a zoom-in of the density of states close to the neutrality point of one electron per site. For the case γ'(second-nearest hopping)=0, the electron-hole nature of the spectrum is apparent and the density of states close to the neutrality point can be approximated by $\rho(\epsilon) \propto |\epsilon|$

Fig 1.11 shows the 2D DOS for the honeycomb lattice. The bandwidth of the DOS is 6eV, hence γ_0 controls the bandwidth and is a measure of the degree to which hopping between nearest neighbours is facilitated. In graphite, the Fermi level is very close (within 0024 eV-see Charlier et al. [19] to constant site energy ϵ_i, so that $E = 0$ approximates the Fermi level. Because the effective width of the bandgap at E_F is zero, the graphite monolayer is classified as a zero-overlap semi-metal, in that it is neither conductor nor insulator. The honeycomb DOS exhibits the expected logarithmic 2D Van Hove singularities and is symmetrical about $E = 0$, a consequence of the bipartite nature of the lattice and nearest neighbor hoping only.

1.6 Massless Chiral Quasiparticles in Monolayer Graphene

1.6.1 The Dirac-Like Hamilitonian

As described in the previous sections, the electronic band structure of monolayer graphene, Figs. 1.8, 1.9, is gapless, with crossing of the bands at points K_+ and K_- located at corners of the Brillouin zone. In this section, it will be shown that electronic properties near these points may be expressed by a Dirac-like Hamiltonian. Although the first Brillouin zone has six corners, only two of them are nonequivalent. In this section, we select points K_+ and K_-, Figs. 1.8, 1.9, as a nonequivalent pair. It is possible to connect two of the other corners to K_+ using a reciprocal lattice vector (hence, the other two are equivalent to K_+), and it is possible to connect the remaining two corners to K_- using a reciprocal lattice vector (therefore, the remaining two are equivalent to K_-), but it is not possible to connect K_+ and K_- with a reciprocal lattice vector. To distinguish between K_+

and K_-, we will use an index $\eta = \pm 1$. Using the values of the primitive reciprocal lattice vectors $\mathbf{b}_1$ and $\mathbf{b}_2$, (8.2), it may be seen that the wave vector corresponding to point K_η is given by

$$\mathbf{K}_\eta = \eta \left(\frac{4\pi}{3a} , 0 \right) , \tag{1.68}$$

Note that the neighborhoods of the K points are often called valleys using nomenclature from semiconductor physics [27].

In the tight-binding model, coupling between the A and B sublattices is expressed by the off-diagonal matrix element H_{AB}, (1.50), that is proportional to parameter γ_0 and the function $f(\mathbf{k})$, (1.47). Exactly at the K_η point, $\mathbf{k} = \mathbf{K}_\eta$, the latter is equal to

$$f(\mathbf{K}_\eta) = e^0 + e^{i\eta 2\pi/3} + e^{-i\eta 2\pi/3} = 0 \ , \tag{1.69}$$

This signifies that there is no coupling between the A and B sublattices exactly at the K_η point. Since the two sublattices are both hexagonal Bravais lattices of carbon atoms, they support the same quantum states, leading to a degeneracy point in the spectrum at K_η , Figs. 1.8, 1.9.

The exact cancelation of the three factors describing coupling between the A and B sublattices, (1.59), no longer holds when the wave vector is not exactly equal to that of the K_η point. One introduces a momentum $\mathbf{p}$ that is measured from the center of the K_η point,

$$\mathbf{p} = \hbar \mathbf{k} - \hbar \mathbf{K}_\eta \ . \tag{1.70}$$

Then the coupling between the A and B sublattices is proportional to

$$f(\mathbf{k}) = e^{i\,p_y\,a/\,\sqrt{3}\hbar} + 2e^{-i\,p_y\,a/\,\sqrt{3}\hbar}\,\cos\left(\frac{2\pi\eta}{3} + \frac{p_x\,a}{2\hbar}\right)\,, \tag{1.71}$$

$$\approx \left(1 + \frac{i\,p_y\,a}{\sqrt{3}\hbar}\right) + 2\left(1 - \frac{i\,p_y\,a}{2\,\sqrt{3}\hbar}\right)\left(-\frac{1}{2} - \frac{\eta\,\sqrt{3}\,p_x\,a}{4\hbar}\right)\,, \tag{1.72}$$

$$\approx -\frac{\sqrt{3}a}{2\hbar}\left(\eta\,p_x - i\,p_y\right)\,, \tag{1.73}$$

where it is kept only linear terms in the momentum $\mathbf{p} = (p_x,\, p_y)$, an approximation that is valid close to the K_η point, i.e. for $pa/\hbar \ll 1$, where $p = |\mathbf{p}| = (p_x^2 + p_y^2)^{1/2}$. Using this approximate expression for the function $f(\mathbf{k})$, the transfer integral matrix (1.54) in the vicinity of point K_η becomes

$$H_1 = v_F \begin{pmatrix} 0 & \eta p_x - i\,p_y \\ \eta p_x + i\,p_y & 0 \end{pmatrix}\,. \tag{1.74}$$

Here, it used $\epsilon_{2p} = 0$ [14], which defines the zero of the energy axis to coincide with the energy of the $2p_z$ orbital.

Within the linear-in-momentum approximation for $f(\mathbf{k}$, (1.63), the overlap matrix S_1 may be regarded as a unit matrix, because its off-diagonal elements, proportional to s_0, only contribute quadratic-in-momentum terms to the energy $E_\pm$, (1.57). Since S_1 is approximately equal to a unit matrix, (1.27) becomes $H_1\,\psi = E\,\psi$, indicating that H_1, (1.64), is an effective Hamiltonian for monolayer graphene at low-energy. The energy eigenvalues and eigenstates of H_1 are given by [27]

$$E_{\pm} = \pm vp\,, \qquad \psi_{\pm} = \frac{1}{\sqrt{2}}\begin{pmatrix} 1 \\ \pm\eta e^{i\eta\varphi} \end{pmatrix} e^{i\,\mathbf{p}\cdot\mathbf{r}/\hbar}\ . \tag{1.75}$$

where± refer to the conduction and valence bands, respectively. Here φ is the polar angle of the momentum in the graphene plane, $\mathbf{p} = (p_x\,, p_y) = p\,(\cos\varphi\,,\ \sin\varphi)$.

1.6.2 Pseudospin and Chirality in Graphene

The effective Hamiltonian (1.74) and eigenstates (1.75) in the vicinity of the K_η point have two components, reminiscent of the components of spin-1/2. Referring back to the original definitions of the components of the column vector , (1.16) and (1.26), prooves that this is not the physical spin of the electron, but a degree of freedom related to the relative amplitude of the Bloch function on the A or B sublattice. This degree of freedom is called pseudospin. If all the electronic density was located on the A sublattice, Fig. 1.12a, this could be viewed as a pseudospin up state (pointing upwards out of the graphene sheet) $|\uparrow\rangle = (1,0)^T$, whereas density solely on the B sublattice corresponds to a pseudospin down state (pointing downwards out of the graphene sheet) $|\downarrow\rangle = (1,0)^T$,[27] Fig.12b.

In graphene, electronic density is normally shared equally between A and B sublattices, Fig. 1.12c, so that the pseudospin part of the wave function is a linear combination of up and down, and it lies in the plane of the graphene sheet.

Not only do the electrons possess the pseudospin degree of freedom, but also they are chiral, signifying that the orientation of the pseudospin is related to the direction of the electronic momentum **p**. This is reflected in the fact that the amplitudes on the A or B sublattice of the eigenstate (1.75) depend on the polar angle φ. It is convenient to use

Pauli spin matrices in the A/B sublattice space, σ_i where $i = 1 \cdots 3$, to write the effective Hamiltonian (1.74) as

$$H_{1,\eta} = v\,(\eta\,\sigma_x\,p_x + \sigma_y\,p_y)\ . \tag{1.76}$$

If we define a pseudospin vector as $\boldsymbol{\sigma} = (\sigma_x, \sigma_y, \sigma_z,)$, and a unit vector as $\hat{\mathbf{n}}_1 = (\eta\,\cos\varphi,\ \sin\varphi,\ 0)$, then the Hamiltonian becomes $H_{1,\eta} = vp\,\boldsymbol{\sigma}\cdot\hat{n}$, stressing that the pseudospin $\boldsymbol{\sigma}$ is linked to the direction $\hat{\mathbf{n}}_1$. The chiral operator $\boldsymbol{\sigma}\cdot\hat{\mathbf{n}}_1$ projects the pseudospin onto the direction of quantization $\hat{\mathbf{n}}_1$: eigenstates of the Hamiltonian are also eigenstates of $\boldsymbol{\sigma}\cdot\hat{\mathbf{n}}_1$ with eigenvalues ± 1, $\boldsymbol{\sigma}\cdot\hat{\mathbf{n}}_1\psi_\pm = \pm\psi_\pm$. An alternative way of expressing this chiral property of electrons is to explicitly calculate the expectation value of the pseudospin operator $\langle\boldsymbol{\sigma}\rangle = \Big(\langle\sigma_x\rangle, \langle\sigma_y\rangle, \langle\sigma_z\rangle\Big)$ with respect to the eigenstate $\psi_\pm$, (1.75). The result, $\langle\boldsymbol{\sigma}\rangle_{e/h} = \pm(\eta\,\cos\varphi,\ \sin\varphi,\ 0)$, shows the link between pseudospin and momentum. For valley K_+, the pseudospin in the conduction band $\langle\boldsymbol{\sigma}\rangle_e$ is parallel to the momentum, whereas the pseudospin in the valence band $\langle\boldsymbol{\sigma}\rangle_h$ is antiparallel to it, Fig. 1.12d.

If the electronic momentum $\mathbf{p}$ rotates by angle φ, then adiabatic evolution of the chiral wave function $\psi_\pm$, (1.75), produces a matching rotation of the vector $\hat{\mathbf{n}}_1$ by angle φ [27]. This is related to the so-called Berrys phase [25; 26].

The chiral properties of low-energy electrons in graphene places an additional constraint on their scattering properties. If a given potential does not break the A-B symmetry, then it is unable to affect the pseudospin degree of freedom which must, then, be conserved upon scattering[27]. Considering only the pseudospin part of the chiral wave function $\psi_\pm$, (1.75), the probability to scatter in a direction φ , where $\varphi = 0$ is the forward direction, is proportional to [27] $w(\varphi) = |\langle\psi_\pm(\varphi)|\psi_\pm(0)\rangle|^2$. For monolayer graphene,

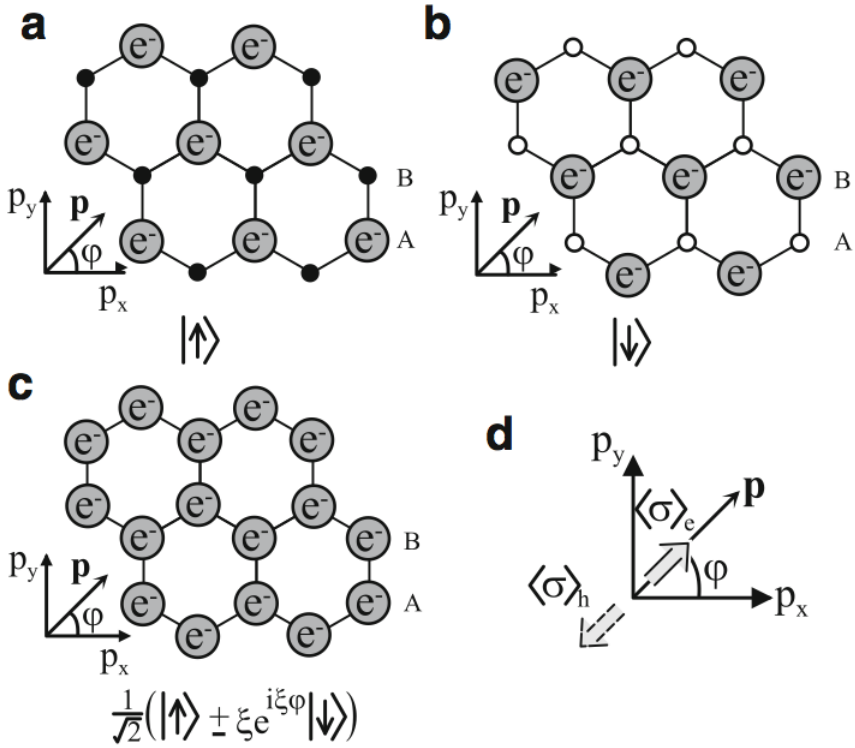

Figure 1.12: Schematic representation of the pseudospin degree of freedom: (**a**) electronic density solely on the A sublattice can be viewed as a pseudospin up state, whereas (**b**) density solely on the B sublattice corresponds to a pseudospin down state; (**c**) in graphene, electronic density is usually shared equally between A and B sublattices, so that the pseudospin part of the wave function is a linear combination of up and down, with amplitudes dependent on the direction of the electronic momentum **p**; (**d**) at valley K_+, the pseudospin $\langle\boldsymbol{\sigma}\rangle_e$ in the conduction band is parallel to the momentum, whereas the pseudospin $\langle\boldsymbol{\sigma}\rangle_h$ in the valence band is anti-parallel to the momentum. Adopted from [27]

$w(\varphi) = \cos^2(\varphi/2)$, Fig. 1.13a. This is anisotropic, and displays an absence of backscattering $w(\pi) = 0$ [22; 23; 24]: scattering into a state with opposite momentum is prohibited because it requires a reversal of the pseudospin. Such conservation of pseudospin is at the heart of anisotropic scattering at potential barriers in graphene monolayers [28; 29],

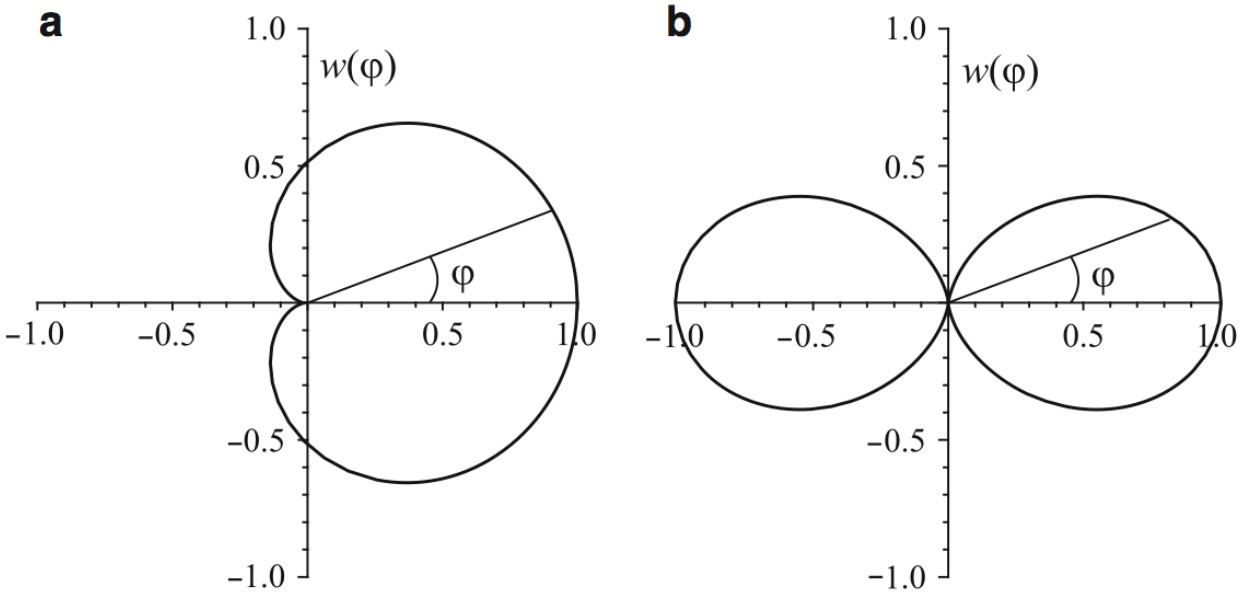

Figure 1.13: Anisotropic scattering of chiral electrons in graphene: (**a**) angular dependence $w(\varphi) = \cos^2(\varphi/2)$ of the scattering probability off an A-B symmetric potential in monolayer graphene and (**b**) $w(\varphi) = \cos^2(\varphi)$ in bilayer graphene. From [27]

known as Klein tunneling.

1.7 Chiral tunneling and Klein paradox in Graphene

In this section, we address the scattering of chiral electrons in two dimensions by a square barrier [29; 30]. The one-dimensional scattering of chiral electrons was explained earlier in the context on nanotubes [22; 23].

We start by noting that by a gauge transformation the wavefunction $\psi_{\pm,\mathbf{K}'}(\mathbf{k}) = \frac{1}{\sqrt{2}}\begin{pmatrix} e^{-\theta_{\mathbf{k}}/2} \\ \pm e^{\theta_{\mathbf{k}}/2} \end{pmatrix}$ where the $\pm$ signs correspond to the eigenenergies $E = \pm v_F k$, that is, for the π^* and π bands, respectively, and $\theta_{\mathbf{q}} = \arctan(\frac{q_y}{q_x})$[31] :

$$\psi_{\mathbf{K}}(\mathbf{k}) = \frac{1}{\sqrt{2}}\begin{pmatrix} 1 \\ \pm e^{i\theta_k} \end{pmatrix} . \tag{1.77}$$

We further assume that the scattering does not mix the momenta around $\mathbf{K}$ and $\mathbf{K}'$ points. In Fig. 1.14, we demonstrate the scattering process due to the square barrier of width D.

The wave function in the different regions can be written in terms of incident and reflected waves. In region I, one can write [31]

$$\psi_I(\mathbf{r}) = \frac{1}{\sqrt{2}}\begin{pmatrix} 1 \\ se^{i\phi} \end{pmatrix} e^{i(k_x x + k_y y)} + \frac{r}{\sqrt{2}}\begin{pmatrix} 1 \\ se^{i(\pi-\phi)} \end{pmatrix} e^{i(-k_x x + k_y y)} . \tag{1.78}$$

with $\phi = \arctan(k_y/k_x)$, $k_x = k_F \cos\phi$, $k_y = k_F \sin\phi$, and k_F is the Fermi momentum. In region II , we have

$$\psi_{II}(\mathbf{r}) = \frac{a}{\sqrt{2}}\begin{pmatrix} 1 \\ s' e^{i\phi} \end{pmatrix} e^{i(q_x x + k_y y)} + \frac{b}{\sqrt{2}}\begin{pmatrix} 1 \\ s' e^{i(\pi-\phi)} \end{pmatrix} e^{i(-q_x x + k_y y)} . \tag{1.79}$$

with $\theta = \arctan(k_y/q_x)$ and

$$q_x = \sqrt{(V_0 - E)^2/(v_F^2) - k_y^2} , \tag{1.80}$$

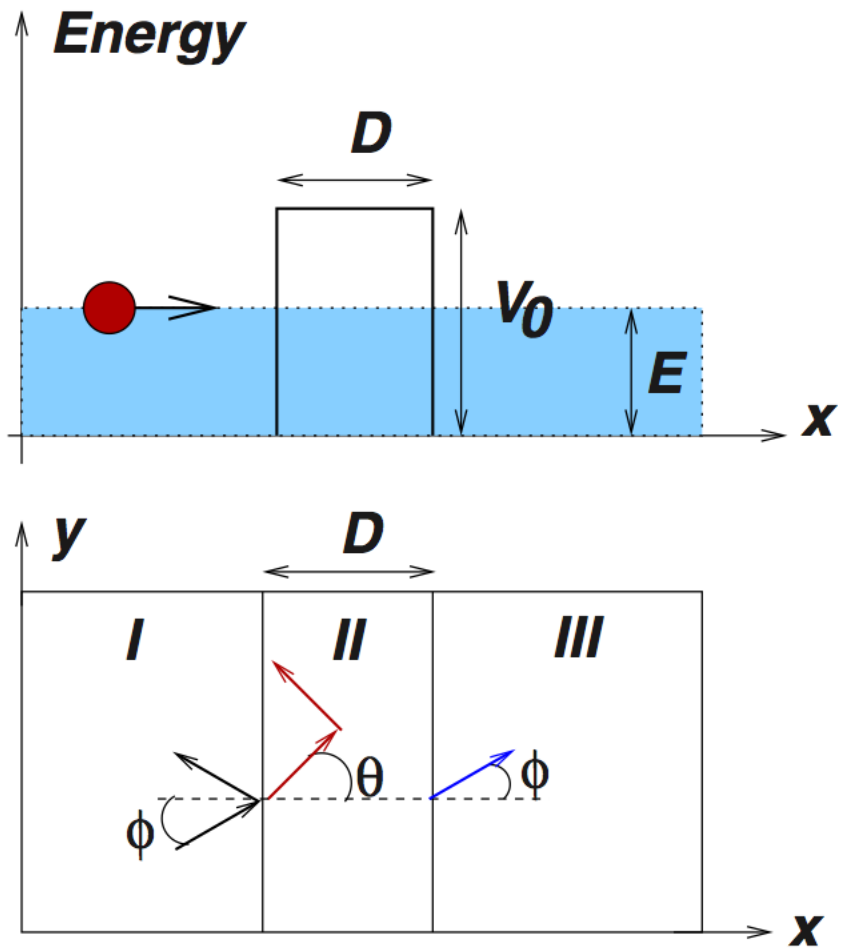

Figure 1.14: Klein tunneling in graphene. Top: schematic of the scattering of Dirac electrons by a square potential. Bottom: definition of the angles ϕ and θ used in the scattering formalism in regions I,II, and III (adapted from [31]).

and finally in region III we have a transmitted wave only [31],

$$\psi_{III}(\mathbf{r}) = \frac{t}{\sqrt{2}} \begin{pmatrix} 1 \\ se^{i\phi} \end{pmatrix} e^{i(k_x x + k_y y)} \ . \tag{1.81}$$

with $s = \mathrm{sgn}(E)$ and $s' = \mathrm{sgn}(E - V_0)$. The coefficients r, a, b, and t are determined from the continuity of the wave function, which implies that the wave function has to obey the conditions $\psi_I(x = 0, y) = \psi_{II}(x = 0, y)$ and $\psi_{II}(x = D, y) = \psi_{III}(x = D, y)$. Unlike the Schrödinger equation, we only need to match the wave function but not its derivative. The transmission through the barrier is obtained from $T(\phi) = tt^*$ and has the form

$$T(\phi) = \frac{\cos^2\theta\,\cos^2\phi}{\left[\cos(Dq_x)\cos\phi\cos\theta\right]^2 + \sin^2(Dq_x)(1 - ss'\,\sin\phi\,\sin\theta)^2}\ . \tag{1.82}$$

This expression does not take into consideration a contribution from evanescent waves in region II, which is usually negligible, unless the chemical potential in region II is at the Dirac energy.

Figure 1.15 shows examples of the angular dependence of transmission probability T in monolayer and bilayer. Note that $T(\phi) = T(-\phi)$, and for values of Dq_x satisfying the relation $Dq_x = n\pi$, with n an integer, the barrier becomes completely transparent since $T(\phi) = 1$, independent of the value of ϕ. Also, for normal incidence $\phi \to 0$ and $\theta \to 0$ and any value of Dq_x, one obtains $T(0) = 1$, and the barrier is again totally transparent. This result is a manifestation of the Klein paradox [32; 33] and does not occur for nonrelativistic electrons. In this latter case and for normal incidence, the transmission is always smaller than 1.

Bibliography

[1] Novoselov, K.S., Geim, A.K., Morozov, S.V., Jiang, D., Zhang, Y., Dubonos, S.V., Grigorieva, I.V., Firsov, A.A.: Electric field effect in atomically thin carbon films.

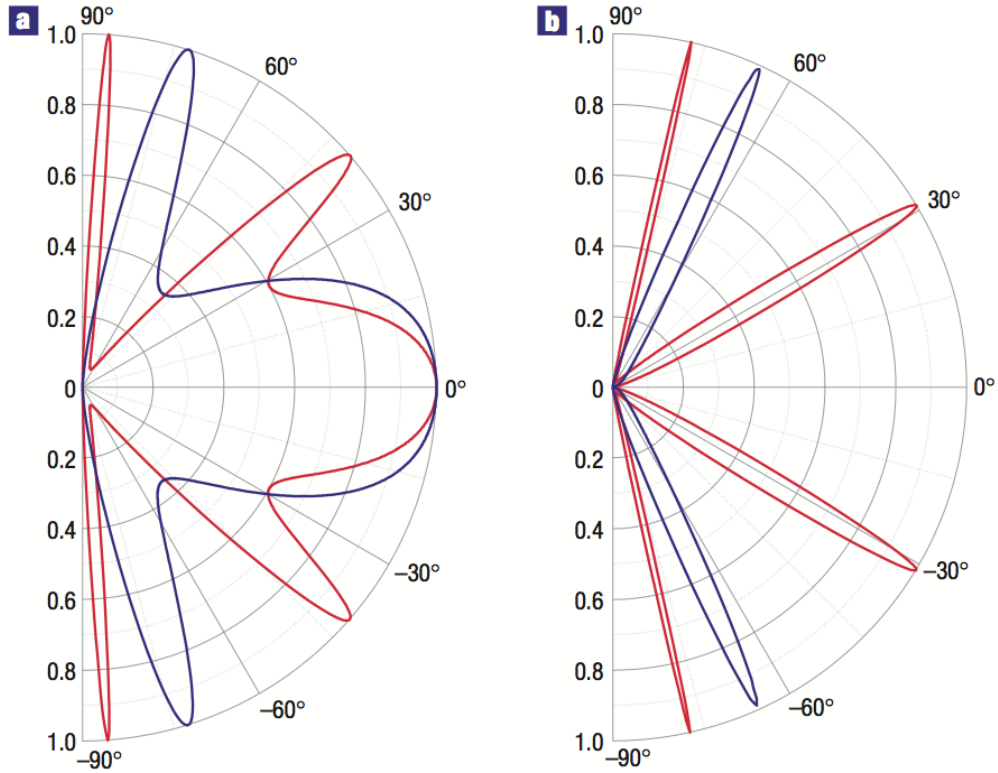

Figure 1.15: **Klein-like quantum tunnelling in graphene systems:** Transmission probability T through a 100-nm-wide barrier as a function of the incident angle for single- (**a**) and bi-layer (**b**) graphene. The electron concentration n outside the barrier is chosen as 0.5×10^{12} cm^2 for all cases. Inside the barrier, hole concentrations p are 1×10^{12} and 3×10^{12} cm^2 for red and blue curves, respectively (such concentrations are most typical in experiments with graphene). This corresponds to the Fermi energy E of incident electrons ≈ 80 and 17meV for single- and bi-layer graphene, respectively, and $\lambda \approx 50nm$. The barrier heights V_0 are (**a**) 200 and (**b**) 50 meV (red curves) and (**a**) 285and (**b**) 100meV (blue curves). [adopted from Katsnelson et al. [29]

Science **22**, 666 (2004)

[2] Geim, A.K., Novoselov, K.S.: The rise of graphene. Nat. Mat. **6**, 183 (2007).

[3] Shankar, R.: Renormalization group approach to interacting fermions. Rev. Mod. Phys. **66**, 129 (1994)

[4] Baym, G., Pethick, C.: *Landau Fermi-Liquid Theory*. Wiley, New York (1991)

[5] Castro Neto, A.H., Guinea, F., Peres, N.M.R.: Drawing conclusions from graphene. Phys. World **19**, 33 (2006)

[6] Gonzalez, J., Guinea, F., Vozmediano, M.A.H.: Non-Fermi liquid behavior of electrons in the half-filled honeycomb lattice: a renormalization group approach.Nucl. Phys. B **424**, 595 (1994)

[7] Baym, G., Chin, S.A.: Landau theory of relativistic Fermi liquids. Nucl. Phys. A **262**, 527 (1976)

[8] Gordon, B.: *Lectures on Quantum Mechanics. Addison-Wesley*, Reading, **MA** (1990)

[9] Pauling, L.: *The Nature of the Chemical Bond. Cornell University Press*, Ithaca (1960)

[10] Castro Neto, A.H., Guinea, F.: Impurity induced spin-orbit coupling in graphene. Phys. Rev. Lett. **103**, 026804 (2009)

[11] Harrison, W.A.: *Elementary Electronic Structure*. World Scientific, Singapore (2005)

[12] Castro Neto, Antonio H.: *Modern Theories of Many-Particle Systems in Condensed*

Matter Physics, Lecture Notes in Physics, **843**. Springer-Verlag Berlin Heidelberg, 2012, p. 117

[13] P.R. Wallace, Phys. Rev. **71**, 622 (1947)

[14] R. Saito, M.S. Dresselhaus, G. Dresselhaus *Physical Properties of Carbon Nanotubes*, (Imperial College Press, London, 1998)

[15] K. Sasaki, S. Murakami, R. Saito, Appl. Phys. Lett. **88**, 113110 (2006)

[16] N.M.R. Peres, F. Guinea, A.H. Castro Neto, Phys. Rev. B **73**, 125411 (2006)

[17] M. Wilson, Physics Today, vol. **59**, issue 1, p. 21

[18] T. Horiguchi, J. Math. Phys. **13**, 1411 (1972)

[19] J.-C. Charlier, J.-P. Michenaud, X. Gonze, J.-P. Vigneron; Phys. Rev. B **44**, 1323713249 (1991)

[20] E. McCann, V.I. Falko, Phys. Rev. Lett. **96**, 086805 (2006)

[21] V.I. Falko, K. Kechedzhi, E.McCann, B.L. Altshuler, H. Suzuura, T. Ando, Solid State Comm. **143** 33 (2007)

[22] T. Ando, T. Nakanishi, R. Saito, J. Phys. Soc. Jpn. **67**, 2857 (1998)

[23] P.L. McEuen, M. Bockrath, D.H. Cobden, Y.-G. Yoon, S.G. Louie, Phys. Rev. Lett. **83**, 5098 (1999)

[24] H. Suzuura, T. Ando, Phys. Rev. Lett. **89**, 266603 (2002)

[25] S. Pancharatnam, Proc. Indian Acad. Sci. A **44**, 247 (1956)

[26] M.V. Berry, Proc. R. Soc. Lond. A **392**, 45 (1984)

[27] Edward McCann.: *Graphene Nanoelectronics: Metrology, Synthesis, Properties and Applications*, NanoScience and Technology. Springer, 2012, p. 237

[28] V.V. Cheianov, V.I. Falko, Phys. Rev. B **74**, 041403(R) (2006)

[29] M.I. Katsnelson, K.S. Novoselov, A.K. Geim, Nature Phys. **2**, 620 (2006)

[30] Katsnelson, M. I., 2007b, Mater. Today **10**, 20.

[31] A. H. Castro Neto, F. Guinea, N. M. R. Peres, K. S. Novoselov, and A. K. Geim; Rev. Mod. Phys. **81**, 109 (2009).

[32] Calogeracos, A., and N. Dombey, 1999, Contemp. Phys. **40**,313.

[33] Itzykson, C., and J.-B. Zuber, 2006, *Quantum Field Theory* Dover, New York.

[34] Riichiro Saito.: *CARBON ALLOYS*, Elsevier Science Ltd, 2003, p. 15

[35] M. O. Goerbig, Electronic properties of graphene in a strong magnetic eld , REVIEWS OF MODERN PHYSICS, **83**, (2011)

CHAPTER II

Electronic Structure of twisted double-layer Graphene

Abstract

In this chapter, we introduce shortly the electronic structure of AA and AB stacked pure bilayer graphene in the absence of magnetic field . The energy band structure is obtained using a tight-binding model with intra-layer and interlayer terms. After that we study electronic structure of rotated bilayer graphene by using of tight-binding method and Green's functions techniques . A perturbative approach which is valid for not too small angles ($\theta \geq 3^\circ$) and states close to Dirac energy is developed. We calculate the self-energy of states of the upper plane due to their coupling with states of the lower plane . We discuss consequences for velocity renormalization and for electron-lifetime due to disorder in one plane. We also calculate and discuss the spatial modulations of density of states. We compare our analytical results to fully numerical calculations, showing good agreement between the two approaches.

2.1 Introduction

Electronic properties of multilayer graphene strongly depend on the stacking order. Periodically stacked multilayer graphene [1; 2; 3; 4; 5; 6] and also arbitrarily stacked multilayer graphene [7; 8] have been reviewed theoretically.

It has been shown that energy gap can be induced by a perpendicular external electric field in ABC-stacked multilayer graphene [9; 10]. In additon, in ABC stacking electron-electron interactions could play an important role due to the appearance of relatively flat bands near the Fermi level [10]. Optical properties of multilayer graphene using absorption spectroscopy have been studied experimentally [11] and theoretically [12; 13; 14; 15] showing characteristic peak positions in optical conductivity depending on stacking sequences. Transport properties of multilayer graphene have been studied theoretically within the coherent potential approximation for averaged local impurities [16; 17] and using Boltzmann transport theory [18; 19].

2.1.1 Stacking Arrangements

In multilayer graphene, there are three distinct stacking arrangements, labeled A, B, and C, classified by the relative position in two-dimensional (2D) plane.

In each plane the honeycomb lattice of a single sheet has two triangular sublattices, labeled by α and β, as illustrated in Fig. 2.1a. (Here we use α and β for sublattices instead of A and B to avoid any confusion with stacking arrangements (A, B, and C.) Different stacking types are obtained by displacing sublattices along the honeycomb edges or by rotating by $\pm 60^0$ about a carbon atom on one of the two sublattices. Special stacking sequences are generated by repeated AB, ABC, and AA stacking, and are called Bernal,

rhombohedral, and hexagonal stacking, respectively.

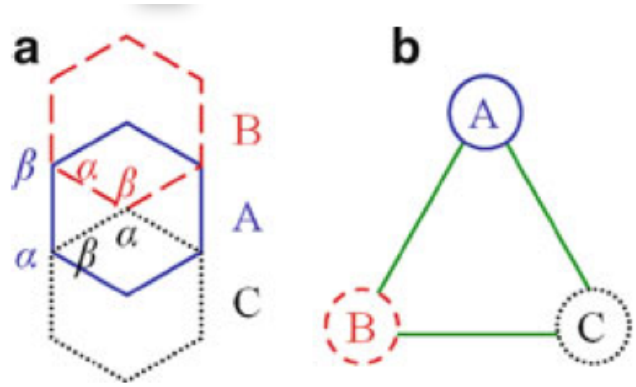

Figure 2.1: (**a**) Three distinct stacking arrangements A, B and C in multilayer graphene and representative sublattices α and β in the A, B, and C layers. (**b**) The stacking triangle where each added layer cycles around. From [56]

Each added layer cycles around the stacking triangle in either the right-handed or the left-handed sense, or stays at the same position in the triangle, as seen in Fig. 2.1b. For example, Bernal (AB) stacking corresponds to moving with a reversal in direction at every step, and rhombohedral (ABC) stacking corresponds to moving with no reversals in direction, while hexagonal (AA) stacking corresponds to not moving around the triangle at all.

2.2 The Tight-Binding Model of AA and AB Bilayers of Graphene

In this section, we present the tight-binding model of AA and AB stacked bilayer graphene. For this purpose, we use the tight-binding model described in chapter 1 in order to generalize the model for monolayer graphene expained in Chapter 1.

Let us consider first the AA stacking, where the two lattices are directly above each other and bonds form between the same sublattices.

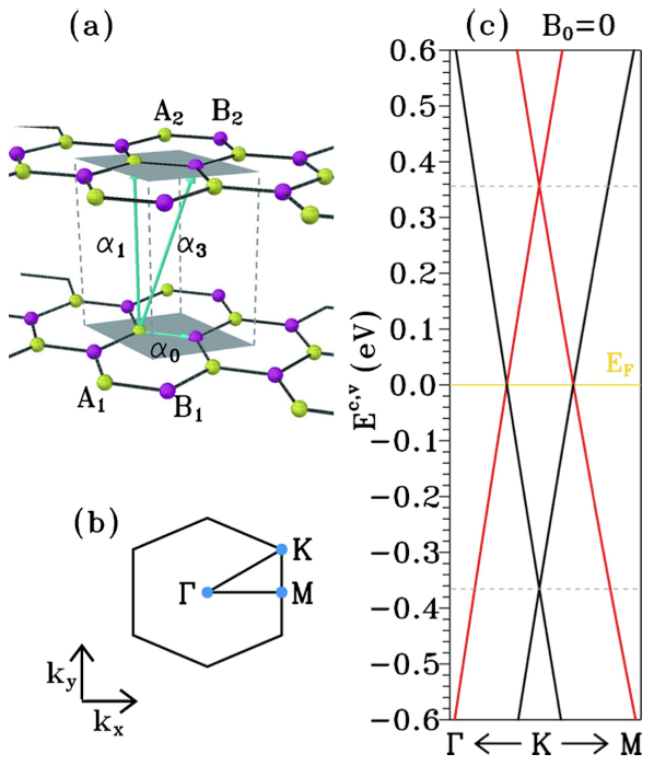

Figure 2.2: (a) The geometric structure, (b) the first Brillouim zone and (c) the low-lying sub bands of AA-stacked graphene. α_0= 2.598 eV is the nearest-neighbor hopping integral and two important interlayer interactions are α_1= 0.361eV and α_3 = -0.032 eV . From [55]

Figure 2.2 shows the geometric configuration of AA-stacked bilayer graphene. The primitive unit cell consists of four sublattices, A_1, B_1 in the first layer and A_2 and B_2 in the second layer. The wave function is linearly combined of four TB functions associated with the four sublattices. Three atomic hopping integrals,α_0= 2.569eV, α_1= 0.3619eV, and α_2= -0.032eV, are taken into account in this work, as indicated in Fig. 2.2(a). The first

Brillouin zone is shown in Fig. 2.2(b). The low-energy electronic structure of AA-stacked bilayer grapheme exhibits two pairs of subbands, as shown in Fig. 2.2(c). The conduction and valence bands of the first (second) pair are symmetric about their crossing energy $-\alpha_1 + \alpha_1\alpha_3/\alpha_0 \approx -0.366\text{eV}$ ($\alpha_1 + \alpha_1\alpha_3/\alpha_0 \approx -0.357\text{eV}$), as indicated by the black (red) lines.

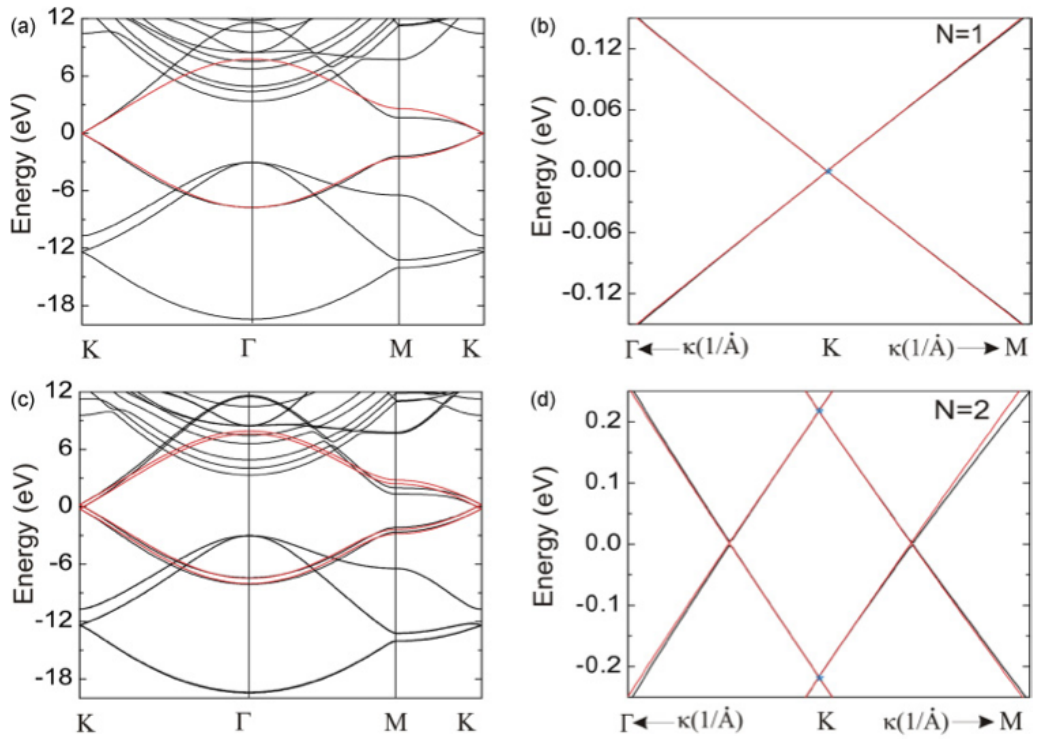

Figure 2.3: Ab initio (black curves) and tight-binding (red curves) band structure along $K\Gamma MK$ of (a) graphene and (c) AA-stacked. Corresponding energy dispersion around the K point for (b) graphene, (d) and AA-stacked bilayer. From [58]

Figure 2.3 shows the band structure of AA-stacked Bilayer graphene near the K point with that of monolayer.

After AA we consider Bernal-stacked bilayer graphene [20; 21; 22] (also called AB-

stacked bilayer graphene). It consists of two parallel layers of carbon atoms, each arranged with a honeycomb lattice as in a monolayer, that are coupled together, Fig. 2.4. There are four atoms in the unit cell, a pair $A1$, $B1$, from the lower layer and a pair $A2$, $B2$, from the upper layer. In Bernal stacking, the layers are arranged so that two atoms, $B1$ and $A2$, are directly below or above each other, whereas the other two atoms, $A1$ and $B2$, do not have a counterpart in the other layer. The primitive lattice vectors $\mathbf{a}_1$ and $\mathbf{a}_2$, and the lattice constant a are the same as for monolayer graphene, and the unit cell, shown in Fig. 2.4a, has the same area in the $x - y$ plane as in the monolayer. Therefore, the reciprocal lattice and first Brillouin zone are the same as in monolayer graphene. The unit cell of bilayer graphene contains four atoms, and, if the tight-binding model includes one p_z orbital per atomic site, there will be four bands near zero energy, instead of the two bands in monolayer graphene.

Essential features of the low-energy electronic band structure may be described by a minimal tight-binding model including nearest-neighbor coupling γ_0 between $A1$ and $B1$, and $A2$ and $B2$, atoms on each layer, and nearest-neighbor interlayer coupling γ_1 between $B1$ and $A2$ atoms that are directly below or above each other,

$$\gamma_1 = \langle \phi_{A2}(\boldsymbol{r} - \boldsymbol{R}_{A2}) | \mathcal{H} | \phi_{B1}(\boldsymbol{r} - \boldsymbol{R}_{B1}) \rangle \tag{2.1}$$

Then we can generalize the treatment of monolayer graphene, (1.54), to write the transfer and overlap integral matrices of bilayer graphene, in a basis with components $A1$, $B1$, $A2$, $B2$, as [57]

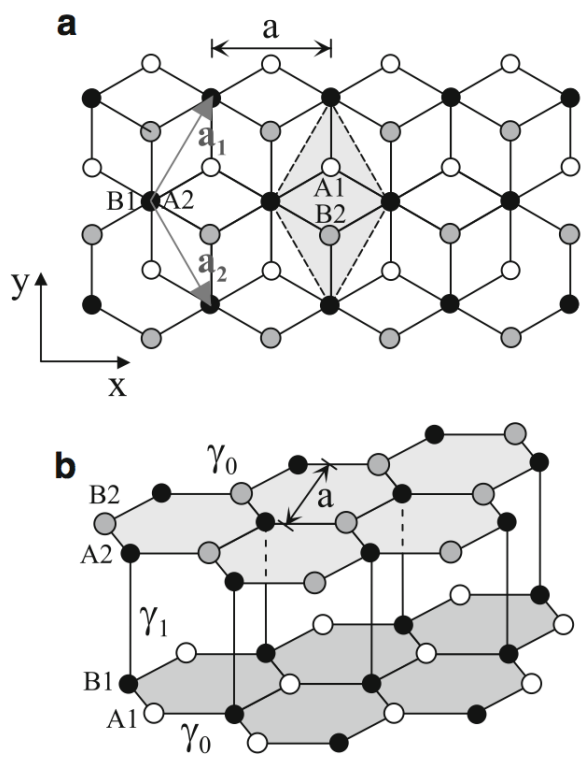

Figure 2.4: Schematic representation of the crystal structure of AB-stacked bilayer graphene: (**a**) plan view with $A1$ (white) and $B1$ atoms (black) on the lower layer, $A2$ (black) and $B2$ atoms (gray) on the upper layer. Vectors $\mathbf{a}_1$ and $\mathbf{a}_2$ are primitive lattice vectors of length equal to the lattice constant a, and the shaded rhombus is a unit cell; (**b**) side view where the parameter γ_0 shows nearest-neighbor coupling within each layer, γ_1 nearest-neighbor coupling between the $B1$ and $A2$ atoms on different layers. From [57]

$$\mathcal{H} = \begin{pmatrix} \epsilon_{2p} & -\gamma_0 f(\boldsymbol{k}) & 0 & 0 \\ -\gamma_0 f^*(\boldsymbol{k}) & \epsilon_{2p} & \gamma_1 & 0 \\ 0 & \gamma_1 & \epsilon_{2p} & -\gamma_0 f(\boldsymbol{k}) \\ 0 & 0 & -\gamma_0 f^*(\boldsymbol{k}) & \epsilon_{2p} \end{pmatrix}, \tag{2.2}$$

$$S = \begin{pmatrix} 1 & s_0 f(\boldsymbol{k}) & 0 & 0 \\ s_0 f^*(\boldsymbol{k}) & 1 & 0 & 0 \\ 0 & 0 & 1 & s_0 f(\boldsymbol{k}) \\ 0 & 0 & s_0 f^*(\boldsymbol{k}) & 1 \end{pmatrix}, \tag{2.3}$$

The upper-left and lower-right 2×2 blocks describe behavior within the lower ($A1/B1$) and upper ($A2/B2$) layers, respectively. The off-diagonal 2×2 blocks, containing parameter γ_1, describe interlayer coupling.

The band structure of bilayer graphene may be determined by solving the secular equation $\det(H - E_j S) = 0$ (1.28). It is plotted in Fig. 2.5 for parameter values $\gamma_0 = 3.033$ eV, $s_0 = 0.129$, $\epsilon_2 p = 0$ [23] and interlayer coupling $\gamma_1 = 0.39$ eV. There are four energy bands, two conduction bands and two valence bands. Overall, the band structure is similar to that of monolayer graphene, Fig.1.9, with each monolayer band split into two by an energy approximately equal to the interlayer coupling γ_1 [22]. The most interesting part of the band structure is in the vicinity of the K points [21], as shown in the left inset of Fig. 2.5, which focuses in on the bands around K_-. At the K point, one of the conduction (valence) bands is split away from zero energy by an amount equal to the interlayer coupling γ_1 ($-\gamma_1$).

The split bands originate from atomic sites $B1$ and $A2$ that have a counterpart atom directly above or below them on the other layer. Orbitals on these pairs of atoms ($B1$ and $A2$) are strongly coupled by the interlayer coupling γ_1 and they form a bonding and anti-bonding pair of bands, split away from zero energy. The remaining two bands, one conduction and one valence band, touch at zero energy: as in the monolayer, there is no

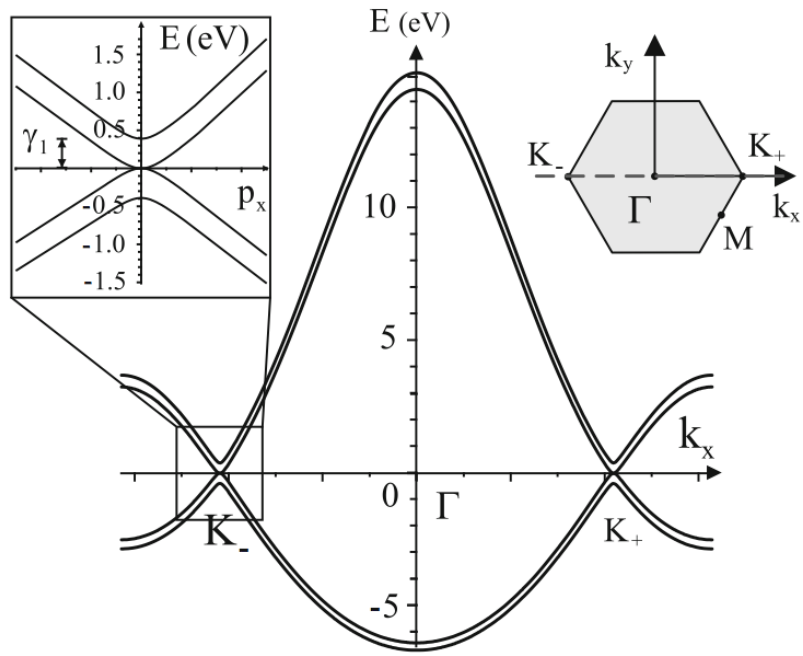

Figure 2.5: The low-energy band structure of bilayer graphene taking into account nearest-neighbor hopping with parameter $\gamma_0 = 3.033$ eV, nearest-neighbor overlap parameter $s_0 = 0.129$, orbital energy $\epsilon_{2p} = 0$ [11], and interlayer coupling $\gamma_1 = 0.39$ eV. The plot shows the bands calculated along the k_x axis intersecting points K_-, Γ , and K_+ in the Brillouin zone, shown as the dotted line in the right inset. The left inset shows the band structure in the vicinity of the point K_- . From [57]

band gap between the conduction and valence bands. In the vicinity of the K points, the dispersion of the latter bands is quadratic $E_\pm \propto \pm|\boldsymbol{k} - \boldsymbol{K}_\eta|^2$, and electronic properties of the low-energy bands may be described by an effective Hamiltonian describing massive chiral particles.

2.3 Rotated Bilayer Graphene

Stacking several layers of Graphene on top of each other, may affect the original electronic structure. Indeed AB or Bernal stacking (as shown previously) destroys the linear dispersion and changes chirality properties even in a bilayer [25; 26; 27; 28; 29; 30] Interaction between layers is then an important question. Yet as we will show in the following it does not systematically destroy interesting properties but on the contrary it can lead to the emergence of very peculiar and new behaviors.

Graphene can be formed in multilayers on SiC [28; 29; 30; 31; 32; 33; 34; 35; 36] but also on metal surfaces such as Ni [37] and in exfoliated flakes[38]) where interactions between successive layers play a crucial role. While on the Si face of SiC, multilayers have an AB stacking and do not show graphene properties[27; 28; 29; 30] , on the C-face, multilayers have been shown to present graphene like properties even when they involve a large number of C planes. ARPES[33; 34; 35; 36] , STM[39] , transport[40] and optical transitions [41] indeed show properties characteristic of a linear graphene like dispersion.

These multilayers are rotated with respect to each other and the rotations show up as Moiré patterns on STM images [34; 42]. The Moiré effect is a well known phenomenon which occurs when repetitive structures (such as screens, grids or gratings) are superposed or viewed against each other. It consists of a new pattern of alternating dark and bright areas which is clearly observed at the superposition, although it does not appear in any of the original structures[24]. Moiré patterns are common in everyday life and often occur when two lattices overlap one another.

This apparent paradox of thick multilayers exhibiting graphene properties was partially solved recently when different theoretical approaches [34; 43; 44; 45; 46; 47; 48; 49; 50]

showed that rotated multilayers are decoupled, at least for large rotation angles.

Going further, theory predicts the existence of three domains: for large rotation angles ($\theta > 20°$) the layers are decoupled and behave as a collection of isolated graphene layers. For intermediate angles $3° < \theta < 20°$ the dispersion remains linear but the velocity is renormalized. What happens at the smallest values of θ is even more puzzling. As already shown by different theoretical groups, for the lowest θ, flat bands appear and result in electronic localization : states of similar energies, belonging to the Dirac cones of the two layers interact, a gap opens at the intersection, associated with saddle points. As the angle decreases, the saddle points come closer to the Dirac point and the renormalization of the velocity increases [43] .

Landau Level (LL) Scanning Tunneling Spectroscopy (STS) gave results in close agreement with theory. The three regimes where observed for CVD graphene grown on Ni: decoupling at large angle, renormalization and van Hove singularities for smaller angles. The singularities appear as peaks on both sides of E_D in STS experiments [37]. On the other hand, if decoupling is indeed observed for multilayers on C face of SiC (ARPES) velocity renormalization has never been shown for this system [35; 36] . The origin of the different behavior between two so similar systems (both are rotated multi- layer graphene) and a possible discrepancy with theory is still subject to intense debate.

In this chapter we developpe a perturbative theory which gives us deeper insight in the regime $3° < \theta < 20°$ (intermediate angles). We recover known results for the velocity renormalization with a better justification for tight-binding model. We analyze also the effect of disorder in one plane on the lifetime of the other plane. We analyze also the spatial modulation of the DOS and demonstrate an increase of the DOS in AA region of

the Moiré. This is a precursor of the localization in the AA region for very low angles less than 3°. This localization has already been observed in some systems and is predicted numerically.

2.3.1 Rotationaly Stacked Commensurate Bilayers

In the following we consider two graphene layers rotated in the plane by an angle θ (Fig. 2.6). We start from an AA bilayer and choose the rotation origin O at an atomic site. A commensurate structure can be defined if the rotation changes a lattice vector $\overrightarrow{OB}(m,n)$ to $\overrightarrow{OB'}(n,m)$ with n,m the coordinates with respect to the basis vectors $\mathbf{a}_1(\sqrt{3}/2,-1/2)$ and $\mathbf{a}_2(\sqrt{3}/2,1/2)$. The rotation angle is then defined as

$$cos\theta = \frac{n^2+4nm+m^2}{2(n^2+nm+m^2)} \tag{2.4}$$

and the commensurate cell vectors correspond to

$$\vec{t} = \overrightarrow{OB'} = n\mathbf{a}_1 + m\mathbf{a}_2; \;\; t' = -m\mathbf{a}_1 + (n+m)\mathbf{a}_2 \;. \tag{2.5}$$

The commensurate unit cell contains $N = 4(n^2+nm+m^2)$ atoms Fig(2.7) . A cell defined in this way is the smallest cell corresponding to one angle provided that n and m are prime numbers. The rotation angle is a good parameter to describe the system but the number of atoms is not since cells of equivalent size can be found for different angles. Indeed, large cells can be obtained for $\theta \sim 0$ large n and m and small $|m-n|$ but also for large angles $\theta \sim 30°$ then $|m-n|$ is large [52] A good way to name the rotated layers is to give the (m,n) couple defined above, that is what we use in this chapter.

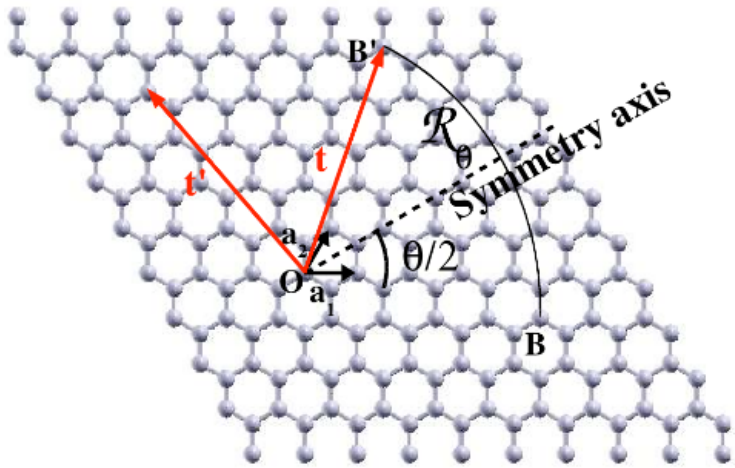

Figure 2.6: Commensurate cell vectors of (n, m) bilayer:

$\theta = 60°$ is the perfect AB stacking. θ close to 60° is obtained for $n = 1(m = 1)$ and large $m(n)$.

Two limit cases have to be considered: small or large angles of rotation. Small rotation angles lead to well defined AA and AB regions and then to a Moiré pattern (Figure 2.8) that can be seen on STM images [34; 42] while a blurred pattern is obtained for larger rotation angles Fig(2.7).

From the periodicity of superlattices, the misorientation between the top and underlying graphene sheets can be calculated using the simple Moiré rotation-pattern assumption: The periodicity, L, of the resulting Moiré hexagonal structure is related to the misorientation angle, θ , between the two layers of the hexagonal lattice, with lattice constant a_0, as [34]

$$L = \frac{a_0}{2\ sin(\theta/2)} \approx \frac{a_0}{\theta} \tag{2.6}$$

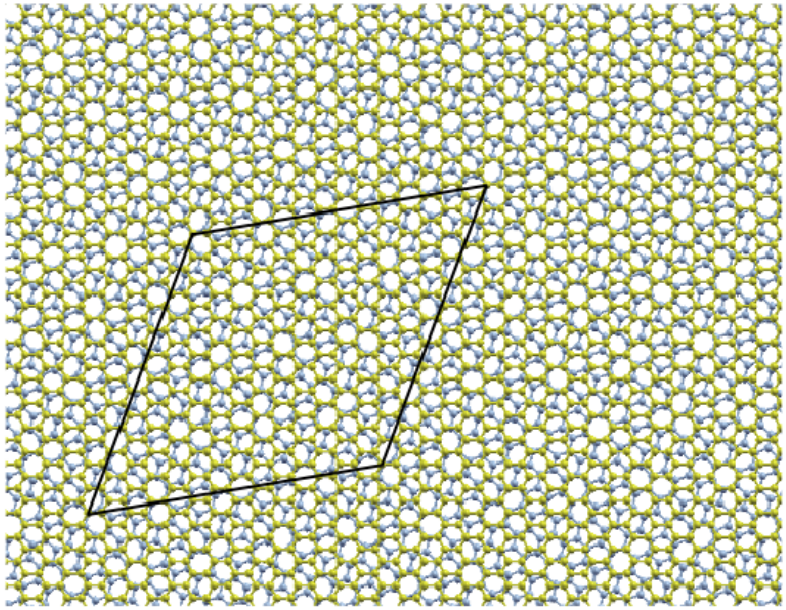

Figure 2.7: Moiré pattern for small θ ($\theta \leq 10°$) left: (6.7) bilayer: $\theta = 5.08°$, $N = 508$ atoms; right: (5.9) bilayer: $\theta = 18.73°$, $N = 604$ atoms. Full (dashed) line circle AB (AA) region.

For small angles, if the rotation axis, perpendicular to the planes, passes through atomic positions in both layers, atoms in the four corners of the supercell are directly superimposed (Figure 2.8) [50]. This corresponds to the so-called AA stacking. For cells (n, m) such that $m = n + 1$, zone with Bernal AB stacking are located at $1/3$ and $2/3$ of the long diagonal (Figure 2.7) [50].

2.4 Tight-Binding Model and Hamiltonian

In the tight-binding scheme only p_z orbitals are taken into account since we are interested in electronic states close to the Fermi level. Since the planes are rotated, neighbors

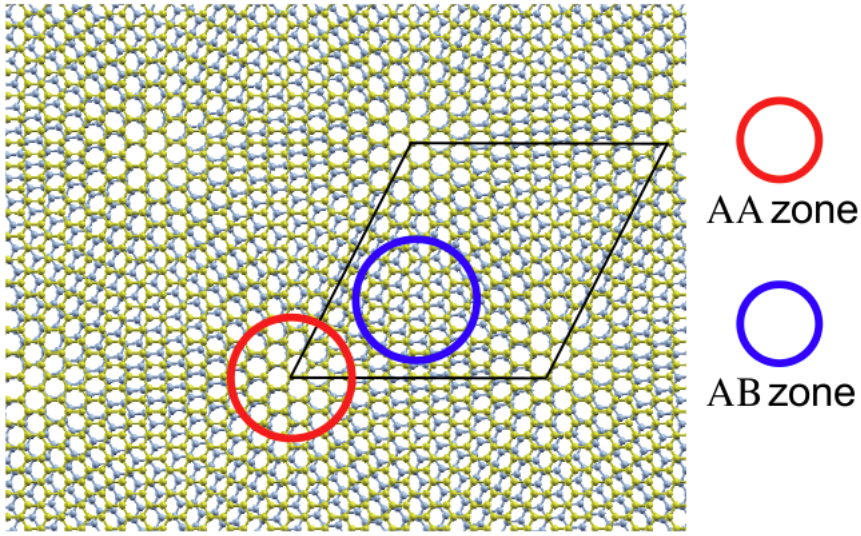

Figure 2.8: Commensurate bilayer cell $(n, m) = (5, 9)$ for a rotation of $\theta = 18.73°$.

are not on top of each other (as is the case in the Bernal AB stacking). Interlayer interactions are then not restricted to $pp\sigma$ terms but some $pp\pi$ terms have also to be introduced [50].

The first thing is to compete the coupling between two states of two planes. Let us consider normalized Bloch states made of atomic orbitals A or B in plane α. One has

$$|\vec{K_A}\rangle_\alpha = \frac{1}{\sqrt{N}} \sum_{\vec{R}} e^{i\vec{K}\cdot\vec{R_A}} |A, R\rangle_\alpha \tag{2.7}$$

$$|\vec{K_B}\rangle_\alpha = \frac{1}{\sqrt{N}} \sum_{\vec{R}} e^{i\vec{K}\cdot\vec{R_B}} |B, R\rangle_\alpha \tag{2.8}$$

Where N is the number of unit cells of the crystal and the summation is perfumed on all cells of crystal. $\vec{R}$ is the position of A atom of the cell. In the following A or B are indicated by ε according to the following convention

$$\varepsilon = \begin{cases} +1 & \text{for A-atom} \\ -1 & \text{for B-atom} \end{cases} \tag{2.9}$$

$$\alpha = \begin{cases} +1 & \text{upper plane} \\ -1 & \text{lower plane} \end{cases} \tag{2.10}$$

We want to compute the matrix element of the Hamiltonian between two normalized Bloch states $|\varepsilon\vec{k}\rangle_+$ and $|\varepsilon'\vec{k}'\rangle_-$:

$$H_c(\varepsilon, \varepsilon'; \vec{k}, \vec{k}') = \langle\vec{k}'\varepsilon'|H_c|\varepsilon\vec{k}\rangle = \ H_c(\vec{k}'\varepsilon'; \vec{k}\varepsilon) \tag{2.11}$$

Because H_c is Hermitian, then we have:

$${}_+\langle\vec{k}'\varepsilon'|H_c|\varepsilon\vec{k}\rangle_- = ({}_-\langle\varepsilon\vec{k}|H_c|\langle\vec{k}'\varepsilon'\rangle_+)^* \tag{2.12}$$

$$H_c(\varepsilon, \varepsilon'; \vec{k}, \vec{k}') = \sum_{\vec{R},\vec{R}'} e^{i(\vec{K}\cdot\vec{R}-\vec{K}'\cdot\vec{R}')}{}_-\langle\vec{R}'\varepsilon'|H_c|\varepsilon\vec{R}\rangle_+ \tag{2.13}$$

We have:

$$\begin{cases} \vec{r}_{\varepsilon\vec{R}}(\text{position in upper layer}) = \vec{R} & \text{if } \varepsilon = +1 \\ \vec{r}_{\varepsilon\vec{R}} = \vec{R} + \vec{u} & \text{if } \varepsilon = -1 \\ \vec{r'}_{\varepsilon'\vec{R}'}(\text{position in down layer}) = \vec{R}' & \text{if } \varepsilon' = +1 \\ \vec{r'}_{\varepsilon'\vec{R}'} = \vec{R}' + \vec{u'} & \text{if } \varepsilon' = -1 \end{cases} \tag{2.14}$$

Then

$$_{-}\langle \vec{R}'\varepsilon'|H_c|\varepsilon\vec{R}\rangle_{+} = H_c(|\vec{r}_{\varepsilon\vec{R}} - \vec{r'}_{\varepsilon'\vec{R}'}|) \tag{2.15}$$

where $\vec{u}$ and $\vec{u'}$ are vectors connecting the two atoms in the unit cells, i.e. A and B atoms in upper and A' and B' atoms in down layers respectively.

From Fourier transformation we write:

$$H_c(\vec{r}) = \int \widetilde{H}_c(\vec{k})\ e^{i\vec{k}\cdot\vec{r}}\, d^2\vec{k} \tag{2.16}$$

$$\widetilde{H}_c(\vec{k}) = \frac{1}{(2\pi)^2}\int H_c(\vec{r})\ e^{-i\vec{k}\cdot\vec{r}}\, d^2\vec{r} \tag{2.17}$$

Writing

$$H_c|\varepsilon\,\vec{k}\rangle_{+} = \sum_i t(\varepsilon_i\,\vec{k}_i\,,\varepsilon\,\vec{k})\ |\varepsilon_i\,\vec{k}_i\rangle_{-} \tag{2.18}$$

Where $t(\varepsilon_i\,\vec{k}_i\,,\varepsilon\,\vec{k})\ \equiv t_i$ is the transfer matrix element. We find selection rules such that

$$\vec{k} + \vec{K}_r = \vec{k'} + \vec{K'}_r \tag{2.19}$$

Which means that coupling Hamiltonian H_c couples the upper state $|\varepsilon\,\vec{k}\rangle_{+}$ to lower state $|\varepsilon\,\vec{k}\rangle_{-}$

Finally for $\vec{k_i} = \vec{k} + \vec{K_r} = \vec{k'}(mod\ \vec{K'_r})$ we derive formula for coupling matrix after some calculations (Appendix B) we switch to the following expression of the Hamiltonian: Where $\vec{K_r}$ and $\vec{K'_r}$ are vectors of reciprocal lattices.

$$t_i(\vec{k}+\vec{K_r}) = \frac{4\pi^2}{S}\,\widetilde{H}_c(\vec{k}+\vec{K_r})\,e^{i\,(\vec{k}+\vec{K_r})\cdot(\eta'\vec{u'}-\eta\vec{u}+\vec{\Delta})} \tag{2.20}$$

Where S is area of unit cell, $\vec{\Delta}$ is translation between the two layers,$\eta = 1$ reads for B-atom and $\eta = 0$ for A-atom. However this translation of the two layers just translate the overall Moire pattern and can be set to zero without loss of generality.

By symmetry of interaction between two orbitals, coupling depends only on the modulus of $\vec{k}+\vec{K_r}$ i.e $\widetilde{H}_c(\vec{k}+\vec{K_r}) \approx \widetilde{H}_c(|\vec{K_d}+\vec{K_r}|)$. The modulus of t_i is represented in Fig (2.9).

From Fig (2.9) one sees that the most important value of $|t_i|$ is one corresponding to the smallest possible value of $\vec{k}+\vec{K_r}$. By careful examination it can be shown that for electronic states close to the Dirac point this minimum corresponds to the modulus of wave-vector in Dirac point ($|\vec{K_d}| \approx 1.72$Å). From figure(coupling) it is easy to see coupling value close Dirac is around 0.12eV (Appendix B). All the other contributions are much smaller and will be neglected here.

Selecting only this contribution means that $\vec{K_r}$ is such that $\vec{k}+\vec{K_r}$ belongs to one of three equivalent valleys. Therefore a set of two Bloch states with a given wave vector (Equations 2.7 and 2.8) in one plane will be coupled to three sets of of two Bloch states in other plane corresponding to three different wave vectors. This simplifies much the structure of Hamiltonian and the analytical calculations presented here.

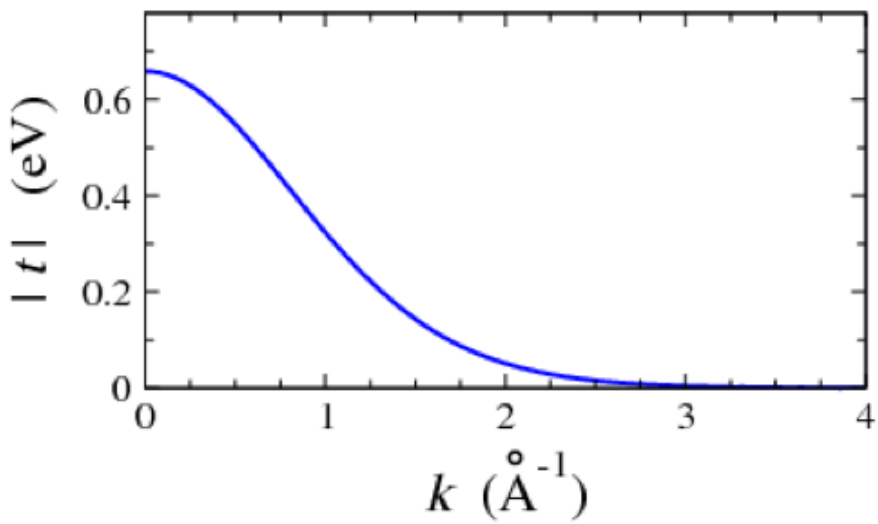

Figure 2.9: Modulus of the inter-layer coupling in versus modulus of the wave-vector

2.5 Velocity renormalization and electron life time

We are interested in the self-energy of coupling of states in upper plane due to the coupling with states of lower plane. Indeed the real-part of self-energy $\Re\sigma(z)$ is associated to modification of dispersion relation and will allow us to discuss velocity renormalization. The imaginary part of self-energy is associated to the electron lifetime. It will allow us to discuss lifetime of the electron in one plane when there is disorder in other plane.

Using matrix notations defined in Appendix B we have:

$$\widetilde{\Sigma}_0(z) = \sum_{\vec{K}_r} T_+(\vec{K}_r)\ \mathcal{G}_0^-\ (\vec{K}_d + \vec{K}_r)\ T_-(\vec{K}_r) \tag{2.21}$$

where $\vec{K}_r$ is the vector of reciprocal lattice which has three values as explanined above. T describes the coupling between two plane and Green operator at wave vector $\theta\,\vec{\zeta}\times\vec{K}_\mu$

is

$$\mathcal{G}_0^-(z, \theta\vec{\zeta}\times\vec{K}_\mu) = \frac{1}{z - H_-(\theta\vec{\zeta}\times\vec{K}_\mu)} \tag{2.22}$$

where $\vec{K}_\mu$ counts three Dirac points.

and for the Hamiltonian:

$$H_-(\theta\vec{\zeta}\times\vec{K}_\mu) = \begin{pmatrix} -\gamma_1\, g(\theta\vec{\zeta}\times\vec{K}_\mu) + \Delta & -\gamma_0 f\,(\theta\vec{\zeta}\times\vec{K}_\mu) \\ -\gamma_0 f^*\,(\theta\vec{\zeta}\times\vec{K}_\mu) & -\gamma_1\, g(\theta\vec{\zeta}\times\vec{K}_\mu) + \Delta \end{pmatrix} \tag{2.23}$$

Where Δ is potential difference between two layers (plane(+) is in potential 0 and plane(-) is in potential Δ), $g = (|f|^2 - 3)$ is effect of next-nearest neighbor hoping of one plane [54] $\gamma_1 \approx 0.1$eV and:

$$f\,(\theta\vec{\zeta}\times\vec{K}_\mu) = |f\,(\theta\vec{\zeta}\times\vec{K}_\mu)|\; e^{i(\theta_\mu + \frac{\pi}{2}\varepsilon_\theta)}\; e^{i\alpha_-(\theta)} \tag{2.24}$$

where: $\varepsilon_\theta = \mathrm{sgn}(\theta)$, $\alpha_-(\theta) = \frac{2\pi\theta}{\sqrt{3}}$, is the next-nearest neighbor hoping and

$$|f\,(\theta\vec{\zeta}\times\vec{K}_\mu)| = \left|\gamma_0 e^{i\frac{2\pi}{\sqrt{3}}\theta}\left(1 - e^{-i\frac{2\pi}{\sqrt{3}}\theta}\right)\right| = 2\sin\frac{\pi\theta}{\sqrt{3}} \tag{2.25}$$

Note that this matrix is evaluated at $\theta\vec{\zeta}\times\vec{K}_\mu$. Indeed for $\vec{k}$ sufficiently close to Dirac point $\vec{k}$, because $\hbar v(|\vec{k} - \vec{K}_d|) \ll \gamma_0|f\,(\theta\vec{\zeta}\times\vec{K}_\mu)|$ and we can neglect the dependence on the $\vec{k}$ in H_-, $\mathcal{G}_-$ and $\widetilde{\Sigma}(z)$

So now after complex calculations (Appendix B) we can write a perfect relation for self-energy:

$$\widetilde{\Sigma}_0(z) = \sigma(z)\,\mathbf{I} \tag{2.26}$$

with $\mathbf{I}$ is identity matrix and

$$\sigma(z) = \frac{6t^2}{\left[z - \gamma_1 g_(\theta)\right]^2 - \gamma_0^2 |f(\theta)|^2}\left[z - \Delta - \gamma_1 g_(\theta) - 2\gamma_0 \sin(\frac{\pi\theta}{\sqrt{3}})\sin(\frac{2\pi\theta}{\sqrt{3}})\right] \tag{2.27}$$

Let us recall that the perturbation theory is valid for

$$z, t, \Delta \ll \gamma_0 f(\theta) \tag{2.28}$$

As shown below the important quantities are $\sigma(z)$ and its derivative $\sigma'(z)$. For both quantities we can neglect z in denominator. For simplicity we also neglect $g(\theta)$ and assimilate $|f(\theta)|$ and keep linear relation of $\sin\theta = \theta$:

$$\sigma(z) \approx \frac{-6t^2}{\gamma_0^2 \frac{4\pi^2}{3}\theta^2}\left[z - \Delta - \gamma_0^2 \frac{4\pi^2}{3}\theta^2\right] \tag{2.29}$$

2.5.1 Velocity renormalization

Using equation (2.25) we have every thing in hand to calculate the Green's function term in states $\vec{k}$ of the upper plane

$$\mathcal{G}_0^+ = \frac{1}{z - H_+(\vec{k}) - \tilde{\Sigma}_0(z)} = \begin{pmatrix} z - \sigma(z) & -\hbar v|\vec{k}|e^{i\theta(\vec{k})} \\ -\hbar v|\vec{k}|e^{-i\theta(\vec{k})} & z - \sigma(z) \end{pmatrix}^{-1} \tag{2.30}$$

$$= \frac{1}{(z-\sigma(z))^2 - (\hbar v|\vec{k}|)^2} \begin{pmatrix} z-\sigma(z) & \hbar v|\vec{k}|e^{i\theta(\vec{k})} \\ \hbar v|\vec{k}|e^{-i\theta(\vec{k})} & z-\sigma(z) \end{pmatrix}$$

The eigenvalues are the poles of the Green's function. Therefore the energy $E(\vec{k})$ is given by

$$E - \sigma(E) = \pm\hbar v|\vec{k}| \tag{2.31}$$

For $|\vec{k}| = 0$ we have solution $E = E_0$ such that

$$E_0 - \sigma(E_0) = 0 \tag{2.32}$$

For small $\vec{k}$ we can write $E(\vec{k}) = E_0 + \delta E(\vec{k})$. Eventually we have a nice formula:

$$\delta E = \frac{\pm\hbar v|\vec{k}|}{1-\sigma'(E_0)} \tag{2.33}$$

Finally the renormalized velocity v_r is

$$\frac{v_r}{v} = \frac{1}{1+A/\theta^2} \tag{2.34}$$

where

$$A = \frac{6t^2}{4/3\,\pi^2\gamma_0^2} = \theta_0^2 \tag{2.35}$$

Where $\theta_0 = 1.4°$. Therefore using a well established tight-binding model, we recover velocity renormalization consistent with that of [59]. In addition we find that this velocity renormalization is independent of the difference in potential of two planes.

As it is shown in Figure 2.10 a systematic study of the renormalization of the velocity

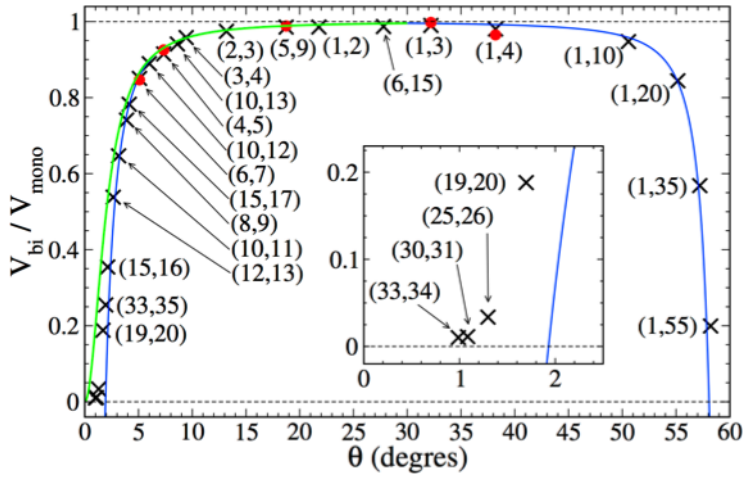

Figure 2.10: Velocity ratio $v_b i/v_{\text{mono}}$ for a commensurate (n, m) bilayer cell versus rotation angle θ: Red circles: VASP calculations by Laurence Magaud, cross: TB calculations by Guy Trambly de Laissardière, the blue line is the model of Lopez dos Santos et al.: $v_b i/v_{\text{mono}} = 1 - 9[\tilde{t}/(v_{\text{mono}}K\ \sin(\theta/2))]$, with $\tilde{t} = 0.11$eV and $v_{\text{mono}}K = 2\sqrt{3}\gamma_0\pi = 9.8$ eV . From [50]. And the green line is our model.

close to the Dirac point is done [50], compared to its value in a monolayer graphene, for rotation angles θ varying between 0° and 60° (Figure 2.10). The renormalization of the velocity varies symmetrically around $\theta = 30°$. Indeed, the two limit cases $\theta = 0°$ (AA stacking) and $\theta = 60°$ (AB stacking) are different, but Moiré patterns when $\theta \to 0°$ and when $\theta \to 60°$ are similar because a simple translation by a vector transforms an AA zone to an AB zone.

Focusing on angles smaller than 30°, it is defined [50] three regimes as a function of the rotation angle θ (Figure 2.10). For large $\theta(20° \leq \theta \leq 30°)$ the Fermi velocity is very close to that of graphene. For intermediate values of $\theta(3° \leq \theta \leq 20°)$ the perturbative theory of Lopez dos Santos et al. predicts correctly the velocity renormalization which is also in accordance to the above formula Equation(2.33). For the small rotation angles

($\theta < 3°$) a new regime occurs where the velocity tends to zero and perturbation theory can't be applied.

2.5.2 Electron lifetime

The two planes of the bilayer can have very different amount of disorder due to their different exposure to environment . For example the lower plane will be in contact with a substrate and the upper plane is exposed either to vacuum or to a gas (sensor application). Therefore it is of high interest to consider the limit case where defects are present in one plane and absent from the other plane. In the following we consider that defects are present only in the lower plane. If the two planes were decoupled, defects in one plane would affect electron lifetime in that plane but not in other one. Since the planes are coupled defects in one plane will also affect electronic lifetime in the other plane. In this chapter we discuss how such a repartition of defects impacts the electron lifetime. In chapter III based the present results we shall discuss how electron lifetime affects the overall electronic conduction of the bilayer.

If there is disorder in the lower plane the Bloch states of this plane will have a contribution to their self-energy which is imaginary. This can be represented in the simple possible model by a purey imaginary part of the potential evergy Δ

$$\Delta = -i\frac{\hbar}{\tau_-} \tag{2.36}$$

where τ_- is the lifetime in the lower plane due to disorder in the lower plane. Using formula 2.29 we see that electrons in the upper plane acquire an imaginary self-energy

$$\Im\sigma(z) = -\frac{i\hbar}{\tau_-} \times \frac{6t^2}{\gamma_0^2 4/3\pi^2\theta^2} = -\frac{i\hbar}{\tau_+} \tag{2.37}$$

Therefore the lifetimes τ_- and τ_+ in the lower and upper planes are related through:

$$\frac{\tau_+}{\tau_-} = \frac{\theta^2}{A} \tag{2.38}$$

where A is given by equation 2.34, and is same quantity as in the velocity renormalization expression 2.35.

2.6 Density of States

We consider now the Density of States (DOS) on one plane as a function of position $\vec{r}$ in the Moire structure. Here $\vec{r}$ will be position of the A and B atom.

$$\rho(E, \vec{r}) = \langle \vec{r}|\delta(E - H)|\vec{r'}\rangle \tag{2.39}$$

This quantity can be measured by STM and oscillations of the DOS are observed in experiments. To our knowledge a theory of this quantity didn't exist prior to this work and is presented now. According to the theory developed in Appendix B, the upper plane has an effective Hamiltonian which is modified by the coupling with lower plane. This effective Hamiltonian contains a self-energy discussed before which is independent of position and just renormalizes the velocity. It contains also a term that couples states with wave vector $\vec{k}$ and states with wave vector $\vec{k} + \vec{G}$ where $\vec{G}$ is a reciprocal vector of Moire pattern. It is this coupling which mixes those states and will give oscillation of DOS with vector $\vec{G}$.

Due to our approximation on the inter-plane hopping $|t_i|$ only the 6 $\vec{G}_j$ with $|\vec{G}_j| = |\sqrt{3}K_d\theta|$ occur. These six G_j are along 6 directions with angles $\theta_j = 2\pi/6\, j$. After a long calculation(Appendix B) we get a compact formula for variation of the DOS [53]

$$\Rightarrow \frac{\Delta\rho(E,\vec{R},\varepsilon)}{\rho(E)} \cong \frac{2t^2}{(\hbar c K_d\theta)^2}\sum_{j=1}^{6}\cos(\vec{G}_j\cdot\vec{R}) \tag{2.40}$$

as we see this formula doesn't depend to type of atom ε (A or B atom), it oscillates with $\vec{G}$ as expected. Using $t \approx 0.12$eV we have

$$\Rightarrow \frac{\Delta\rho(E,\vec{R})}{\rho(E)} \cong \frac{1}{\theta_{deg}^2}\sum_{j=1}^{6} cos(\vec{G}_j\cdot\vec{R}) \tag{2.41}$$

where θ_{deg} is the rotation angle expressed in degrees. As it is clear the maximum value is obtained for $\vec{R} = 0$ which is in the AA region and $\sum_{j=1}^{6} cos(\vec{G}_j\cdot\vec{R})$ is 6. For example for $\theta = 3^\circ$ the maximum value of relation variation of DOS is $\frac{6}{9}$ in the AA region which is strong. We note also that the relative variation rapidly decreases when θ increases.

We now compare our model results with those of tight-binding calculations. As shown in Fig 2.11 the overall agreement between tight-binding and model calculations is quite good. We observe in particular a reinforcement of the DOS in the AA region and a lowering in the AB regions. This behavior is a precursor of the electronic localization in AA region which is observed in the very low angle limit $\theta < 1 - 2^\circ$.

The main difference between the two approaches is the following. In the tight-binding results, two neighboring A and B atoms do not have the same DOS. In the analytical approach there is no such difference. As shown in Fig 2.12 average DOS of two neighboring A and B atoms is well reproduced by the analytical model. Yet the DOS on sub lattices A

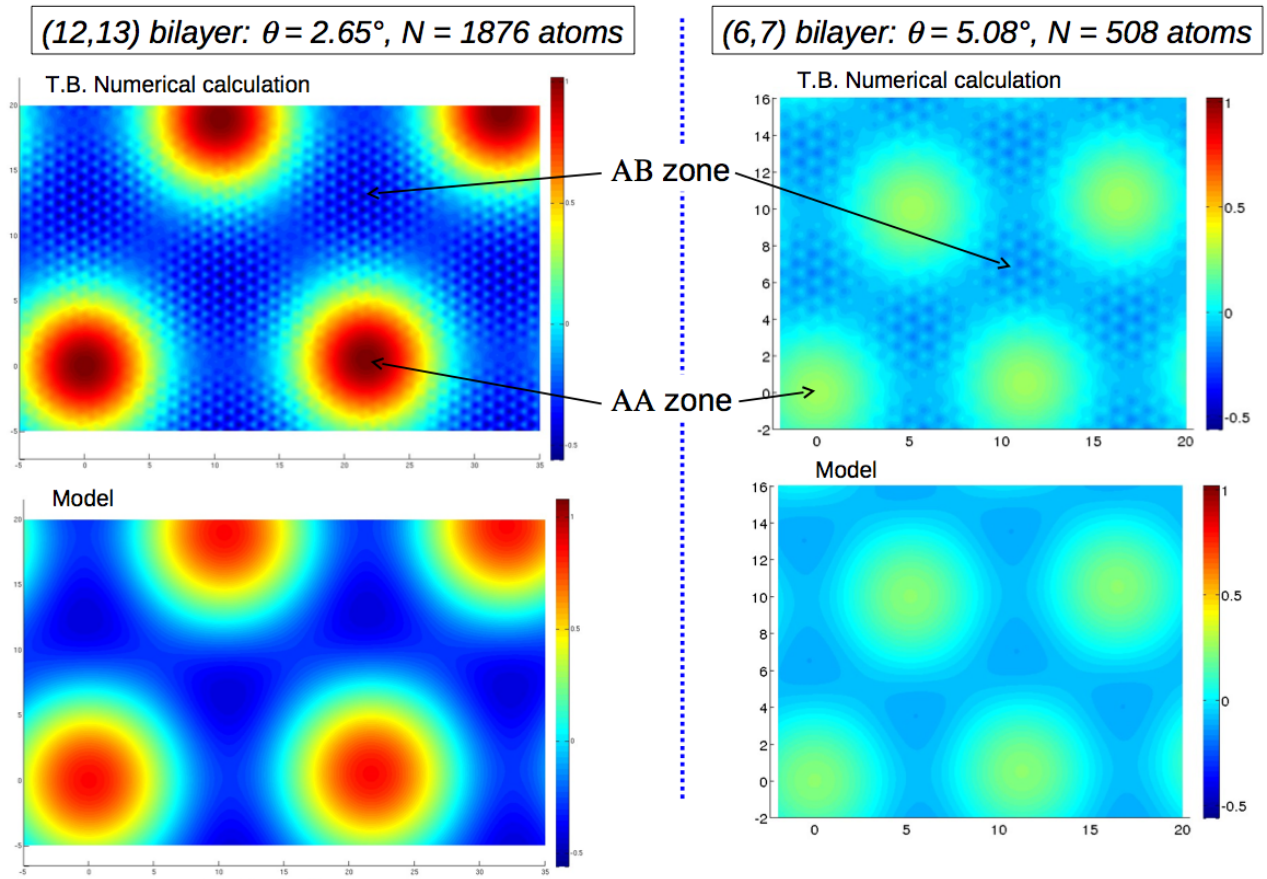

Figure 2.11: Relative variation of the LDOS on top layer for two angles. Tight-binding results are in the top and corresponding analytical results are below.

and B can differ by about ±15% as compared to averaged DOS. The reason of this discrepancy is not firmly established. It could be due to the use of perturbative theory. Another cause could be that we retained only one Fourier component of the transfer matrix element of $t(\vec{k})$. Indeed in the calculation by Castro Neto et. al [60] the authors retain also only one Fourier component of the transfer matrix $t(\vec{k})$, but do numerical non-perturbative calculation. They find also a DOS which is the same for neighboring A and B atoms.

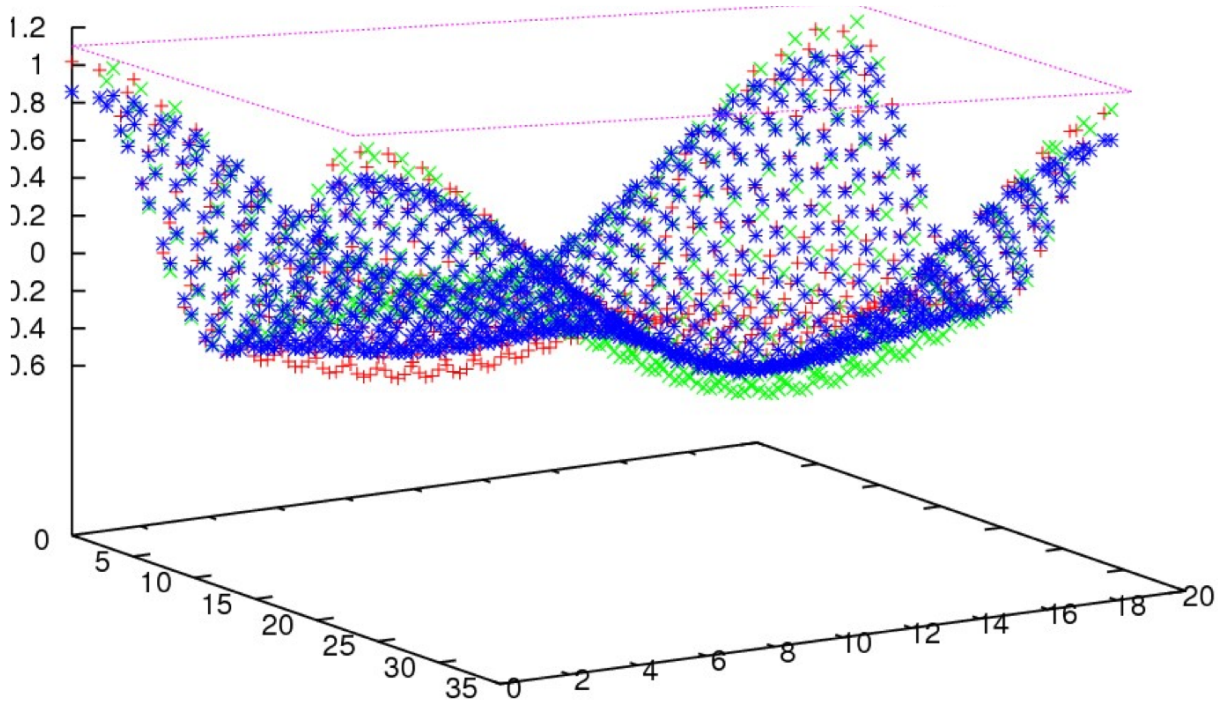

Figure 2.12: 3D relative variation of DOS $\frac{\Delta\rho(E,\vec{R})}{\rho(E)}$. The green and red points correspond to A and B atoms with a difference of about $\pm 15\%$. Blue points corresponds to our analytical model which reproduce the average values of relative variation of DOSs on A and B atoms.

Bibliography

[1] S. Latil, L. Henrard, Phys. Rev. Lett. **97**, 036803 (2006)

[2] F. Guinea, A.H. Castro Neto, N.M.R. Peres, Phys. Rev. B **73**, 245426 (2006)

[3] B. Partoens, F.M. Peeters, Phys. Rev. B **74**, 075404 (2006)

[4] B. Partoens, F.M. Peeters, Phys. Rev. B **75**, 193402 (2007)

[5] M. Koshino, T. Ando, Phys. Rev. B **76**, 085425 (2007)

[6] M. Koshino, T. Ando, Phys. Rev. B **77**, 115313 (2008)

[7] H. Min, A.H. MacDonald, Phys. Rev. B **77**, 155416 (2008)

[8] H. Min, A.H. MacDonald, Prog. Theor. Phys. Suppl. 176, 227 (2008)

[9] M. Aoki, H. Amawashi, Solid State Commun. **142**, 123 (2007)

[10] F. Zhang, B. Sahu, H. Min, A.H. MacDonald, Phys. Rev. B **82**, 035409 (2010)

[11] K.F. Mak, J. Shan, T.F. Heinz, Phys. Rev. Lett. **104**, 176404 (2010)

[12] C.L. Lu, C.P. Chang, Y.C. Huang, R.B. Chen, M.L. Lin, Phys. Rev. B **73**, 144427 (2006)

[13] C.-L. Lu, H.-C. Lin, C.-C. Hwang, J. Wang, M.-F. Lin, C.-P. Chang, Appl. Phys. Lett. **89**, 221910 (2006)

[14] M. Koshino, T. Ando, Solid State Commun. **149**, 1123 (2009)

[15] H. Min, A.H. MacDonald, Phys. Rev. Lett. **103**, 067402 (2009)

[16] J. Nilsson, A.H. Neto, F. Guinea, N.M. Peres, Phys. Rev. Lett. **97**, 266801 (2006)

[17] J. Nilsson, A.H. Castro Neto, Phys. Rev. Lett. **98**, 126801 (2007)

[18] J. Nilsson, A.H. Castro Neto, F. Guinea, N.M.R. Peres, Phys. Rev. B **78**, 045405 (2008)

[19] H. Min, P. Jain, S. Adam, M.D. Stiles, Phys. Rev. B **83**, 195117 (2011)

[20] K.S. Novoselov, E. McCann, S.V. Morozov, I.V. Falko, M.I. Katsnelson, U. Zeitler, D. Jiang, F. Schedin, A.K. Geim, Nature Phys. **2** 177 (2006)

[21] E. McCann, V.I. Falko, Phys. Rev. Lett. **96**, 086805 (2006)

[22] S.B. Trickey, F. Mller-Plathe, G.H.F. Diercksen, J.C. Boettger, Phys. Rev. B **45**, 4460 (1992)

[23] R. Saito, M.S. Dresselhaus, G. Dresselhaus *Physical Properties of Carbon Nanotubes*, (Imperial College Press, London, 1998)

[24] Amidror, Isaac.: *The Theory of the Moiré Phenomenon*; Volume I: Periodic Layers; 2nd ed., 2009; Springer

[25] S. Latil and L. Henrard, Phys. Rev. Lett. *97*, 036803 (2006).

[26] F.Zhang, B.Sahu, H.Min, A.H.MacDonald, Phys. Rev. B *82*, 035409 (2010)

[27] F. Varchon, P. Mallet, J.-Y. Veuillen, and L. Magaud, Phys. Rev. B *77*, 235412 (2008).

[28] T.Ohta, A.Bostwick, T.Seyller, K.Horn, E.Rotenberg Science *313*, 951 (2006)

[29] C.Coletti, C.Riedl, D.S.Lee, B.Krauss, L.Patthey, K.von Klitzing, J.H. Smet, U.Starke, Phys. Rev. *81*, 235401 (2010)

[30] I. Brihuega et al., Phys. Rev. Lett. *101*, 206802 (2008).

[31] J.Hass et al Appl. Phys. Lett *89*, 143106 (2006)

[32] J.Hass et al J.Phys: Condens. Matter *20*,323202(2008)

[33] K.V.Emtsev, F.Speck, Th. Seyller, L.Ley, J.D.Riley, Phys. Rev B *77*, 1553023 (2008)

[34] J. Hass, F. Varchon, J. E. Millan-Otoya, M. Sprinkle, N. Sharma, W. A. de Heer, C.Berger, P. N. First, L. Magaud, H. Conrad, Phys. Rev. Lett. *100*, 125504 (2008).

[35] M.Sprinkle et al Phys. Rev. Lett. *103*, 226803 (2009)

[36] J.Hicks et al Phys. Rev. B *83*, 205403 (2011)

[37] A.Luican, G.Li, A.Reina, J.Kong, R.R.Nair, K.S.Novoselov, A.K.Geim, E.Y.Andrei, Phys. Rev. Lett. *106*, 126802

[38] G.Li, A.Luican, L.M.B.Lopes dos Santos, A.H.Castro Neto, A.Reina, J.Kong, E.Y.Andrei, Nat. Phys. *6*, 109,(2010)

[39] D.L.Miller et al, Science *324*, 924 (2009)

[40] C. Berger et al., Science *312*, 1191 (2006).

[41] M.L.Sadowski, G.Martinez, M.Potemski, C.Berger, W.A.de Heer, Phys. Rev. Lett. *97*, 266405

[42] F.Varchon, P.Mallet, L.Magaud, J.-Y.Veuillen, Phys. Rev. B *77*, 165415 (2008) (2006)

[43] J. M. B. Lopez dos Santos, N. M. R. Peres, and A. H. Castro Neto, Phys. Rev. Lett. *99*, 256802 (2007) (2006)

[44] S.Latil, V.Meunier, L.Henrard, Phys. Rev. B *76*, 201402(R) (2008)

[45] S. Shallcross, S. Sharma, and O. A. Pankratov, Phys Rev.Lett. *101*, 056803 (2008)

[46] G.Mele

[47] E.Suarez Morell, J.D.Correa, P.Vargas, M.Pacheco, Z.Barticevic, Phys. Rev. B *82*, 121407 (R) (2010).

[48] R.Bistritzer and A.H. MacDonald, Proc. Natl. Acad. Sci. USA 108, 12233 (2011)

[49] R.Bistritzer and A.H.MacDonald, Phys. Rev. B *81*, 245412 (2010)

[50] G. Trambly de Laissardiere, D. Mayou, L. Magaud, Nano Let. 10, 804(2010)

[51] G.Trambly de Laissardiere

[52] J. M. Campanera, G. Savini, I. Suarez-Martinez, and M. I. Heggie Phys. Rev. B **75**, 235449 (2007).

[53] O. Faizy, G. Trambly de Laissardiere, D. Mayou.: to be submitted

[54] K. Sasaki, S. Murakami, and R. Saito; : Appl. Phys. Lett. 88, 113110 (2006)

[55] Yen-Hung Ho, Jhao-Ying Wu, Rong-Bin Chen, Yu-Huang Chiu, and Ming-Fa Lin Appl. Phys. Lett. **97**, 101905 (2010)

[56] Hongki Min.: *Graphene Nanoelectronics: Metrology, Synthesis, Properties and Applications*, NanoScience and Technology. Springer, 2012, p. 325

[57] Edward McCann.: *Graphene Nanoelectronics: Metrology, Synthesis, Properties and Applications*, NanoScience and Technology. Springer, 2012, p. 237

[58] I. Lobato and B. Partoens, PHYSICAL REVIEW B **83**, 165429 (2011)

[59] J. M. B. Lopes dos Santos, N. M. R. Peres, and A. H. Castro Neto, Phys Rev Lett, **99**, 256802 (2007)

[60] J. M. B. Lopes dos Santos, N. M. R. Peres, A. H. Castro Neto.: arXiv:1202.1088v1 [cond-mat.mtrl-sci]

CHAPTER III

QuantumTransport in Graphene Nanostructures

Abstract

In this chapter we consider the transport properties of the two graphene based structures analyzed in this thesis : rotated bilayers and impurity on graphene. We give first an introduction to the theory of electronic transport in bulk systems and in particular to the Kubo formalism. We discuss the role of quantum diffusion and disorder on conductivity. Then we present numerical simulations of quantum diffusion and conductivity in rotated bilayers in the case where disorder is in one plane only. The results of chapter 2 on electron lifetime allows us to propose a simple model that rationalizes these numerical results and explains the role of interlayer coupling on the conductivity of rotated bilayers. We consider then the case of transport through nanocircuits with coherent electronic transport. We introduce the fundamentals concepts of the Landauer approach and the way of calculating conductance from Greens function. This allows us then to analyze a model of transport through a STM tip that is positionned just above an impurity on graphene. As we show, when this impurity presents a resonant state, an anomalous behavior of the STM

signal can exist in the near field regime. The STM signal dI/dV no more represents the Density of States and can present a dip instead of a resonance as a function of the energy.

3.1 Introduction to Bulk Transport

In macroscopic conductors, the resistance that is found to exist between two contacts is related to the bulk conductivity and to the dimensions of the conductor. In short, this relationship is expressed by

$$R = \frac{L}{\sigma A}, \tag{3.1}$$

where σ is the conductivity and L and A are the length and cross-sectional area of the conductor, respectively. If the conductor is a two-dimensional conductor, such as a thin sheet of metal, then the conductivity is the conductance per square, and the cross-sectional area is just the width W. This changes the basic formula (3.1) only slightly, but the argument can be extended to any number of dimensions. Thus, for a d-dimensional conductor, the cross-sectional area has the dimension $A = L^{(d-1)}$, where here L must be interpreted as a characteristic length. Then, one may rewrites (3.1) as

$$R = \frac{L^{(2-d)}}{\sigma_d}, \tag{3.2}$$

Here, σ_d is the d-dimensional conductivity. In general, for 2D and 3D systems, the current density may not be parallel to the direction of the field. The resistivity would then be represented by a tensor, i.e., an $N \times N$ matrix with $N = 1, 2, 3$ according to the dimensionality.

In addition the electric field component E_ν and current $\mathbf{j}(\mathbf{r}, t)$ may depend on space and time. For a small, arbitrary electric field, the electrical response may also be *non-local* in space (for an inhomogeneous system) : the current density at point $\mathbf{r}$ and time t may depend on the conductivity at every other point in space and earlier times. The general current response is thus

$$j_\mu(\mathbf{r}, t) = \sum_\nu \int d\mathbf{r}' \int_{-\infty}^{t} dt' \, \sigma_{\mu\nu}(\mathbf{r}, \mathbf{r}'; t - t') E_\nu(\mathbf{r}', t'), \tag{3.3}$$

We present basic approaches of the conductivity for homogenous fields.

In this case, if a field component $E_\nu(\mathbf{r})$ is applied in the ν direction and induces a current density j_μ in the μ direction, the linear response relation 3.3 becomes

$$j_\mu = \sum_\nu \sigma_{\mu\nu} E_\nu \ , \tag{3.4}$$

with $\sigma_{\mu\nu}$ the elements of the conductivity *tensor*. All the above quantities can be frequency dependent. One shall consider especially the component σ_{xx} for an isotropic model one has $\mathbf{j}(\omega) = \sigma(\omega)\mathbf{E}(\omega)$ with $\sigma_{xx}(\omega)$

3.1.1 Drude Model

Let us assume classical electrons of mass m and electric charge e. They move under the action of the electric field and will experience collisions that will change their momentum $\mathbf{p}$. These collisions could be due to the scattering with ionic vibrations, or collisions with

other electrons or impurities. For the time being the nature of the collisions is irrelevant. However, what is important for the considerations one makes here is that all collisions are independent events, namely, electrons experience a collision independently of the outcome of previous collisions(one says that a collision at time t is *uncorrelated* with a collision at time t).

Electrons have an average velocity $\mathbf{v}$. Let us now define the *relaxation time* τ as the average time between two successive collisions. As a consequence of these collisions, in the time interval τ , electrons change, on average, their momentum by the amount

$$\frac{d\mathbf{p}}{dt} = -\frac{m\mathbf{v}}{\tau} \ , \tag{3.5}$$

where m is the effective mass of the electron in the given material.

By assuming that after a collision the electron emerges with a velocity $\mathbf{v}_0$ that is randomly oriented. This implies that on average (over all particles) the randomly oriented velocity immediately. After the collision does not contribute to the total average velocity $\mathbf{v}$, i.e., $\langle \mathbf{v}_0 \rangle = 0$. After the collision, and before the next collision occurs, the electron is accelerated by the driving field. Between collisions, the change of momentum must then be proportional to the field

$$\frac{d\mathbf{p}}{dt} = e\mathbf{E} \ , \tag{3.6}$$

At steady state, if all the momentum change is equal to the one the electrons experience during collisions 3.5 one can then have the relation:

$$\frac{m\mathbf{v}}{\tau} = e\mathbf{E} \ , \tag{3.7}$$

Comparing 3.7 with $\boldsymbol{E} = \rho \boldsymbol{j}$, and using the form well-known equation $\mathbf{j}(\mathbf{r}, t) = e\, n(\mathbf{r}, t)\, \mathbf{v}(\mathbf{r}, t)$ for the current density, the resistivity is

$$\rho = \frac{m}{ne^2\tau} \ . \tag{3.8}$$

In this model, the conductivity is given by

$$\sigma = \frac{1}{\rho} = \frac{ne^2\tau}{m} \tag{3.9}$$

This is the Drude relation between the conductivity and the microscopic properties of the conducting electrons. At non-zero frequency it generalizes to

$$\sigma(\omega) = \frac{ne^2\tau/m}{1 - i\omega\tau} \tag{3.10}$$

The relaxation time is generally the only unknown and can be determined experimentally precisely from the relation 3.9, once the conductivity is measured. Relaxation times in bulk metallic wires are typically of the order of 10^{-14}s at room temperature and reflect mainly inelastic scattering of electrons by ionic vibrations.

3.1.2 Resistance, coherent and incoherent transport

The above analysis tells us the real physical origin of resistance: Momentum change. One can thus gives the following physical definition:

Resistance : *Amount of momentum change during collisions*.

In this context, momentum change is also referred to as momentum *relaxation*. The collisions can then be ideally grouped into:

- **Elastic** : Momentum relaxes but single-particle energy is conserved.
- **Inelastic** : Momentum and energy relax.

Relaxation times can be accordingly defined. For instance, an *elastic relaxation time* is the time between two successive collisions that change electron momentum, but conserve single-particle energy. This is the case, for instance, for scattering off a rigid impurity.

Following the distinction between elastic and inelastic resistance, it is also customary to name the electron dynamics in which the system experiences only elastic scattering, *phase coherent transport*, from the fact that if the single-particle energy is conserved, the phase of the corresponding timedependent wave-function has a simple oscillatory behavior, with constant frequency, over the whole time evolution. In other words, no phase is lost or gained during the collision.This is clearly an idealization, as scattering processes that change single-particle energy are always present to some degree. Electron transport is thus truly *incoherent*. It then can be defined an *energy* or *inelastic relaxation time*

$$\tau_E = \textit{average time between two successive scattering events that change energy.} \quad (3.11)$$

In certain literature it is also customary to define as *dephasing processes* those that change the phase without, however, changing the energy considerably. This is assumed to be the case, for instance, for *voltage probes*: devices that measure a voltage difference, without

carrying overall current.

In this case a coherence time is

$$\tau_\phi = \textit{average time between two successive scattering events that change wave-function phase.} \tag{3.12}$$

If this time is longer than the time it takes for electrons to go from one side of the sample to the other then electron transport may, to some degree, be approximated as coherent. As we will discuss in the next chapter this is one of the underlying assumptions of the Landauer approach.

3.1.3 Introduction to Kubo formalism

The Drude model is a purely classical model. Although it is robust and has a wide range of applicability in the metals and semi-conductors, it is not satisfying since it is not based on quantum mechanics. A way to take part to take partly into account quantum aspects is through Bloch-Boltzman theory. In *bulk* materials and devices, transport has been well described via the Boltzmann transport equation or similar kinetic equation approaches [1] The validity of this approach is based on the following set of assumptions: (i) scattering processes are local and occur at a single point in space; (ii) the scattering is instantaneous (local) in time; (iii) the scattering is very weak and the fields are low, such that these two quantities form separate perturbations on the equilibrium system; (iv) the time scale is such that only events that are slow compared to the mean free time between collisions are of interest. In short, one is dealing with structures in which the potentials vary slowly on both the spatial scale of the electron thermal wavelength (to be defined

below) and the temporal scale of the scattering processes.

Yet the Boltzman approach does not take into account interferences effects after several scattering events. These effects can ultimately lead to Anderson localization and are of primary importance especially in $1D$ or $2D$. The Bloch-Boltzman approach can not treat two strong scattering. For these reasons we will use Kubo formalism which is the best adapted to the problem treated here.

3.1.4 Conductivity and dissipation

We consider a system at equilibrium which is perturbed by an external voltage . In the framework of linear response theory, this voltage induces an electric field $\mathbf{E}$ and a current density $\mathbf{j}$ which is proportional to it, namely $j = \sigma\mathbf{E}$. To calculate the conductivity σ, one can introduce a perturbation term associated to the electric field in the Hamiltonian which becomes

$$\mathcal{H} = \frac{p^2}{2m} + V(\mathbf{r}) + e\mathbf{E}\cdot\mathbf{r} \ , \tag{3.13}$$

However, for a macroscopic conductor, the additional term of this Hamiltonian cannot be considered as a perturbation, even though the electric field is small. It is more convenient to use the equivalent Hamiltonian

$$\mathcal{H} = \frac{(p - e\mathbf{A}(t))^2}{2m} + V(\mathbf{r}) \ , \tag{3.14}$$

where the electric field results from the time-dependent vector potential $\mathbf{A}(t)$ as

$$\mathbf{E} = \frac{\partial \mathbf{A}}{\partial t} \quad \text{and} \quad \nabla \times \mathbf{A} = 0 \ , \tag{3.15}$$

The current density is given by $\mathbf{j} = \mathrm{Tr}\,(\rho \hat{\mathbf{j}})$ where $\hat{\mathbf{j}}$ is the current density operator and $\rho(t)$ is the one-particle density matrix which obeys

$$i\hbar \frac{\partial \rho}{\partial t} = [\mathcal{H}, \rho] \ . \tag{3.16}$$

One can writes ρ in the form $\rho = \rho_0 + \delta\rho$, where ρ_0 is the equilibrium density matrix that corresponds to $\mathbf{A} = 0$. A stationary electric field is suitably described by a monochromatic field of frequency ω, $\mathbf{E}(\omega) = i\omega\mathbf{A}(\omega)$, in the limit $\omega \to 0$. For a macroscopic system, 3.16 leads to an infinitely long transient regime without relaxation towards a stationary regime. One way to cure this problem is to introduce a term of the form $-i\gamma\delta\rho(t)$ into Equation 3.16, leading to an exponential relaxation on the time scale $\hbar/\gamma$ .One finally takes the limit $\gamma \to 0$, assuming that the end result does not depend on γ .

Another way to interpret the relaxation rate γ is to consider a finite size conductor coupled to the external environment (the reservoirs) constituted by the measurement leads. Electrons can penetrate into the reservoirs, change their phase randomly, and be reinjected incoherently into the sample. A weak coupling between the conductor and the reservoirs can be modelled with a broadening γ of the energy levels of the isolated sample, so that $\hbar/\gamma$ represents the lifetime of an electron in the conductor. Instead of 3.16, it obtains [3]

$$i\hbar \frac{\partial \rho}{\partial t} = [\mathcal{H}, \rho] - i\gamma\Big(\rho(t) - \rho_{eq}(t)\Big) \ , \tag{3.17}$$

where the density matrix ρ_{eq} describes the total system at thermal equilibrium. We may

conclude from this description that an intrinsic irreversible behavior appears as a result of the coupling to reservoirs. But one should keeps in mind that the whole system, namely conductor together with reservoirs, remains quantum mechanically coherent, and it is the averaging over the degrees of freedom of the reservoirs that introduces irreversibility.

Within the linear response approximation, one retains only the linear terms in $\mathbf{A}(t)$ in the expression of $\delta\rho(t)$, of $\delta\rho_{eq}(t) = \rho_{eq} - \rho_0$, and of the Hamiltonian (3.16). Rewriting $\mathcal{H} = \mathcal{H}_0 + \mathcal{H}_1(t)$ where $\mathcal{H}_0 = \frac{p^2}{2m} + V(\mathbf{r})$ and

$$\mathcal{H}_1(t) = \frac{e}{2m}(\mathbf{p}\cdot\mathbf{A} + \mathbf{A}\cdot\mathbf{p}) \ , \tag{3.18}$$

and after some calculations [3] for an electric field applied along Ox axis, so that the conductivity is

$$\sigma_{xx}(\omega) = \frac{i}{\omega}\Big[\frac{ne^2}{m} + \frac{e^2}{m^2\Omega}\sum_{\alpha\beta}\frac{f(\varepsilon_\alpha) - f(\varepsilon_\beta)}{\varepsilon_\alpha - \varepsilon_\beta}\frac{\varepsilon_\alpha - \varepsilon_\beta - i\gamma}{\varepsilon_\alpha - \varepsilon_\beta - \hbar\omega - i\gamma}|\langle\alpha|p_x|\beta\rangle|^2\Big] \ , \tag{3.19}$$

where $f(\varepsilon_\alpha)$ is the occupation factor of the state $|\alpha\rangle$ and Ω is the volume of the conductor. In order to simplify this expression, one can uses the so-called *f-sum rule* which states that

$$n + \frac{1}{m\Omega}\sum_{\alpha\beta}\frac{f(\varepsilon_\alpha) - f(\varepsilon_\beta)}{\varepsilon_\alpha - \varepsilon_\beta}|\langle\alpha|p_x|\beta\rangle|^2 = 0 \tag{3.20}$$

Introducing the matrix element of the current operator $j_{\alpha\beta} = \frac{e}{m}\langle\alpha|p_x|\beta\rangle$ and restoring the spin s, finally

$$\sigma_{xx}(\omega) = is\frac{\hbar}{\omega}\sum_{\alpha\beta}\frac{f(\varepsilon_\alpha) - f(\varepsilon_\beta)}{\varepsilon_\alpha - \varepsilon_\beta}\frac{|j_{\alpha\beta}|^2}{\varepsilon_\alpha - \varepsilon_\beta - \hbar\omega - i\gamma}\ , \tag{3.21}$$

Consider only the case of zero frequency. The matrix elements $j_{\alpha,\beta}$ of the operator p_x can be related to matrix elements of the position operator X. This allows to write the DC conductivity in terms of quantum diffusion which is the Einstein formula.

3.1.5 Conductivity and quantum diffusion

In the framework of Kubo-Greenwood approach [13] for calculation of the conductivity, a central quantity is the average quadratic spreading of wave packets of energy E at time t along the x direction,

$$\Delta X^2(E,t) = \left\langle \left(\hat{X}(t) - \hat{X}(0)\right)^2 \right\rangle_E , \tag{3.22}$$

where $\hat{X}(t)$ it the Heisenberg representation of the position operator $\hat{X}$. The $\langle\hat{A}\rangle_E$ means an average of diagonal elements of the operator $\hat{A}$ over all states with energy E. The diffusivity at zero temperature, $\mathcal{D}(E)$, at energy E is deduced from ΔX^2,

$$\mathcal{D}(E) = \lim_{t\to+\infty} D(E,t) \quad \text{with} \quad D(E,t) = \frac{\Delta X^2(E,t)}{t}, \tag{3.23}$$

where $D(E,t)$ is called diffusion coefficient.

In a 2-dimensionnal system with surface S, the DC-conductivity σ_{xx} at zero temperature along the x-direction is given by the Einstein formula:

$$\sigma_{xx}(E_\mathrm{F}) = \frac{e^2}{S} n(E_\mathrm{F})\mathcal{D}(E_\mathrm{F}), \tag{3.24}$$

where $n(E)$ is the total density of states and E_{F} the Fermi energy.

The effect of decoherence mechanisms such as electron-electron scattering, electron phonon interaction (temperature), is not considered in the above expression. This effect can be estimated by introducing an inelastic scattering time τ_i.

Therefore the experimental conductivity can be estimated by:

$$\sigma_{xx}(E_{\mathrm{F}}) = \frac{e^2}{S} n(E_{\mathrm{F}}) \mathcal{D}(E_{\mathrm{F}}, \tau_i), \tag{3.25}$$

τ_i decreases when the temperature increases. In actual graphene at room temperature, realistic values of τ_i is a few 10^{-13}s. Here the Fermi-Dirac distribution function is taken equal to its zero temperature value. This is valid provided that the electronic properties vary smoothly on the thermal energy scale $k_{\mathrm{B}}T$.

3.2 Transport in rotated bilayer

3.2.1 Introduction

We consider now the conduction of rotated bilayers in the case where disorder is only in the lower plan while the upper plane contains no defects. We believe that this situation can occur because the two planes are not exposed to the environment in a symmetric manner. For example the lower plane can be in contact with a substrate when the upper plane is exposed to a gas which can produce adsorbates.

The model studied here could also be of interest for bi-wall or multi-wall nanotubes. Indeed the external wall of the nanotube can be modified by adsorbed chemical species

while the inner walls are protected. In that case also the overall conductance of the nanotube should depend on the coupling between the different layers. This coupling itself will depend on the chiralities of the walls.

3.2.2 Monolayer of Graphene

Let us recall first a few results about the conductivity of a grapheme monolayer in the presence of a short-range scattering potential. If disorder is not too strong the density of states is not affected and a simple model is given by the Einstein formula:

$$\sigma = e^2 \nu(E_F) D \tag{3.26}$$

where

$$\nu(E_F) = 2_s 2_v |E_F|/(2\pi\hbar^2 v_F^2) \tag{3.27}$$

is the density of states at the Fermi energy (only electrons close to the Fermi energy are involved in transport), and:

$$D = v_F^2 \tau/2 \tag{3.28}$$

is the diffusion constant in two dimensions. The classical contribution to the conductivity is therefore in terms of the Fermi-wavevector k_F and the mean free path $l = v_f \tau$.

$$\sigma = \frac{2_s 2_v e^2}{2h} k_F l, \tag{3.29}$$

Note that the fact that the DOS is not modified implies that $k_F l \gg 1$ and therefore $\sigma \gg \frac{2e^2}{h} G_0$. Yet there are quantum corrections to this formula due to Anderson localization effects. The variation of conductivity due to this correction is:

$$\Delta\sigma(L) = -[2_s 2_v e^2/(\pi h)] \ln(L/l) \tag{3.30}$$

Where L is the cutt-off length due to the loss of phase coherence. The localization length ξ can be estimated with the condition $\sigma + \Delta\sigma(L = \xi) = 0$ as

$$\xi/l \sim \exp(\frac{\pi k_F l}{2}) \tag{3.31}$$

Close to the Dirac point numerical simulation show that the DOS is strongly modified and presents a plateau. In this regime $k_F l \sim 1$, the conductance takes a value which is of order of G_0 and ξ/l is smaller.

As explained in 3.1.2 the inelastic scattering tends to destroy localization on length scale greater than the inelastic mean-free path. In the following we present results of the transport which can be interpreted by neglecting all localization effects. This means the inelastic mean-free path is of the order of a few elastic mean-free path.

3.2.3 Main results

The model studied numerically is that of a rotated bilayer treated in a tight-binding Hamiltonian. The defects in the lower plane are vacancies on sites that are distributed

at random. These vacancies represent in a simple manner adatoms such as Hydrogen on graphene (see chapter 4). Although we must be careful in our interpretation of the data, since our results are preliminary, we believe that the behavior analyzed here is representative more generally of disorder with short-range potential.

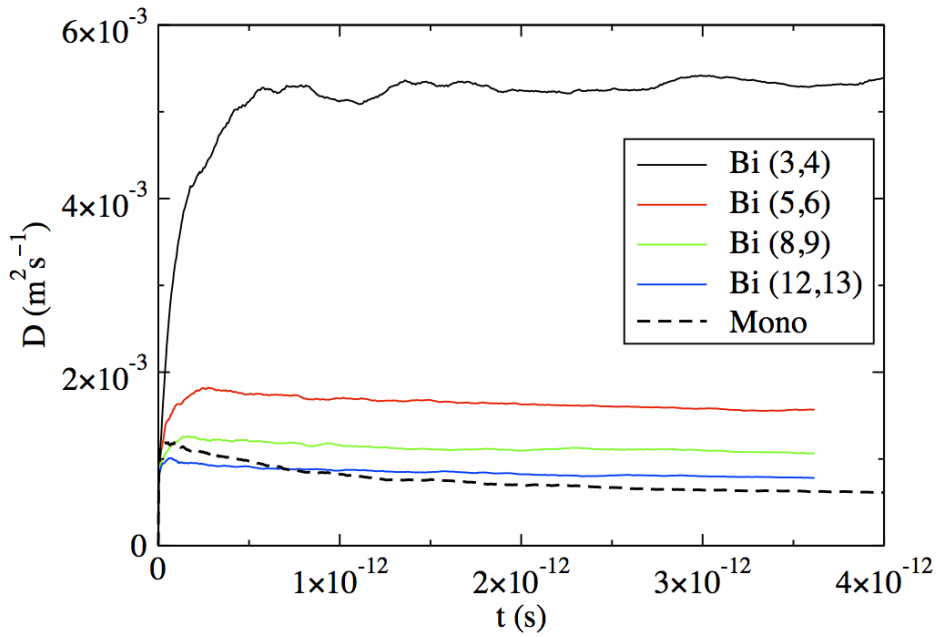

Figure 3.1: Diffusivity $D = X^2(E,t)/t$ versus time t for $E = 0.1$eV. The angles corresponding to the different bilayers are $\theta(3,4) = 9.54°$, $\theta(6,7) = 5.09°$, $\theta(8,9) = 3.89°$, $\theta(12,13) = 2.65°$

Here we will show some preliminary results for only one concentration of 1% of sites which is a relatively high concentration for this type of adsorbate. The numerical calculation provides us with the density of states as a function of the energy and the quantum diffusion $X^2(E,t)$ as a function of energy E and time t.

Figure 3.1 shows the typical behavior of the diffusivity $D(E,t) = X^2(E,t)/t$ for different bilayers at energy $E = 0.1$ eV. $D(E,t)$ first increases at short times this is the ballistic

regime. Then the diffusivity reaches a maximum which is the microscopic diffusivity. It is this value that is described typically by a semi-classical model and that will be discussed in detail hereafter. For larger times the diffusivity decreases more or less rapidly due to quantum interferences effects which ultimately lead to the Anderson localization. Indeed for short range uncorrelated disorder in a $2D$ system we expect that ultimately all states are localized at large distances as discussed above.The localization length ξ is usually very large so that the microscopic diffusivity and conductivity are representative of the measured conductivity except for large samples (several microns) and temperatures well below the room temperature.

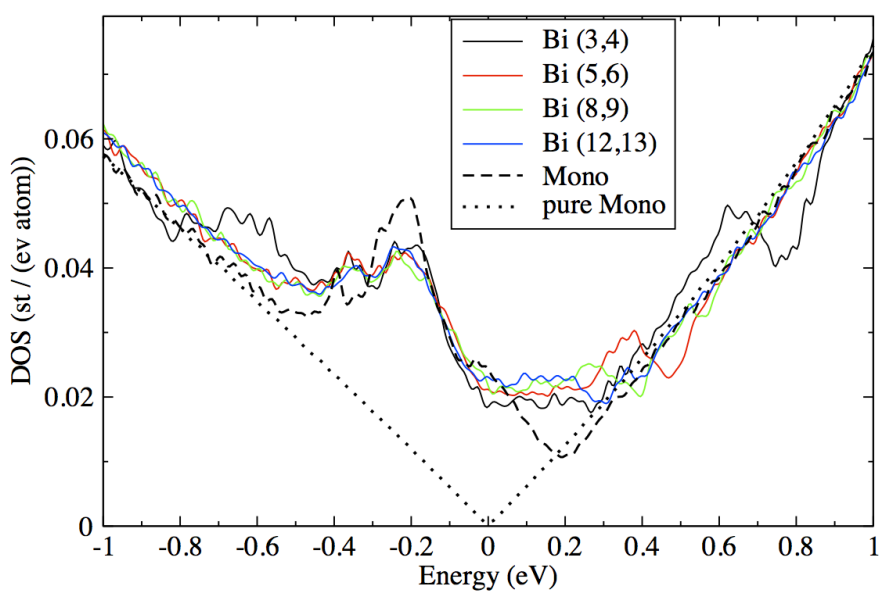

Figure 3.2: DOS in the bilayer and in the monolayer with pure or defect (1% vacancy) in the one layer. The angles corresponding to the different bilayers are $\theta(3,4) = 9.54°$, $\theta(6,7) = 5.09°$, $\theta(8,9) = 3.89°$, $\theta(12,13) = 2.65°$.

Figure 3.2 shows the total density of states as a function of energy for several angles. We report also the density of states for a monolayer without defects and for a monolayer

with a concentration of defects equal to that of the lower plane of the bilayer (i.e. 1%). Except for the pure monolayer there is a plateau of density of states around the zero energy (Dirac energy). This is a well known phenomenon that is in agreement with calculations of defected structures in the literature. The peak in the DOS around the energy $E = -0.2$ eV is a reminiscence of the resonance called midgap state. Due to the second nearest neighbor hopping taken into account in the present tight-binding model this midgap state is displaced and does not occur the Dirac energy $E = 0$. It is also enlarged.

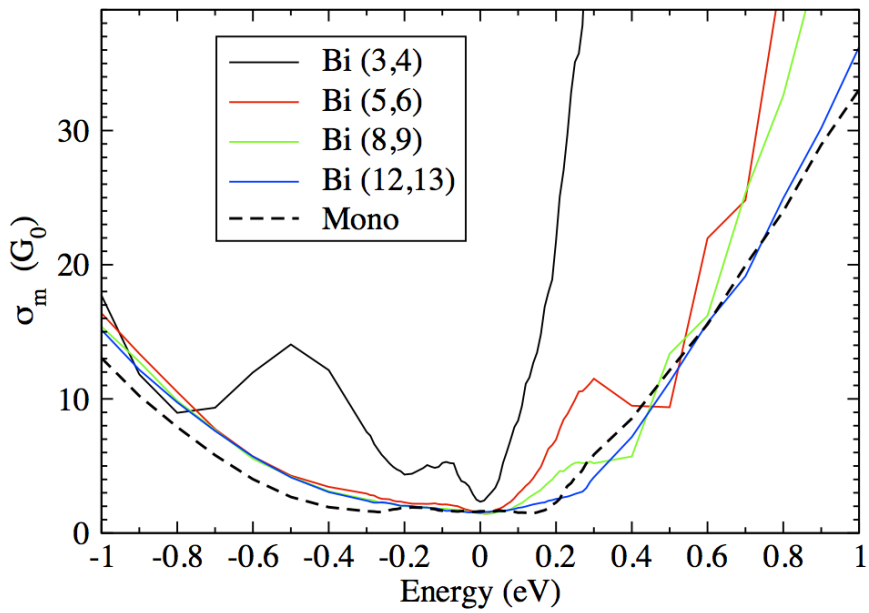

Figure 3.3: Conductivity in the bilayer and in the monolayer with pure or defect (1% vacancy) in the one layer. The angles corresponding to the different bilayers are $\theta(3,4) = 9.54°$, $\theta(6,7) = 5.09°$, $\theta(8,9) = 3.89°$, $\theta(12,13) = 2.65°$

Figure 3.3 shows the microscopic conductivity of the rotated bilayer as well as that of the monolayer with 1% defects. Here also there is a minimum of the conductivity of the order of $G_0 = 2e^2/h$ close to the Dirac energy. This corresponds to the well known

minimum conductivity of graphene. For the monolayer this minimum occurs in an energy window of about 0.6 eV. For the bilayers this energy window corresponding to the minimum conductivity tends to decrease when the angle increases. Away from this minimum the general trend is that the conductivity of the bilayer, at a given energy, increases when the rotation angle increases.

3.2.4 Model and discussion

We develop now a simple model of conductivity of the bilayer that can explain the main trends and gives some quantitative predictions. In the absence of coupling between the two planes the conductivity of the bilayer is simply the sum of the conductivities of both planes. Here we assume that in the presence of coupling the conductivity of the bilayer is still the sum of the conductivities:

$$\sigma \approx \sigma_+ + \sigma_- \tag{3.32}$$

In order to compute the conductivity of each plane we consider that the relaxation of the current is identical to the lifetime of electrons. This assumption is valid for isotropic scattering which is the case here. Due to the small coupling the electron transport lifetime, the density of states and the velocity in the lower plane (the one containing defects) are weakly changed except perhaps for the lowest angles ($\theta < \theta_0$) that are not amenable to a perturbative treatment of the interlayer coupling. Therefore we shall consider that the conductivity of this plane is unaffected by the coupling with the other plane.

For the upper plane the situation is quite different. As explained in chapter 2 the coupling with the lower plane that contains defects induces a finite lifetime τ_+ for electrons

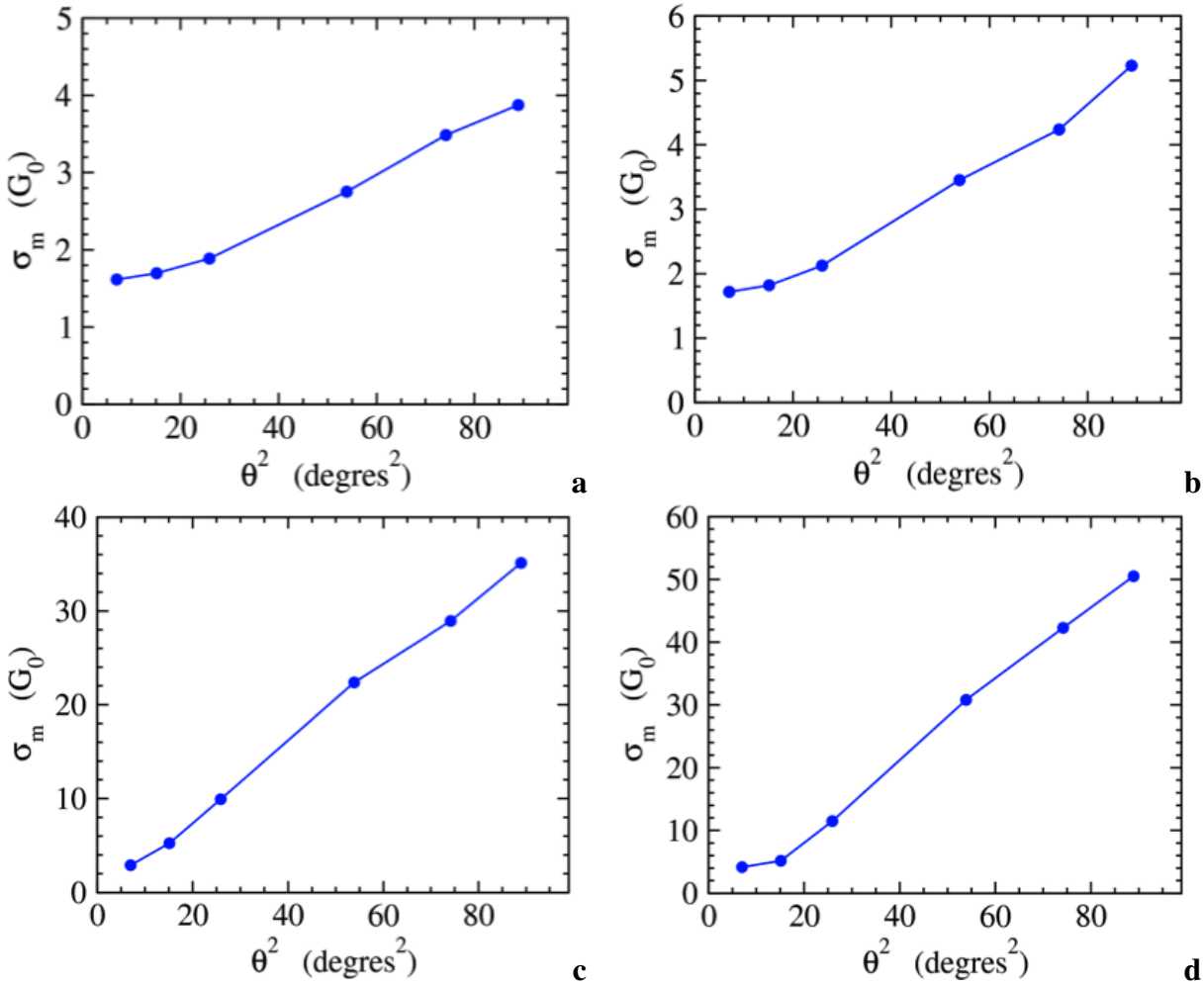

Figure 3.4: Conductivity in rotated bilayer versus the squared angle in degree for different energies: (a) E= -0.05 eV, (b)E=-0.1 eV, (c) E=0.25 eV and (d) E= 0.3 eV

in this plane. Therefore the conductivity is no more infinite as it is in the absence of coupling. We shall consider that the velocity is unchanged and that the density of states is not too much affected by the coupling with the lower plane except very close to the Dirac energy on an energy scale of order h/τ_+. In this energy range σ_+ is of the order of $\sigma_{\min} \sim G_0 = \dfrac{2e^2}{h}$.

According to the Einstein formula the two conductivities are :

$$\sigma_- = e^2 n_-(E) v^2 \tau_- \text{ and } \sigma_- = e^2 n_+(E) v^2 \tau_+ \tag{3.33}$$

This simple model explains why at a given energy the conductivity increases with the angle between the two layers. This is due to the fact that the scattering time τ_+ in the upper plane increases with the angle simply because the coupling with the disordered lower plane decreases.

In the energy range corresponding to Figure 3.4 the conductivity of the monolayer with defects is roughly constant, therefore we take

$$\sigma_- \approx \sigma_{\text{mono}} \approx \sigma_{\min} \tag{3.34}$$

where $\sigma_{\min}$ is of order of $G_0 = \frac{2e^2}{h}$. We can write:

$$\frac{\sigma_+}{\sigma_-} = \frac{n_+(E)}{n_-(E)} \frac{\tau_+}{\tau_-} \tag{3.35}$$

$$\sigma_+ \approx \sigma_{\min} \frac{n_+(E)}{n_-(E)} \frac{\tau_+}{\tau_-} \tag{3.36}$$

$$\frac{\tau_+}{\tau_-} \approx \frac{\theta^2}{\theta_0^2} \tag{3.37}$$

Where $\theta_0 = 1.4°$ is given in chapter2. The results shown in Figure 3.4 for different energies are compatible with a scattering time that increases linearly with the square of the angle as given by the above formula.

The factor given by the ratio of the two densities of states 3.36 is not necessarily equal to one. Indeed close to the Dirac energy the density of states in the plane with defects (lower plane) can be in a plateau due to the relatively strong disorder. In the upper plane the effective scattering time is larger and the effective disorder is smaller. Therefore at the same energy the density of states of the upper plane can be that of pure graphene which is smaller. From this model we expect that the total variation of the conductivity between low angles (about 2-3 degrees) and large angles about (10 degrees) will depend on the ratio between the two densities. This is what is shown by Figure 3.4. This is in rough agreement with ratio of DOS of the monolayer with and without defects (Figure 3.2)

3.3 Landauer approach

Here we present an approach due to Landauer [8; 10; 9], which relates the conductance G to the transmission properties of the disordered conductor, viewed as a quantum potential barrier. For a finite length one-dimensional wire connected to perfect conductors, the Landauer formula,

$$G = 2\frac{e^2}{h}T \ , \tag{3.38}$$

relates the conductance to the transmission coefficient T through the wire. The conductance we consider here is that of the entire system composed of the barrier itself and the two ideal leads. This relation holds for each realization of disorder and not only on average.

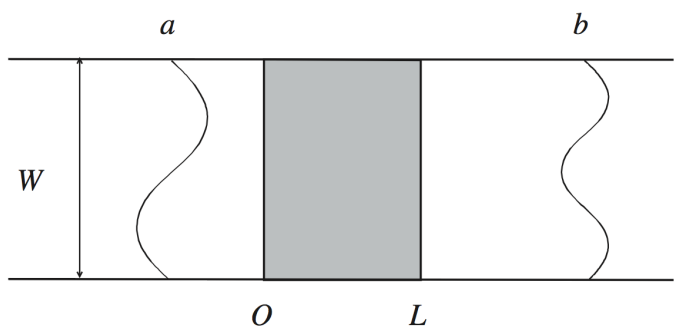

Figure 3.5: Wave guide geometry used in the Landauer formalism. The disordered conductor of length L and section $S = W^{d-1}$ is perfectly connected to ideal leads defined as wave guides propagating incoming, reflected and transmitted plane waves.

This Landauer formula 3.38 can be generalized to higher dimensionalities d. To that purpose, we consider a disordered conductor of length L and square section $S = W^{d-1}$, connected to ideal leads (Figure 3.5) viewed as wave guides propagating transmitted and reflected plane waves. In this geometry, the transverse wave vector of the eigenmodes of the wave guide (also called *transverse channels*) are quantized by boundary conditions. We can thus define the transmission coefficient T_{ab} between an incoming channel a and an outgoing channel b. The Landauer formula (3.29) generalizes to

$$G = 2\frac{e^2}{h}\sum_{a,b} T_{a,b} \ , \tag{3.39}$$

To determine the number of transverse channels, we consider that electrons are injected at the Fermi energy. For Schrödinger electrons the square of their wave vector is $k_F^2 = k^2 + |\mathbf{q}|^2$ where k and $\mathbf{q}$ are the longitudinal and transverse components. The transverse modes are quantized in units of $2\pi/W$. In three dimensions, the number of transverse channels is

$$M = \frac{\pi k_F^2}{4\pi^2/W^2} = \frac{k_F^2 S}{4\pi} \ , \tag{3.40}$$

and in $d = 2$, the number of transverse channels is:

$$M = \frac{2k_F}{2\pi/W} = \frac{k_F W}{\pi} \ . \tag{3.41}$$

The Landauer approach is well adapted to the description of electronic transport and it provides an alternative and equivalent approach to the Kubo formula. It becomes essential if we wish to describe transport in conductors with a complex geometry or in optics where there is no equivalent to the Kubo description. Moreover, in optics, it is possible to measure the contribution T_{ab} of each transmission channel. The Landauer approach allows us to retrieve all the results already obtained within the Kubo formalism, such as the weak localization correction [3] to the conductance.

The Landauer formalism for wave guide geometry has been generalized by M. Büttiker to account for more complex geometries called multi-terminal geometries with several contacts [12].

3.3.1 Green's Function and Fisher-Lee Formula

The Green's functions and relations with scattering matrix are present in Appendix C. We want to present the Fisher-Lee formula which expresses the elements of the $\mathcal{S}$-matrix in terms of the Green's function [9].

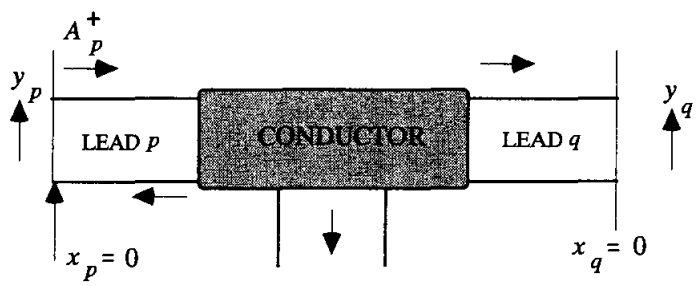

Figure 3.6: A unit impulse in lead p generates an incident wave which is partially transmitted to each of other leads. Taken from [9]

Consider a conductor connected to a set of leads. For convenience, we use a different coordinate system in each lead as shown in Figure 3.6. The interface between lead p and the conductor is defined by $x_p = 0$. We will use the symbol $\mathcal{G}^R_{qp}$ to denote the Green's function between a point lying on the plane $x_p = 0$ and another point lying on $x_q = 0$

$$\mathcal{G}^R_{qp}(y_q; y_p) \equiv \mathcal{G}^R(x_q = 0,\, y_q;\, x_p = 0,\, y_p)\ , \tag{3.42}$$

Let us try to write this quantity in terms of the $\mathcal{S}$-matrix element connecting the two leads. This is easy to do if we neglect the transverse dimension (y) of the leads and treat

them as one-dimensional. We know that the unit excitation at $x_p = 0$ gives rise to a wave of amplitude A_p^- away from the conductor (not shown in the Figure 3.6) and a wave of amplitude A_p^+ toward the conductor. The wave traveling toward the conductor is scattered by the conductor into different leads. Hence we can write

$$\mathcal{S} = -\delta_{qp} + i\hbar\sqrt{v_q v_p}\mathcal{G}^R_{qp}, \tag{3.43}$$

This is desired relation expressing the $\mathcal{S}$-matrix in terms of the Green's function.

For *Multi-Moded Leads* the Transmission function is given by [9]

$$\bar{T}_{pq} = \mathrm{Tr}[\Gamma_p \mathcal{G}^R \Gamma_q \mathcal{G}^A] \ , \tag{3.44}$$

in which

$$\Gamma_p = i[\Sigma_p^R - \Sigma_p^A] \tag{3.45}$$

where the advanced self-energy (Σ_p^A) is the Hermitian conjugate of the retarded self-energy (Σ_p^R).

The above formula for T_{pq} gives the transmission in terms of the green's function of the conductor and of the self-energy due to the coupling to the ballistic leads. Yet in some cases leads are not defined a priori as in the model studied in part 3.5. Then it is fruitfull to adopt another viewpoint through the notion of the effective channels [14]. As explained in this paper the effective channels can always be constructed starting from the central part of the device, figure 3.7. One shows that the transmission coefficient between the incoming channel1 and outgoing channel2 is given by:

$$\bar{T} = \mathrm{Tr}[\tilde{\Gamma}_1 \mathcal{G}^R \tilde{\Gamma}_2 \mathcal{G}^A] \ , \tag{3.46}$$

This formula is similar to the standard Fisher-Lee Formula 3.44, except that $\tilde{\Gamma}$ replaces Γ. This is so because the effective channels are not ballistic leads. More precisely they are ballistic far from the central part of the device but are not ballistic close to device. If there is just one mode per channel (as in the model studied in part 3.5) then $\tilde{\Gamma}$ and Γ are scalar quantities. It that case one has $\tilde{\Gamma} = \Gamma$. This is a surprising result since the transmission is somehow independent of the non-ballistic character of the channel close to the central part of the device. This result was not given in [14] and we derive it just below.

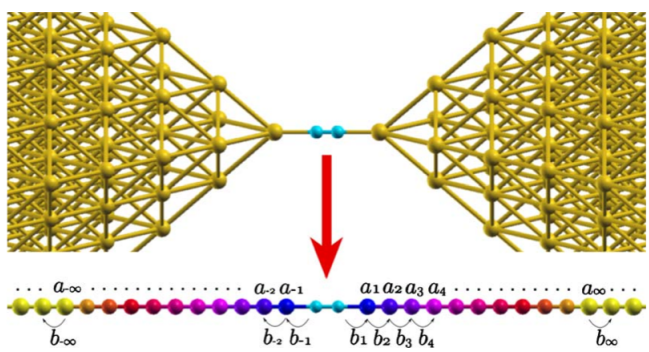

Figure 3.7: Mapping of a real $3D$ device (top: hydrogen molecule in between gold leads) into the effective $1D$ system (bottom: effective atomic chain). The *effective channels* arise from the central device (here the hydrogen molecule) and pursue into a nonballistic section (blue, violet, and red pseudoatoms), until they achieve an asymptotic ballistic behaviour (yellow). Taken from [14]

From [14] we have for $\tilde{\Gamma}$ of the right effective channel :

$$\tilde{\Gamma} = b_1^2 |\overline{g}_1|^2 \, b_2^2 |\overline{g}_2|^2 \, \cdots b_n^2 |\overline{g}_n|^2 \, \Gamma_n \tag{3.47}$$

where b_p is the hopping integral between sites p and $p-1$ and a_p is the on-site energy of site-p (see figure 3.7). The green's function is:

$$\overline{g}_p = \frac{1}{z - a_p - \Sigma_p(z)} \tag{3.48}$$

and

$$\Gamma_n = -2\Im\Sigma_n \tag{3.49}$$

Σ_p is the self-energy of site-p due to its coupling to all sites of its right side. Σ_p is given by:

$$\Sigma_p = b_{p+1}^2 \overline{g}_{p+1}(z) \tag{3.50}$$

Using equation 3.48 and 3.50 one obtains easily:

$$\Im\Sigma_{p-1} = b_p^2 |\overline{g}_p|^2 \Im\Sigma_p \tag{3.51}$$

By iterating equation 3.51 one obtains:

$$\Im\Sigma(z) = b_1^2 |\overline{g}_1|^2 \, b_1^2 |\overline{g}_1|^2 \, \cdots b_n^2 |\overline{g}_n|^2 \Im\Sigma_n \tag{3.52}$$

Where $\Sigma(z)$ is the self-energy of the central device (here the Hydrogen molecule) due to its coupling with the right effective channel. Since

$$\Gamma(z) = -2\Im\Sigma(z) \tag{3.53}$$

From 3.47, 3.49, 3.53 and 3.52 one has finally

$$\tilde{\Gamma}(z) = \Gamma(z) \tag{3.54}$$

3.4 Anomalous STM images of resonant states on Graphene

The Scanning Tunneling Microscope (STM) is of major importance in the investigation of surfaces properties. Usually the STM is used in the far distance mode and the signal dI/dV in proportional to the DOS below the STM tip, in accordance with the Tersoff-Hamann theory. If the STM approaches from the surface then one reaches the near field regime , where the electronic transmission at a given energy is expected to approach unity [15] as shown in Figure 3.8

In this section we analyze theoretically the STM images of a resonant state of an adsorbate on graphene. We consider the case where the STM tip comes close to the adsorbate of the surface of graphene. We show that in some cases the transmission can be small even if in this near-field regime instead of approaching unity as in standard models [15]. In this near-field regime the perturbative theory of the STM signal is not valid and we show that the STM image does not represent the local density of states. Instead we find that the resonance of the transmission $T(E)$ as a function of the energy of states E, which is characteristic of a resonant state, can be replaced by a dip as a function of the energy (anti-resonance). We analyze in particular two models. One is representative of an adsorbate in a top position i.e. the adsorbate is right above one carbon. The other model is representative of an adsorbate in a hollow position. In that case the adsorbate is right above the center of an hexagon of carbon atoms. We also compare our results with the

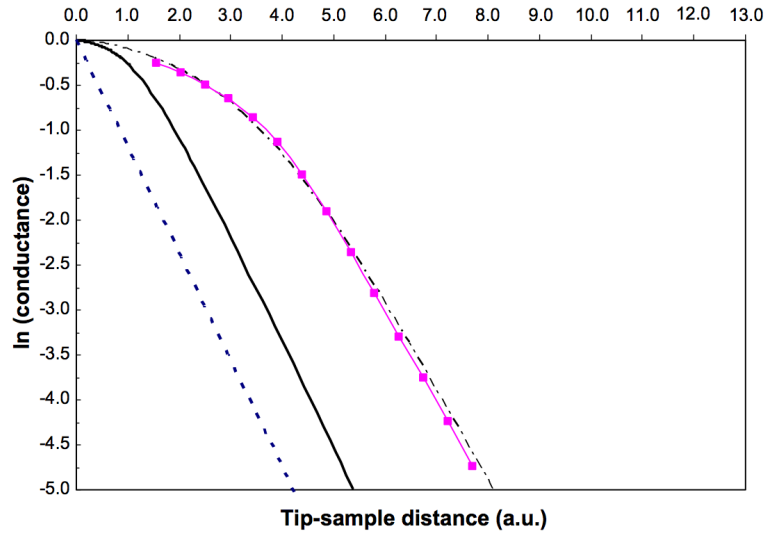

Figure 3.8: Logarithm of the conductance G in units of $\frac{2e^2}{h}$ as a function of distance for different models [15]. $G = \frac{2e^2}{h}T$ where T is the transmission. At large distances the transmission decreases exponentially with distance between the tip and the surface. At short distance the transmission is close to 1. Picture is taken from [15]

case of the adsorbate on a metallic substrate. As we show due to a large DOS of the metal the resonance created by the adsorbate is not sufficiently narrow to lead to an anomalous STM regime in the near field regime.

3.4.1 Model

We consider a one channel model according to the Fisher-Lee relation 3.44. The central part of the circuit is the apex atom of the STM tip (last atom of the STM tip at the right in Figure 3.9). The left lead is constituted by the rest of the tip coupled to leads of the STM aparatus. The right lead is constituted by the adatom and the substrate.

We note Σ_{STM} the self-energy of the apex orbital (there is one orbital/atom) due to coupling with left-lead (STM side). We note Σ_{ad} the self-energy due to the coupling with

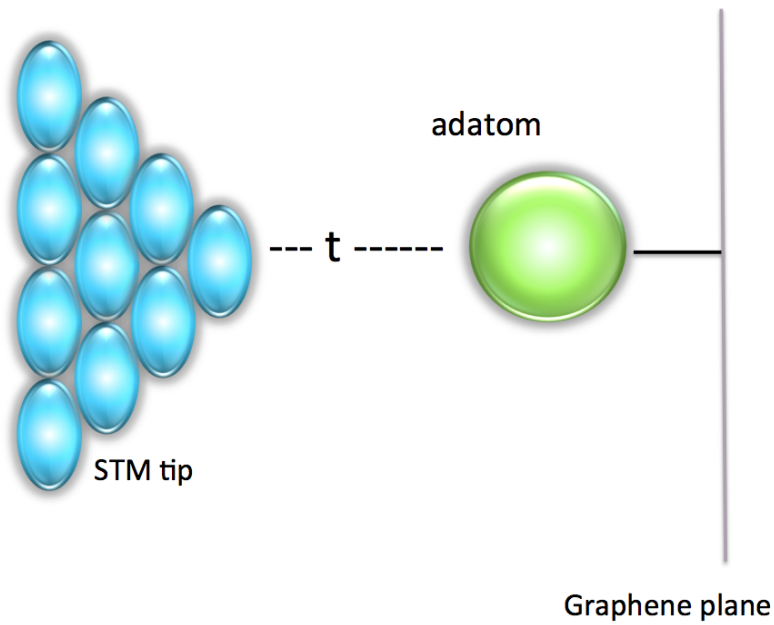

Figure 3.9: our schematic model of STM tip approaching on adatom.

the right-lead (adatom and substrate side). We take

$$\Sigma_{\mathrm{STM}} = -i\Delta \tag{3.55}$$

$$\Sigma_{\mathrm{ad}} = u - iv = t^2 g_{\mathrm{ad}} \tag{3.56}$$

where

$$g_{\mathrm{ad}} = \frac{1}{z - \epsilon_d - V^2 \tilde{g}} \tag{3.57}$$

Here Δ is width of the resonance of the DOS on the apex orbital of the STM tip alone.

t is the coupling between the apex orbital and the adatom. g_{ad} is the green's function of the adatom orbital coupled to the substrate and without the STM tip.

ϵ_d is the on-site energy of the adatom orbital, V is the coupling between the orbital of the adatom and the substrate. $\tilde{g}$ is the green's function of the states of the substrate which are coupled to the adsorbate orbital. Finally we introduce the quantity

$$x = \frac{t^2}{\Delta} \tag{3.58}$$

In this work we shall take $\Delta \sim 1\mathrm{eV}$ and $0 < t < 1\mathrm{eV}$. So that $0 \leqslant x \leqslant 1$ eV By writing of 3.44 for single channel we have for the transmission $T(E)$

$$T = \Gamma_{\mathrm{STM}}\, \mathcal{G}^R\, \Gamma_{ad}\, \mathcal{G}^A \tag{3.59}$$

Here

$$\Gamma_{\mathrm{STM}} = -2\Im(\Sigma_{STM}) \tag{3.60}$$

and

$$\Gamma_{ad} = -2\Im(\Sigma_{ad}) \tag{3.61}$$

where $\Im(z)$ is the imaginary part of complex number z. The green's functions $\mathcal{G}^R$ and $\mathcal{G}^A$ are given by

$$\mathcal{G}^R = \mathcal{G}^{*A} = \frac{1}{z - \Sigma_{STM} - \Sigma_{ad}} \tag{3.62}$$

Here we assume that the onsite energy for the apex orbital is equal to zero. In the

following we consider that the energy range of Fermi-Energy $z = E_F$ is small compared with the width of resonance Δ. Then $z \ll \Delta$ and we can simplify Equation 3.59 as

$$T = 2\Delta 2v \frac{1}{|u - i(\Delta + v)|^2} = \frac{4v}{\Delta} \frac{1}{|xg_{ad} - i|^2} \tag{3.63}$$

3.4.2 General trends

Large distance regime ($x|g_{ad}| \ll 1$ i.e $|u - iv| \ll \Delta$)

Let us consider the case when the STM tip is at a large distance of the adatom. Then the hopping integral t between the apex orbital and the adatom goes to zero and $u, v \ll \Delta \equiv x|g_{ad}| \ll 1$. Then equation 3.63 can be simplified to

$$T = \frac{4v}{\Delta} = 4\pi x N_{ad}(E) \tag{3.64}$$

which is equivalent to the standard Tersoff-Hamann theory. Note that πN_{ad} is the imaginary part of g_{ad} therefore $|\pi N_{ad}| < |g_{ad}|$, so that

$$T \leqslant 4x|g_{ad}| \ll 1 \tag{3.65}$$

Short distance regime with resonance ($x|g_{ad}| \gg 1$ i.e $|u - iv| \gg \Delta$)

Now we consider a case in which the tip approaches very close to the adatom. The above condition ($x|g_{ad}| \gg 1$) is possible typically if the resonance of the DOS on the adsorbate has a width Δ_r which is sufficiently small. Indeed for energies close to the resonance we have $|g_{ad}| \sim 1/\Delta_r$ and the condition $x|g_{ad}| \gg 1$ can be satisfied if $x \gg \Delta_r$. In the following we shall take $\Delta \sim$ 1eV and $0 < t <$ 1eV, so that $x <$ 1eV. The regime

$x|g_{ad}| \gg 1$ exists provided that $\Delta_r \ll 1$eV. This requires indeed a narrow resonance.

In this case, Equation 3.63 reduces to the following:

$$T \approx 2\Delta 2v \frac{1}{|u - iv|^2} \approx 2\Delta 2\Im\Big(\frac{1}{u - iv}\Big) \tag{3.66}$$

now by Equation 3.56

$$T = 2\Delta 2\Im\Big(\frac{1}{t^2 g_{\text{adatom}}}\Big) = 4\Delta \frac{V^2}{t^2}\Im(-\tilde{g}) \tag{3.67}$$

where $V^2\tilde{g} = \widetilde{\Sigma}$ so here $\widetilde{\Sigma}$ is the self-energy of the orbital of the adsorbate due to its coupling to the substrate. And therefore we have:

$$\Im(-\tilde{g}) = \pi\tilde{N}(E) \tag{3.68}$$

where $\tilde{N}$ is the effective Density of states coupled to the adatom. Thus finally we have

$$T(E) = 4\pi\Delta \frac{\gamma_0^2}{t^2}\tilde{N}(E) \tag{3.69}$$

Note that $\pi V^2\tilde{N}(E)$ is the imaginary part of $(z - \epsilon_d - V^2\tilde{g})$. Therefore $\pi V^2\tilde{N}(E) \leqslant |z - \epsilon_d - \gamma_0^2\tilde{g}| = \dfrac{1}{|g_{ad}|}$, and the transmission is small instead of being close to 1 as in standard models.

$$T(E) \leqslant \frac{4}{x|g_{ad}|} \ll 1 \tag{3.70}$$

Equation 3.69 means that the transmission in the near field regime depends only on the substrate (DOS of substrate). In the case of graphene the effective DOS $\tilde{N}(E)$ presents a dip close to zero energy. Therefore the we expect that the STM signal can present a dip

instead of a resonance. This is confirmed by the model calculation as shown below.

The interpretation of formula 3.69 is that in this near-field regime the *adatom is more coupled to the STM tip than to the substrate. Therefore the adatom can be considered as the apex atom of the STM tip while its coupling to the substrate is weak.* The equation 3.69 is equivalent to the standard Tersoff-Hamann' theory. It explains why the transmission is proportional to the effective density of states coupled to the adatom, in this regime $x|g_{ad}| \gg 1$

3.4.3 Numerical studies and discussion

Now we consider three models. The first two concern an adsorbate on graphene either in a top position or in a hollow position on graphene (see figure 3.10). The third model which we consider is the case of an adsorbate on a metallic substrate.

Let us describe now the main numerical results

1) **Adatom in top position**

In that case the self-energy is given by [16]:

$$\widetilde{\Sigma}_{\text{top}}(z) = -z\left[\left(\frac{V}{D}\right)^2 \ln\left|1 - \frac{D^2}{z^2}\right|\right] - i\pi\left(\frac{V}{D}\right)^2 |z|\,\Theta\Big(D - |z|\Big) \tag{3.71}$$

where $D = \sqrt{\sqrt{3}\pi t_0} \sim 6\text{eV}$ is a high-energy cutoff of order of the graphene bandwidth using the Debye prescription, i.e., conservation of the number of states in the Brillouin zone after linearization of the spectrum around the K point, $t_0 \sim 2.8\text{eV}$ is the hoping energy between nearest neighbors sites of graphene and $V = 5.2\text{eV}$ is the hybridization

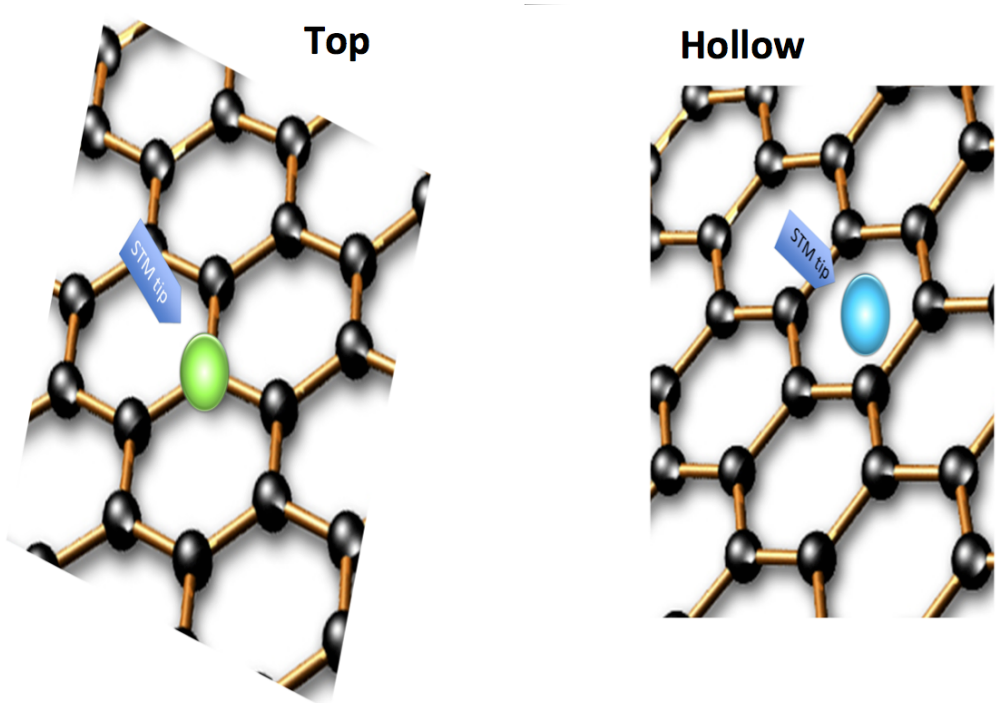

Figure 3.10: Two different models of adsorbate on graphene. One is representative of an adsorbate in a top position where the adsorbate is right above one carbon (Fig left). The other model is representative of an adsorbate in a hollow position (Fig right). In that case the adsorbate is right above the center of an hexagon of carbon atoms.

amplitude of the adatom (Hydrogen here) with the nearest carbon atom. We will present a derivation for above formula in chapter4.

As shown in Figure 3.11 (a) and (b) the density of states of the adsorbate on the substrate presents a peak at an energy very close to the on-site energy ϵ_d.The transmission is shown in (c) and (d) for the two on-site energies and different values of x. For small x $x \lessapprox 0.1$eV the transmission varies in accordance with the DOS (a and b). For large x and very close to the energy of resonance the transmission goes to zero and its variation with energy is in rough agreement with formula $T = 4\pi V^2 \frac{\Delta}{t^2} \tilde{N}(E) \propto |E|$.

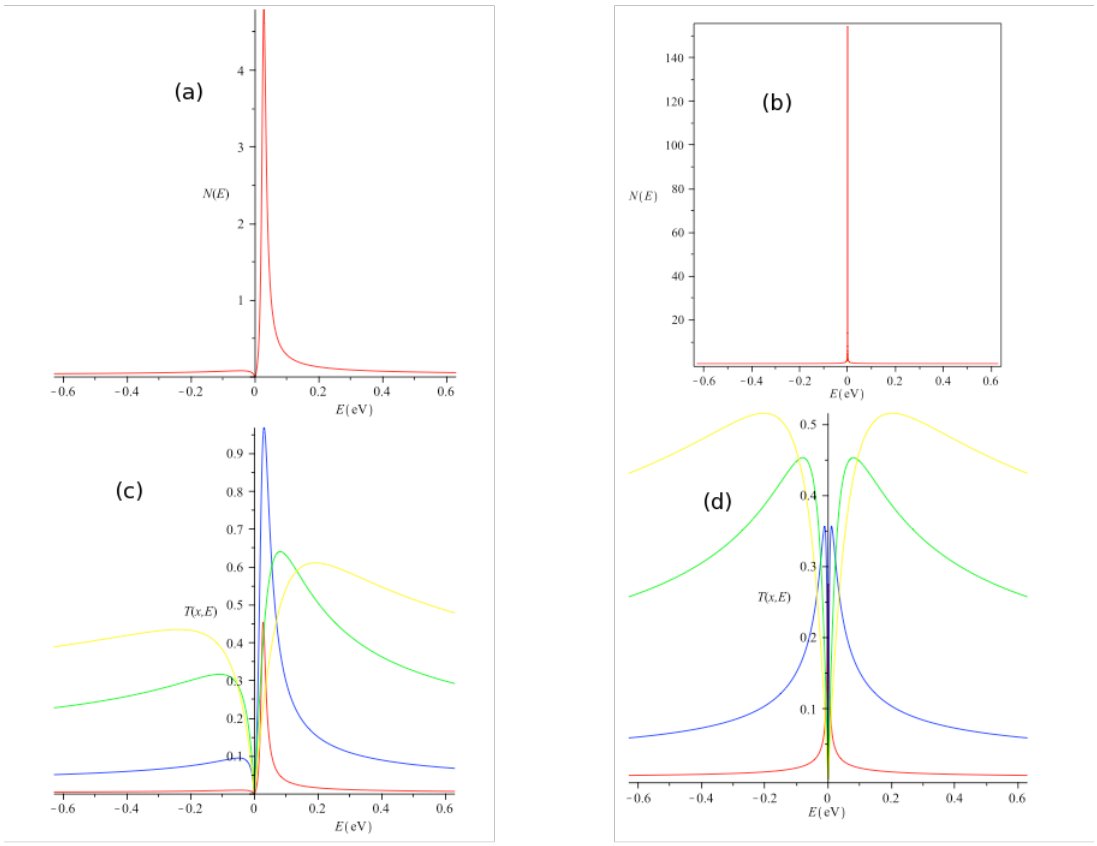

Figure 3.11: (TOP POSITION) DOS of the adsorbate without STM for the case of an adatom on top position, for different values of onsite energy (a) $\epsilon_d = 0.26$eV and (b) $\epsilon_d = 0.0$eV. Transmission T for the case of an adatom on top position for different values of coupling x between the apex atom of the tip and the adatom (c) on-site energy $\epsilon_d = 0.26$eV and (d) $\epsilon_d = 0.0$. Here different colors corresponds to different values of x as *red* $\equiv x = 0.01$eV, *blue* $\equiv x = 0.1$eV, *green* $\equiv x = 0.5$eV and *yellow* $\equiv x = 1.0$eV,

2) **Adatom in hollow position**

In that case the self-energy is given by [16]

$$\widetilde{\Sigma}_{\text{hollow}}(z) = -z\left[2\left(\frac{V}{D}\right)^2/(\pi t_0^2)\left\{D^2 + z^2 \ln\left|1 - \frac{D^2}{z^2}\right|\right\}\right] - 2i\pi\left(\frac{V}{D}\right)^2\left|\frac{z^3}{t_0^2}\right|\Theta\Big(D - |z|\Big) \tag{3.72}$$

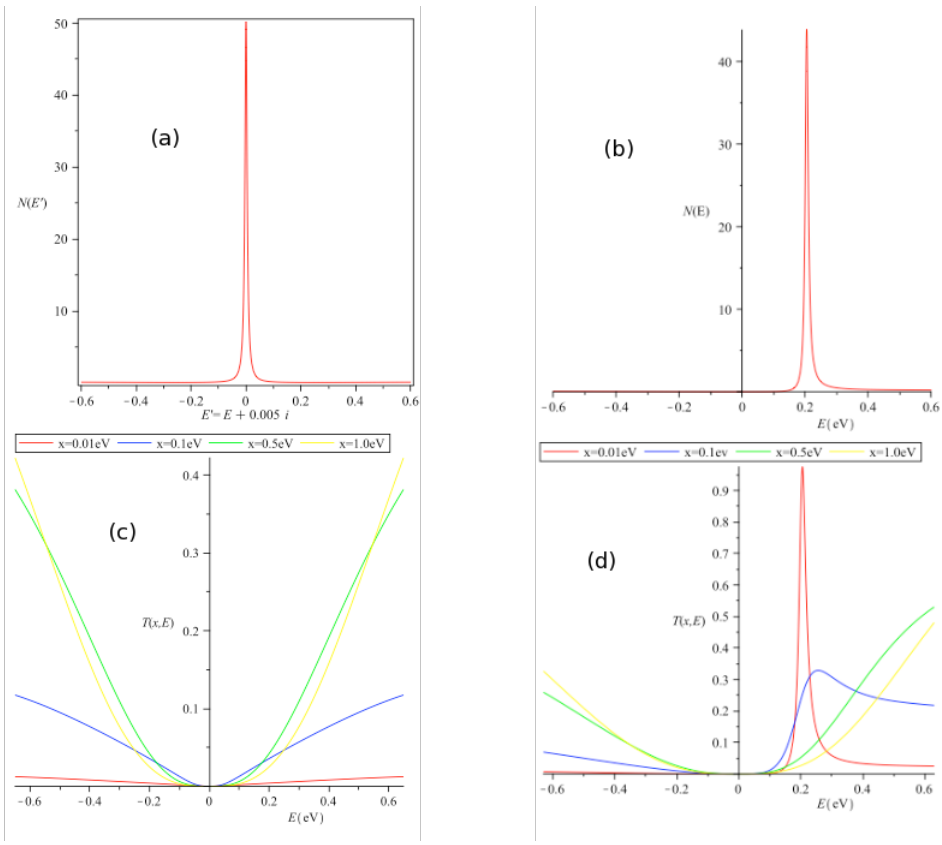

Figure 3.12: (HOLLOW POSITION) DOS of the adsorbate without STM for the case of an adatom in a hollow position for different values of on-site energy (a) $\epsilon_d = 0.0$eV and (b) $\epsilon_d = 0.26$eV. Transmission T for the case of adatom in a hollow for different values of coupling x between the apex orbital of the tip and the adatom (c) on-site energy $\epsilon_d = 0.0$eV and (d) $\epsilon_d = 0.260$. Here different colors corresponds to different values of x as *red* $\equiv x = 0.01$eV, *blue* $\equiv x = 0.1$eV, *green* $\equiv x = 0.5$eV and *yellow* $\equiv x = 1.0$eV,.

Where D and t_0 have the same values as mentioned before for top position case. Here

$V \sim 5$eV is the hybridization amplitude of the adatom with each of the nearest neighbors carbon atoms.

Here it is important to notice that the imaginary part in Equation 3.72 is much smaller than for Equation 3.71 i.e ($\frac{z^3}{t_0^2} \ll |z|$). This is due to interferences effect in the coupling between the s orbital of the adatom and the p_z orbitals of the six neighbors carbon atoms in the hollow geometry. This will favor *narrower resonance* as shown below. This means that an adsorbate in the hollow position is less coupled than in the top position

For small x, $x \lessapprox 0.01$ eV and $\epsilon_d = 0.26$eV, the $T(E)$ is close to the density of states in accordance with Tersoff-Hamann theory (Figure 3.12). But for larger x the Tersoff-Hamann theory fails. The transmission varies in accordance with equation 3.69 and is roughly $\propto |z|^3$. Note that for $\epsilon_d = 0$ is a singular case. Indeed the DOS on the adsorbate presents a delta peak ar $E = 0$ with a weight $\frac{1}{1 + \frac{2V^2}{\pi t_0^2}}$. This delta peak is made apparent in Figure 3.12 (a) due to a finite imaginary part of z, $\Im(z) = 0.005$eV. The transmission $T(E)$ does not present a peak and looks like the DOS ($\tilde{N} \propto |E|^3$) for $x \geq 0.5$eV.

3) **Adatom on metal substrate**

Here we have chosen a rectangular band-model $N(E) = \frac{1}{2W}$ for $-W < E < W$. In the present calculations we take $W = 10$eV which is a typical value for a metal. The Self-energy $\widetilde{\Sigma}_{\text{metal}}(z)$,

$$\widetilde{\Sigma}_{\text{metal}}(z) = \frac{V^2}{2W} \ln\Big(\frac{1 + W/z}{1 - W/z}\Big) \tag{3.73}$$

As shown in Figure 3.13 (a) the DOS of the adatom presents a wide resonance on a metallic substrate because the density of state of the metallic substrate is larger than for graphene (top or hollow). As a consequence the phenomena of anomalous STM image

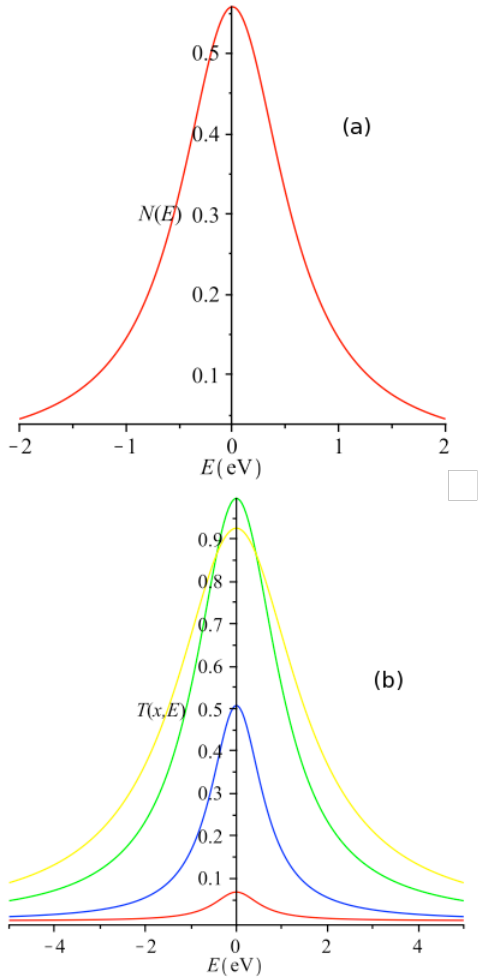

Figure 3.13: (METALLIC SUBSTRATE) DOS of the adsorbate without STM (a) and the transmission (b) for the case of metallic substrate here we take $\epsilon_d = 0$.

does not occur because the resonance is too large to reach to regime $x|g_{ad}| \gg 1$

To conclude we showed the phenomenon of the anti-resonance in the near field regime. This occurs for sufficiently narrow resonances and is favored in graphene by its low density of states. We find that the effect is stronger for the hollow position than for the top position. This anomalous STM images could be observed for other resonance states like vacancies

states. For the metallic substrate we find that the effect discussed here is absent.

Bibliography

[1] David K. Ferry.: *Transport in Nanostructures*, Cambridge University Press, Cambridge, 2009

[2] Massimiliano Di Ventra.: *Electrical Transport in Nanoscale Systems*, Cambridge University Press, Cambridge, 2008

[3] Eric Akkermans, *Mesoscopic Physics of Electrons and Photons*; Cambridge University Press; Reissue edition, 2011

[4] Drude, P., Annalen der Physik 1, 566 (1900).

[5] Boltzmann, L.W., Ber. Wien. Akad. 66, 275 (1872).

[6] Frenkel, J., Phys. Rev. **36**, 1604 (1930)

[7] Kubo, R., J. Phys. Soc. Japan 12, 570 (1959).

[8] Landauer, R., IBM J. Res. Dev. 1, 223 (1957).

[9] Datta, S., Electronic Transport in Mesoscopic Systems (Cambridge University Press, Cambridge, 1995.

[10] Landauer, Rolf; Philosophical Magazine, Vol. 21, p. 863-867

[11] C. L. Kane, R. A. Serota and P. A. Lee, Phys. Rev. B, **37**, 6701 (1988)

[12] Büttiker, M., IBM J. Res. Dev. **32**, 316 (1988).

[13] Kubo, R., Rep. Prog. Phys. 29, 255 (1966)

[14] Pierre Darancet, Valerio Olevano, Didier Mayou; Phys Rev B **81**, 155422 (2010)

[15] Blanco, Jose Manuel; Flores, Fernando; Prez, Rubn; Progress in Surface Science, Volume 81, Issue 10-12, p. 403-443 (2006)

[16] Bruno Uchoa, Ling Yang, S.-W. Tsai, N. M. R. Peres, A. H. Castro Neto; arXiv 1105.4893v2 [cond-mat.mes-hall]

CHAPTER IV

Adsorbates on Graphene

Abstract

In this chapter we consider the electronic structure of adsorbates on graphene. These adsorbates can be atoms as H, O, F or molecules as OH and also many others. It has been shown that they tend to produce resonances (also called mid-gap states) close to the Dirac energy. These resonances create in particular a modification of the density of states around the adsorbate, in the graphene plane. This in turn induces a charge transfer and variation of the electrostatic potential which are important to determine. After an introduction to the subject in part 4.1 we give the basic Hamiltonian and the formalism in section 4.2. Our first results are presented in section 4.3 and suggest a moderate variation of the electrostatic potential due to charge transfer.

4.1 Introduction

In this chapter, we discuss how some electronic properties of graphene are modified by chemical doping, usually by the sparse adsorption of atoms or molecules. This topic is of

fundamental importance, because by their nature, adsorbates not only can donate electrons or holes to graphene but also can play a role as defects, disrupting the lattice symmetry fromwhich the unique properties of graphene such as the important pseudospin degree of freedom are derived.

Graphene-like materials could be used in the fabrication of electronic and optoelectronic devices, gas sensors, biosensors, and batteries for energy storage. To enable many of these new technologies, it is necessary to understand and control the interaction of graphene with adsorbates. This need arises on the one hand because adsorbates can modify the intrinsic properties of graphene, leading to new and useful behaviors, and on the other hand because adsorbates can limit the conductivity of graphene, which can adversely impact electronic devices.

Point defects occur predominantly within the graphene plane in [1] the form of lattice vacancies and impurity atoms. The occurrence of impurities can be either in substitutional or interstitial sites and can be in the form of isotopic impurities [1], which predominantly perturb the phonon spectra. Yet many chemical species are known to adsorb readily to graphene like for example H, F, and O atoms and OH molecules. These adsorbed species bond covalently to graphene and strongly affect its electronic structure:

As is shown in Fig. 4.1, the graphene carbon atoms to which the atoms or molecules bond move out of the graphene plane toward the adsorbed moiety by fractions of an Angstrom and thus partial rehybridization of the graphene electronic structure occurs locally from the sp^2 bonding of the planar graphene to the sp^3 bonding characteristic of carbon atoms in tetrahedral geometries.

As a result, it is reasonable to expect these adsorbed species to strongly scatter elec-

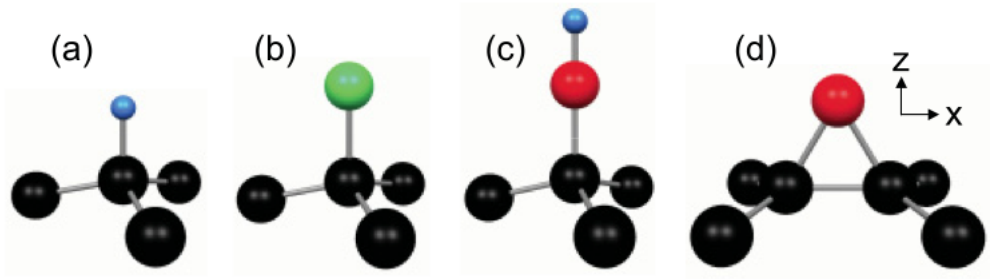

Figure 4.1: Relaxed geometries of adsorbates on graphene. C, H, F, and O atoms are black, blue, green, and red respectively (a) Adsorbed hydrogen atom. H and C atoms to which H binds are 1.47 and 0.35 Å above graphene plane. (b) Adsorbed fluorine. F and C atoms to which F binds are 1.83 and 0.36 Å above graphene plane. (c) Adsorbed hydroxyl group. H, O, and C atoms to which O binds are 2.78, 1.83, and 0.41 Å above graphene plane. (d) Adsorbed oxygen. O and C atoms to which O binds are 1.51 and 0.27 Å above graphene plane. The C atoms to which the O binds are separated by 1.47 Å . The x axis is parallel to the line joining the C atoms to which the O binds. Adopted from [2]

trons in graphene and modify the electronic properties. In this chapter we shall mainly be concerned with charge transfer and electrostatic potential around these adsorbates.

4.2 Formalism for Adsorbates on Graphene and Dirac Point Resonances

We will adopt an approach based on a tight-binding Hamiltonian Ha that is a generalization of the Hamiltonian H given in chapter1 . We describe also a theoretical methodology for studying these Dirac point resonances through the T-matrix.

4.2.1 Tight Binding Hamiltonian for Adsorbates on Graphene

The tight binding Hamiltonian H_a for adsorbate has the form [2]

$$\mathcal{H}_a = \mathcal{H}_0 + \sum_{\alpha} \epsilon_\alpha d_\alpha^\dagger d_\alpha + \sum_{\alpha,j} \gamma_{\alpha j}\left(d_\alpha^\dagger a_j + h \cdot c.\right) \tag{4.1}$$

where

$$\mathcal{H}_0 = -\sum_{\langle i,j \rangle} t_{ij}\left(a_i^\dagger a_j + h \cdot c.\right) \tag{4.2}$$

describes the graphene band electrons with the energy scale chosen so that the energy of the $2p_z$ orbitals of the graphene carbon atoms is set to zero. a_j is the destruction operator for an electron in the $2p_z$ orbital ϕ_j of carbon atom j . $d_\alpha^\dagger$ is the creation operator for an electron in an extended molecular orbital (EMO) ψ_α that is associated with an adsorbed atom or molecule and ϵ_α is the energy of that orbital. Also $\gamma_{\alpha j} = \langle \psi_\alpha | \mathcal{H} | \phi_j \rangle$ is the matrix element of the Hamiltonian between the $2p_z$ orbital ϕ_j of carbon atom j and EMO ψ_α. The carbon valence orbitals included in the EMOs are those other than the $2p_z$ orbitals of the graphene π band that are already included in the theory through the term $\mathcal{H}_0$ in (4.2).

Inclusion of the graphene carbon orbitals other than the $2p_z$ orbitals (i.e., the carbon $2s$, $2p_x$, and $2p_y$ orbitals of the carbon atom(s) to which the adsorbed atom or molecule bonds and of its nearest carbon atom neighbors) in the theory in this way turns out to be important. Indeed these orbitals take part in the rehybridization of the graphene from sp^2 to sp^3 bonding induced by the adsorbate that strongly affects the electronic structure of the system and its transport properties.

4.2.2 Effective Hamiltonian for Adsorbates on Graphene

In the simplest possible model of an adsorbate represented by just one atomic orbital α that couples only to the $2p_z$ orbital of only one carbon atom j of the graphene, the tight-binding Hamiltonian of the graphene and adsorbate is [2]

$$\mathcal{H}_1 = \mathcal{H}_0 + \epsilon_\alpha d_\alpha^\dagger d_\alpha + \gamma_{\alpha j}\left(d_\alpha^\dagger a_j + h \cdot c.\right) \tag{4.3}$$

where the notation is as in (4.2). The eigenstate $|\psi\rangle$ of $\mathcal{H}_1$ with energy eigenvalue ϵ can be written as $|\psi\rangle = |\psi_g\rangle + |\psi_a\rangle$ where $|\psi_g\rangle$ and $|\psi_g\rangle$ are the projections of $|\psi\rangle$ onto the space spanned by the $2p_z$ orbitals of graphene and onto the orbital of adsorbed atom, respectively.With these definitions, it has been shown [3] that $|\psi_g\rangle$ is an exact eigenstate of an effective Hamiltonian

$$\mathcal{H}_{eff} = \mathcal{H}_0 + V_j a_j^\dagger a_j \tag{4.4}$$

with the same energy eigenvalue ϵ as $|\psi\rangle$. Here

$$V_j = \gamma_{\alpha j}^2/(\epsilon - \epsilon_\alpha) \tag{4.5}$$

Thus for the purpose of calculating the scattering in graphene with such an adsorbed atom, the Hamiltonian $\mathcal{H}_1$ can be replaced with $\mathcal{H}_{eff}$, i.e., the Hamiltonian of graphene without the adsorbed atom but with an energy dependent potential $\gamma_{\alpha j}^2/(\epsilon - \epsilon_\alpha)$ on carbon atom j of the graphene sheet.

With more than one EMO and/or bonding to more than one graphene atom the result is an effective Hamiltonian [2]

$$\mathcal{H}_{eff} = \mathcal{H}_0 + \sum_{i,j} V_{ij} a_i^\dagger a_j \tag{4.6}$$

with

$$V_{ij} = \sum_\alpha \gamma_{\alpha i} \gamma_{\alpha j}^* / (\epsilon - \epsilon_\alpha) \tag{4.7}$$

where i and j label the graphene carbon atoms to which the adsorbate bonds and α labels the EMOs associated with the adsorbate that are described in Sect. 4.1. With this generalization, the effective Hamiltonian applies to the H, F, OH, and O adsorbates and to many others.

In principle the generalization to several EMO is required even for the case of H which has only one valence orbital in order to properly treat the effect of the rehybridization of the graphene from sp^2 to sp^3 bonding induced by the adsorption of a H atom.

4.2.3 The $\mathcal{T}$-Matrix Formalism

The $\mathcal{T}$-matrix formalism of scattering theory (not to be confused with the transmission probability matrix $T_{ij}(E)$ of the Landauer transport formalism discussed in Chapter 3) has yielded valuable insights into the resonant scattering of electrons in graphene by impurities and adsorbates . The T-matrix is defined [appendix B] by

$$\mathcal{G} = \mathcal{G}_0 + \mathcal{G}_0 \mathcal{T} \mathcal{G}_0 \tag{4.8}$$

where $\mathcal{G} = (\epsilon + i\eta - \mathcal{H}_{eff})^{-1}$ is the full Green's function based on the effective Hamiltonians $\mathcal{H}_{eff}$ discussed in Sect. 4.1.2 for a single adsorbed atom or molecule and

$\mathcal{G}_0 = (\epsilon + i\eta - \mathcal{H}_0)^{-1}$ is the unperturbed Greens function for π band electrons in clean graphene with $\mathcal{H}_0$ given by (4.2). $\mathcal{T}$ characterizes the strength of the scattering of electrons at energy ϵ due to the presence of the adsorbate. It can be written in the standard form [appendix A]

$$\mathcal{T} = \mathcal{V} + \mathcal{V}\mathcal{G}_0\mathcal{V} + V\mathcal{G}_0\mathcal{V}\mathcal{G}_0\mathcal{G}_0\mathcal{V} + \cdots \tag{4.9}$$

where, according to (4.4) and (4.5), $\mathcal{V} = a_j^\dagger a_j \sum_\alpha |\gamma_{\alpha j}|^2/(\epsilon - \epsilon_\alpha)$ for a H, F, OH atom or molecule with EMOs α bound to carbon atom j. Taking matrix elements of (4.7) between the graphene $2p_z$ orbitals of the carbon atom(s) to which the adsorbed atom or molecule binds and summing the resulting series yields

$$\tilde{\mathcal{T}} = (\mathbb{1} - \tilde{\mathcal{V}}\tilde{\mathcal{G}}_0)^{-1}\tilde{\mathcal{V}} \tag{4.10}$$

The strength of scattering associated with a defect is in general proportional to the square modulus of appropriate matrix elements of the $\mathcal{T}$ -matrix. Thus, the energies ϵ at which resonant scattering by H, F, OH and O adsorbates should occur are those at which $|\langle m|\mathcal{T}|n\rangle|^2$ have maxima. As can be seen in Fig. 4.2, strong scattering resonances are predicted to occur in the vicinity of the Dirac point energy $\epsilon = 0$ for all four adsorbed species. The electron energy ϵ_{DR} at which the resonance is centered depends on the adsorbed species. $\epsilon_{DR} = -0.136t, -0.089t, -0.0026t$ for F, OH, and H, respectively. For O, there is a narrow peak near $0.112t$ that overlaps a broader peak centered near $0.090t$. In addition to these Dirac point resonance for O there is an antiresonance (i.e., deep minimum in the scattering strength) near $0.55t$.

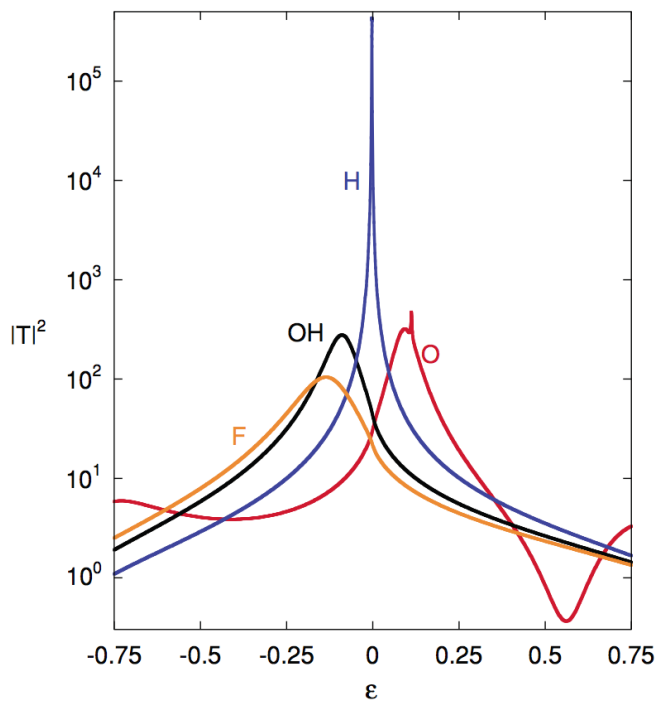

Figure 4.2: Calculated square modulus of the $\mathcal{T}$ -matrix vs. electron energy ϵ for an H, F, or O atom or OH group adsorbed on graphene in the geometries shown in Fig. 4.1. $\mathcal{T}$ and ϵ are in units of $t = 2.7$ eV. The Dirac point of graphene is at $\epsilon = 0$. For H, F, and OH $\mathcal{T} = \langle 1|\mathcal{T}|1\rangle$. For O the square of the Frobenius norm of the matrix $\mathcal{T} = \langle m|\mathcal{T}|n\rangle$ is plotted. The EMOs included in this calculation are linear combinations of the atomic valence orbitals of the adsorbed species and the $2s$, $2p_x$, and $2p_y$ valence orbitals of each of the carbon atoms shown in Fig. 4.1 for the respective adsorbed species. Thus the local rehybridization of the graphene from the sp^2 to sp^3 bonding is included in the model. The overlaps $\sigma_{\alpha j}$ between the EMOs and the $2p_z$ orbitals of the carbon atoms to which the adsorbed moieties bond are included in the calculations. Taken from [2]

By far the strongest resonance (and the closest one to the Dirac point) is found for hydrogen. Electron scattering associated with this resonance is so strong that in electron transport in nanoribbons the adsorbed H atom scatters electrons in a way almost identical to a carbon atom vacancy, i.e., as if the carbon atom to which the H atom binds is missing

entirely from the graphene lattice.

To conclude the scattering of the electrons in graphene by covalently bonded adsorbates presents strong resonances with an unusual property. Instead of the scattering resonances occurring near the energies of atomic or molecular orbitals of the adsorbate or impurity as would be the case for a weakly couple adsorbate, the strongly coupled moieties gives rise to strong scattering resonances at energies close to the Dirac point energy of graphene.

4.3 Density of states around an adsorbate

In this section we compute the DOS around the adsorbate using the Green's function formalism. We recall first the expression of Green's function and then use it to express the DOS.

4.3.1 Green's function of the host (graphene)

Let only the zeroth site on the A sublattices be occupied by an impurity. Then, the diagonal element of the Greens function $\hat{\mathcal{G}} = (\epsilon - \hat{\mathcal{H}})^{-1}$ on this site [4],

$$\mathcal{G}_0 = \frac{g_0}{1 - V_L g_0} \tag{4.11}$$

where g_0 is the diagonal element of the Greens function in the host, $\hat{g} = (\epsilon - \hat{\mathcal{H}}_0)^{-1}$. The site-diagonal elements g_0 are equal on both sublattices and can be easily obtained by approximating the Brillouin zone with a circle,

$$g_0 = \frac{1}{\mathcal{S}_{BZ}} \int \frac{E}{E^2 - E^2(\boldsymbol{k})} d\boldsymbol{k}\,, \tag{4.12}$$

where the integration is carried over the entire Brillouin zone, which has the area

$$\mathcal{S}_{BZ} = \frac{8\pi^2}{\sqrt{3}a^2}\,, \tag{4.13}$$

and $E(\boldsymbol{k})$ is the unperturbed dispersion relation corresponding to the host Hamiltonian(pure Graphene's Hamiltonian). In practical situations the Fermi level in graphene is located, nearly unavoidably, in a narrow spectral region, in which the dispersion is linear with a good accuracy. Near each of the two inequivalent Dirac points, the dispersion relation $E(\boldsymbol{k})$ can be expanded. The integration can be performed exactly (In details derivation can be found in [5]).

$$g_0 \approx \frac{4\pi}{\mathcal{S}_{BZ}} \int_0^{k_{max}} \frac{E}{E^2 - (v_F k')^2} k' dk'\,, \tag{4.14}$$

$$= \int_0^1 \frac{E}{E^2 - \sqrt{3}\pi t^2 x} dx$$

Finally one has [6]

$$g_0 \approx \frac{E}{D^2} \ln |\frac{E^2}{D^2 - E^2}| - i\pi N_0(E), \tag{4.15}$$

where $N_0(E) = \frac{|E|}{D^2}\Theta(D - |E|)$ and D is a high-energy cutoff of order of the graphene bandwidth $D = \sqrt{\sqrt{3}\pi t} \approx 6$eV. The cutoff D is taken using the Debye prescription [7] i.e. conservation of the number of states in the Brillouin zone after linearization of the

spectrum around K point.

Comparison of 4.15 with the results of an exact numerical calculation showed it to be accurate in the range $|\epsilon|/t \leqslant 0.8$ [2]. Here, $t = 2.7$ eV is the modulus of the Hamiltonian matrix element between the $2p_z$ orbitals of nearest-neighbor carbon atoms i and j of the pristine graphene lattice. Note that improved approximate analytic expressions for $g_0(E)$ has been given in [2]

$$\langle 1|\mathcal{G}_0|1\rangle = \frac{\epsilon\alpha(\epsilon)}{\sqrt{3}\pi t^2}\ln\Big(\frac{\epsilon^2}{\sqrt{3}\pi t^2 - \epsilon^2}\Big) - i\frac{|\epsilon|\beta(\epsilon)}{\sqrt{3}t^2} \tag{4.16}$$

where $\alpha(\epsilon) = 1.07(1 + 0.66\epsilon^2/t^2)$ and $\beta(\epsilon) = 1 + 0.31\epsilon^2/t^2 + 0.33\epsilon^4/t^4$.

We also the off-diagonal elements of the Green's function of the host (Graphene)[8] which are given by:

$$\mathcal{G}_{AA} = \mathcal{G}_{BB} = \frac{-E\cos(\boldsymbol{K}\cdot\boldsymbol{r})}{\pi v_F^2}K_0(-iEr/v_F), \tag{4.17}$$

where $\mathcal{G}_{AA}$ and $\mathcal{G}_{BB}$ are the diagonal elements of the host's Green's function, and

$$\mathcal{G}_{AB} = \frac{iE\sin(\boldsymbol{K}\cdot\boldsymbol{r} + \phi)}{\pi v_F^2}K_1(-iEr/v_F), \tag{4.18}$$

where ϕ is the angle between $\boldsymbol{K}$ (Dirac point) and $\boldsymbol{r}$ and $K_{0,1}$ denote modified Bessel functions of second type. The function $\mathcal{G}_{BA}$ can be obtained from the relation $\mathcal{G}_{BA}(\boldsymbol{r}) = \mathcal{G}^*_{BA}(-\boldsymbol{r})$ giving

$$\mathcal{G}_{BA} = \frac{iE\sin(\boldsymbol{K}\cdot\boldsymbol{r} - \phi)}{\pi v_F^2}K_1(-iEr/v_F), \tag{4.19}$$

4.3.2 Spatial Variation of the DOS

The density of states of the localized level reads [7]:

$$\rho(E, \epsilon_d) = -\frac{1}{\pi}\Im\frac{1}{E - \epsilon_d - \Sigma(E) + io^+}, \tag{4.20}$$

for the self energy by Eq. 4.20 we have [7]:

$$\Sigma(E) = V^2 g_0(E) = -V^2\frac{E}{D^2}\ln\Big(\frac{|E^2 - D^2|}{E^2}\Big) - iV^2\frac{\pi|E|}{D^2}\Theta(D - |E|), \tag{4.21}$$

Then the DOS of the localized level reads [7]:

$$\rho(E, \epsilon_d) = \frac{1}{\pi}\frac{\Delta|E|\Theta(D - |E|)}{[EZ^{-1}(E) - \epsilon_d]^2 + \Delta^2 E^2}, \tag{4.22}$$

where $Z^{-1}(E) = 1 + (V/D)^2\ln(|D^2 - E^2|/E^2)$ is real part of $\Sigma(E)$ and $\Delta = \pi V^2/D^2$. For Hydrogen adsorbate $V = 5.2eV$ and $\epsilon_d = 0.26eV$.

The spatial variation of the LDOS due to impurity are given by [9; 10]:

$$\Delta\rho(\boldsymbol{r}, \epsilon_d, E) = -\frac{1}{\pi}\Im[\mathcal{G}(-\boldsymbol{r}, E)\mathcal{T}(E, \epsilon_d)\mathcal{G}(\boldsymbol{r}, E)], \tag{4.23}$$

where

$$\mathcal{T}(E, \epsilon_d) = \frac{V^2}{E - \epsilon_d - V^2 g_0(E)} \tag{4.24}$$

So for a localized impurity (e.g Hydrogen atom) on the A sub lattice we can write:

$$\Delta\rho(\boldsymbol{r}, \epsilon_d, E) = -\frac{1}{\pi}\Im\Big\{[\mathcal{G}_{AA}(-\boldsymbol{r}, E)\mathcal{G}_{AA}(\boldsymbol{r}, E)]\mathcal{T}(E, \epsilon_d)\Big\}, \tag{4.25}$$

If **r** is on the A sublattice, or

$$\Delta\rho(\boldsymbol{r}, \epsilon_d, E) = -\frac{1}{\pi}\Im\Big\{[\mathcal{G}_{AB}(-\boldsymbol{r}, E)\mathcal{G}_{BA}(\boldsymbol{r}, E)]\mathcal{T}(E, \epsilon_d)\Big\}, \tag{4.26}$$

If **r** is on the B sublattice. After some calculations we have

$$\Delta\rho_A(\boldsymbol{r}, \epsilon_d, E) = -\frac{1}{\pi}\Big(\frac{E}{\pi v_F^2}\Big)^2 \cos^2(\boldsymbol{K}\cdot\boldsymbol{r})\Im\Big[K_0^2(-iEr/v_F)\mathcal{T}(E, \epsilon_d)\Big] \tag{4.27}$$

if $\boldsymbol{r}$ is in the vicinity of an A site and

$$\Delta\rho_B(\boldsymbol{r}, \epsilon_d, E) = -\frac{1}{\pi}\Big(\frac{E}{\pi v_F^2}\Big)^2 \sin^2(\boldsymbol{K}\cdot\boldsymbol{r} - \phi)\Im\Big[K_1^2(-iEr/v_F)\mathcal{T}(E, \epsilon_d)\Big] \tag{4.28}$$

if $\boldsymbol{r}$ is in the vicinity of an B site.

4.4 Charge Transfer and the Electrostatic Potential around adsorbate

Using the above expression of the density of states we can now calculate the charge density and then the electrostatic potential created by this charge density.

The variation of the integrated density of states due to the impurity are:

$$\Delta n(\boldsymbol{r}, \epsilon_d) = \int_{-D}^{E_F} \Delta\rho(\boldsymbol{r}, \epsilon_d, E)dE \tag{4.29}$$

Where E_F is the Fermi energy that will be taken equal to zero in the following calculations (neutral graphene).

By adding equation 4.27 and 4.28 we can compute spatial variation of charge per unit cell area $\Delta\sigma(r)$

$$\Delta\sigma(r) = e\,\Delta n(r) \tag{4.30}$$

where e is the electron charge. Figure 4.3 shows the variation of charge per unit cell which is due to a charge transfer between the adsorbate and the graphene plane and also to charge coming from infinity, somewhere in graphene. This is because we assumed that chemical potential is fixed in our problem. Note that in Figure4.3, both $\cos^2(\boldsymbol{K}\cdot\boldsymbol{r})$ and $\sin^2(\boldsymbol{K}\cdot\boldsymbol{r}-\phi)$ are replaced by their average value $1/2$. This makes $\Delta\sigma(\mathbf{r})$ isotropic but preserves its order of magnitude and its variation on long distances.

We are interested in calculating change in potential energy of electron at position $\boldsymbol{r}$ due to charge transfer around the adsorbate. In continuous notations we have:

$$\Delta V(r) = \frac{e^2}{4\pi\varepsilon_0}\int\int\frac{\Delta\rho(\boldsymbol{r}',\epsilon_d,E)}{|\boldsymbol{r}-\boldsymbol{r}'|}dEd\boldsymbol{r}' \tag{4.31}$$

in polar plane we have:

$$\Delta V(r) = \int_0^{2\pi}\int_{r'=a_0}^{r}\int_{-D}^{E_F}\frac{\Delta\rho(\boldsymbol{r}',\epsilon_d,E)}{\sqrt{r^2-2r'r\cos\theta+r'^2}}dEr'dr'd\theta \tag{4.32}$$

This does not look easy to sum up because of the short wavelength pattern. However, since the short wavelength pattern does not carry energy dependence, we might try to approximate the sum by substituting both $\cos^2(\boldsymbol{K}\cdot\boldsymbol{r})$ and $\sin^2(\boldsymbol{K}\cdot\boldsymbol{r}-\phi)$ by their average value $1/2$. Then the remaining dependence on atomic position is through the Bessels only, and slow on the atomic scale, if the energy is close to the Dirac point.

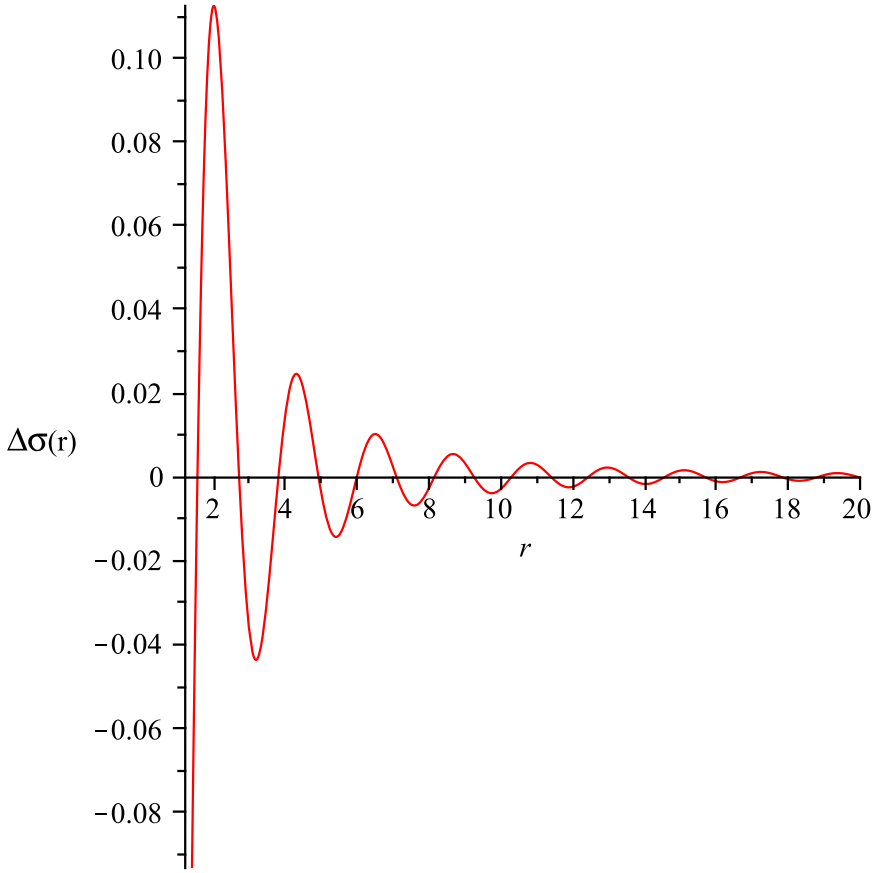

Figure 4.3: The spatial variation of charge per unit cell area versus distance (unit of Angstrom) from Hydrogen adatom in graphene sheet ($\varepsilon_d = 0.26eV$ all the parameters are in the text).

By using following integral relation [11]

$$\int_0^{2\pi} \frac{d\theta}{\sqrt{a \pm b\cos\theta}} = \frac{4}{\sqrt{a+b}} K(\sqrt{\frac{2b}{a+b}}) \tag{4.33}$$

where $K(a)$ is the complete elliptic integral, we can write

$$\Delta V_{A/B}(r) = -\frac{2}{\pi^3 v_F^4}\Im \int_{-D}^{E_F}\int_{r'=a_0}^{r} \frac{r'}{r+r'} K(\frac{2\sqrt{rr'}}{r+r'})\Big[K_{0/1}^2(-iEr/v_F)E^2\mathcal{T}(E,\epsilon_d)\Big]dr'dE \quad (4.34)$$

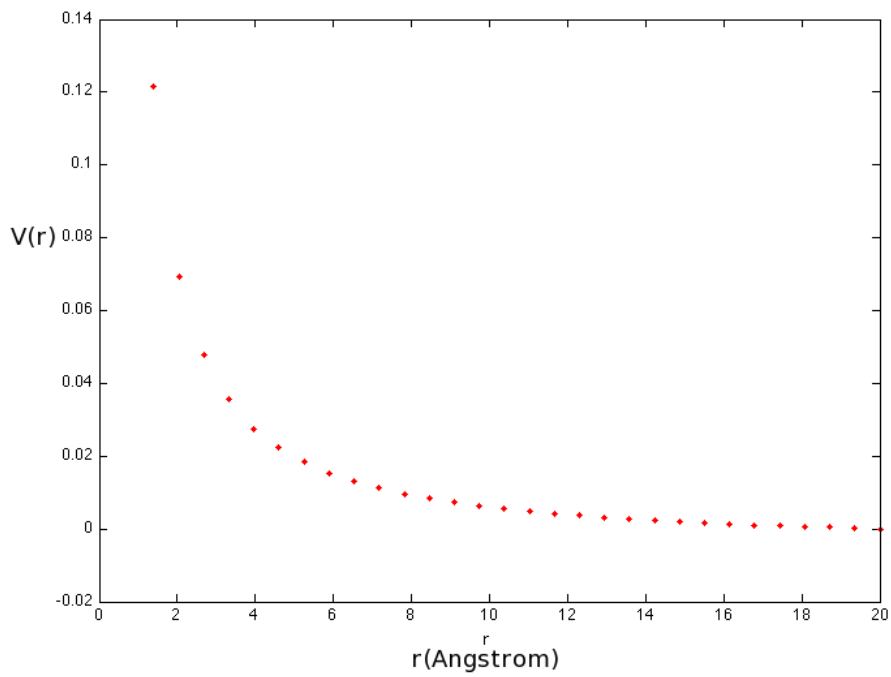

Figure 4.4: The spatial variation of average electrostatic potential in eV versus in-plane distance from Hydrogen adsorbate .

Our results in Figure 4.4 is well comparable with work by Katsnelson [12] for Hydrogen. We find a relatively modest variation of the electrostatic potential of the order of 0.1 eV at most.

To conclude we have shown it is possible to get an estimate of the charge density around an adsorbate and to compute the corresponding electrostatic potential in a simple

tight-binding model. A full study with respect to various parameters (especially ϵ_d) will be done starting from this preliminary work.

Bibliography

[1] Paulo T. Araujo, Mauricio Terrones, and Mildred S. Dresselhaus; Materials Today 15(3), 98-109 (2012)

[2] Siarhei Ihnatsenka and George Kirczenow; Phys. Rev. B **83**, 245442 (2011)

[3] John P. Robinson, Henning Schomerus, Lszl Oroszlny, and Vladimir I. Falko

[4] Yu. V. Skrypnyk and V. M. Loktev; PRB **73**, 241402 (R) (2006)

[5] Yu. V. Skrypnyk and V. M. Loktev; PRB **82**, 085436 (2010)

[6] T. O. Wehling, S. Yuan, A. I. Lichtenstein, A. K. Geim, and M. I. Katsnelson; PRL**105**, 056802 (2010)

[7] Bruno Uchoa, Valeri N. Kotov, N. M. R. Peres, and A. H. Castro Neto; PRL **101**, 026805 (2008)

[8] Andrei V. Shytov, Dmitry A. Abanin, and Leonid S. Levitov; PRL **103**, 016806 (2009)

[9] Cristina Bena; PRL **100**, 076601 (2008)

[10] Antonios Gonis; *Green functions for ordered and disordered systems* North-Holland 1992

[11] A. P. Brychkov, Yu. A. Marichev, O. I. Prudnikov; *Integrals and Series; Volume 2 : Special Functions* Gordon and Breach Science Publishers; (1998)

[12] B. Sachs, T. O. Wehling, A. I. Lichtenstein and M. I. Katsnelson, Theory of Doping: Monovalent Adsorbates, in ”Graphene, Theory, Research and Applications”, InTech, Rijeka (Croatia) (2011).

Conclusion

Le graphène est constitué d'une couche atomique de carbone, disposée selon un réseau nid d'abeille, qui possède des propriétés électroniques uniques. Les porteurs de charge sont des fermions de Dirac sans masse et la structure électronique originale entraine des propriétés telles que , conductivité électrique minimale, effet Hall quantique anormal, effet tunnel de Klein, conductivité optique universelle notamment.

Cette thse a port sur les proprits lectroniques de deux structures lmentaires lchelle nanomtrique qui sont maintenant produites couramment par les exprimentateurs. Il sagit des biplans tourns de graphène et des adsorbats rsonants comme lhydrogne par exemple. Pour chaque systme nous avons considr le problme de sa structure lectronique et la description de certaines proprits de transport.

Les biplans tourns de graphène ont été découverts en particulier dans le graphène produit à partir du carbure de silicium. Ils présentent des propriétés originales par rapport aux biplans de type AB tels qu'on en trouve dans le graphite. Il a été montré que le paramètre principal qui dicte les propriétés électroniques est l'angle de rotation θ entre les deux couches lorsque l'on part d'un biplan AA. Lorsque cet angle est grand (modulo 60°) les deux plans apparaissent comme électroniquement découplés. Mais lorque cet angle diminue une physique riche apparaît. En particulier des études précédant cette thèse ont montré que la vitesse des électrons est renormalisée et diminue lorsque l'angle diminue. Pour des angles qui ne sont pas trop petits ($\theta > 2 - 3°$) ce phénomène peut se décrire au moyen d'une théorie de perturbation.

Dans cette thèse nous avons analysé la densité d'états en fonction de la position dans un

plan, toujours en utilisant une théorie perturbative valable pour des angles qui ne sont pas trop petits ($\theta > 2 - 3°$). Nous avons montré que la densité d'états présente des oscillations sinusoïdales avec la position dans le plan , qui ont la périodicité du Moiré produit par le biplan. Il est intéressant de constater que le maximum de la densité d'états est obtenu dans la zone dont l'empilement est localement de type AA. Ainsi ces modulations prfigurent le phénomène de localisation dans les zones AA qui se produit aux très petits angles ($\theta < 2°$). La variation relative de la densité d'états est indépendante de l'énergie (près de l'énergie de Dirac) et l'amplitude de l'oscillation varie comme l'inverse du carré de l'angle θ. La formule analytique que nous avons obtenue se compare bien à des calculs numériques réalisés sur le modéle de liaisons fortes.

L'amplitude de la modulation de la densité d'états est compatible avec le signal observé dans les expériences de STM (microscopie à effet tunnel). Toutefois le signal STM pourrait avoir une contribution venant de londulation des plans de graphène. En effet il est difficile de faire la distinction entre le signal provenant de l'ondulation des plans ou provenant d'une modulation relative de la densité d'états qui est indépendante de l'énergie. Ainsi, malgré nos efforts, l'origine du signal STM présentant des Moirés n'est toujours pas complètement résolue à présent.

Nous discutons aussi l'effet du désordre sur la durée de vie des électrons et sur le transport dans les biplans tournés. Plus précisément nous considérons le cas le désordre est présent dans un seul plan. La question est alors de savoir comment le désordre dans un plan affecte le transport dans le biplan. Si les deux plans étaient découplés le plan presque sans défauts aurait une conductivité très élevée qui déterminerait la conductivité du biplan. Cependant les électrons du plan sans défauts sont toujours finalement diffusés

par le désordre dans l'autre plan à cause du couplage. Dès lors la conductivité du biplan est dominée par l'effet du couplage qui dépend lui même fortement de l'angle de rotation θ .

Une approche perturbative montre que, pour un désordre donné dans un plan, la durée de vie des électrons de l'autre plan augmente comme le carré de l'angle de rotation θ. Partant de cette estimation nous pouvons proposer une formule pour la conductivité du biplan. Nous avons comparé cette formule à des résultats numériques essentiellement exacts. L'accord trouvé est bon.

Nos résultats pourraient être relevants aussi pour les nanotubes multi-parois qui prsentent une situation similaire. Ici la paroi externe du nanotube peut être modifiée par exemple de façon chimique alors que les parois internes sont protégées et restent essentiellement parfaites. La conductivité globale peut alors tre sensible au couplage entre les parois internes et externes. Dans le cas du biplan de graphène le paramètre dominant est l'angle de rotation θ entre les deux plans. Pour les nanotubes multi-parois le paramètre équivalent est l'angle de rotation entre les vecteurs chiralité des différentes parois. Donc notre étude suggère que pour les nanotubes multi-parois cet angle est un paramètre essentiel du transport électronique du nanotube. Bien sûr cette analyse est en principe valide pour les nanotubes dont le diamtre est suffisamment élevé (plusieurs nanométres) et d'autres paramètres pourraient jouer un rôle important pour des nanotubes de diamètre plus faible.

Nous avons aussi considéré dans cette thèse le rôle joué par des adsorbats comme l'atome d'hydrogène. Une caractéristique centrale de ces adsorbats est qu'ils produisent une résonance près de l'énergie de Dirac. Les adsorbats peuvent non seulement donner des

électrons ou des trous au plan de graphène mais peuvent jouer aussi une rôle de défauts en détruisant la symétrie locale du réseau. Les matériaux à base de graphène pourraient être utilisés dans la fabrication de constituants électroniques ou optoélectroniques, dans les détecteurs de gaz, les bio-senseurs les batteries et les systmes de stockage de l'énergie. Pour permettre ces nouvelles technologies il est nécessaire de comprendre et de contrôler l'interaction du graphène avec des adsorbats.

Plusieurs études théoriques en particuliers ab-initio ou en liaisons fortes ont été réalisées pour étudier le transfert de charge par les adsorbats. Ici nous avons démarré une étude basée sur le modèle continu (équation de Dirac). Cette approche permet d'étudier le transfert de charge en fonction de l'énergie de site de l'orbitale de l'adsorbat et de son couplage avec le plan de graphène. Nous avons présenté nos premiers résultats. Clairement cette approche devra être poursuivie pour analyser en détail le rôle des différents paramètres sur le transfert de charge et le potentiel électrostatique autour de l'adsorbat.

Les adsorbats résonants peuvent être étudiés expérimentalement en particulier par des études de STM. Comme nous l'avons montré cette signature STM pourrait être particulière. Pour cette étude théorique nous avons utilisé le formalisme des fils effectifs développé récemment à l'Institut Néel. Partant de ce formalisme nous dérivons un modèle qui est particulièrement simple, si l'on considère le cas d'un seul canal de conduction au travers de la pointe STM.

Lorsque la pointe STM est suffisamment éloignée de l'adsorbat le signal dI/dV est proportionnel à la densité d'états comme attendu avec la théorie de Tersoff et Hamann. Cependant si la pointe s'approche suffisamment près de l'adsorbat le signal ne reflète plus du tout la densité d'états. Au lieu d'un signal résonant il peut exister un creux dans le signal

près de l'énergie de la résonance. Nous avons montré que pour une orbitale de l'adsorbat de symétrie "s" la résonance est plus forte si l'adsorbat est en position hollow plutôt que en position top. Ceci est dû au fait que la résonance tend à être plus étroite en position hollow que en position top. Nous avons montré aussi que cet effet original disparaît sur un substrat métallique pour lequel la densité d'états plus forte du métal entraine une résonance plus large.

A notre connaissance cet effet n'a jamais été prédit ni observé. Les résonances sur le graphène pourraient être bien adaptées à l'observation de ce phénomène. Pour les adsorbats une difficulté pourrait être que dans le régime champ proche le courant au travers de l'adsorbat est suffisamment important pour chauffer le système ou produire un déplacement de l'adsorbat. De ce point de vue les résonances produites autour des lacunes pourraient être mieux adaptées à l'observation de ce phénomène. En effet la lacune est considérée comme une structure plus stable et ne devrait être ni détruite ni déplacée par la mesure STM.

Conclusion

Graphene is a one-atom thick layer of sp^2 bonded carbon atoms arranged in a honeycomb lattice which possesses unique electronic properties. The charge carriers in graphene are massless Dirac fermions and its unique electronic structure leads to a number of interesting physical effects, such as the minimal electrical conductivity, anomalous quantum Hall effect, Klein tunneling, the universal optical conductivity among others.

This thesis has focused on the electronic properties of two elementary structures at the nanoscale that are now produced by experimentalists. These two systems are rotated bilayers of graphene and graphene with resonant adsorbates such as Hydrogen atoms for example. For each system we have considered the problem of the electronic structure and of the description of some electronic transport properties.

Rotated bilayers of graphene have been discovered especially in graphene produced on Silicon Carbide. They present original properties when compared with standard AB bilayers that occur for example in graphite. It has been found that the main parameter is the rotation angle θ between the two layers, starting from a AA bilayer. When the angle θ is large (modulo 60°) the two layers appear electronically decoupled and this is now well understood. Yet when the angle diminishes a rich physics appears. In particular theoretical studies, prior to this one have, showed a renormalization of the velocity that increases when the angle decreases. For no too small angles ($\theta > 2-3°$) this phenomenon and can be described by a perturbative approach.

In the present work we have analyzed the density of states as a function of the position in the layer, still using a perturbative theory and therefore for not too small rotation angles.

We have shown that this density of states presents sinusodal oscillations with position which have the periodicity of the Moiré pattern of the bilayer. Interestingly the maximum of the density of states is found in the regions where the local arrangement of the two layers is of AA type. Therefore these modulations are precursors of the localization in the AA regions that is well identified at low angles ($\theta < 2^\circ$). The relative variation of the density at a given position is independent of energy close to the Dirac point and its amplitude varies inversely with the square of the angle θ . The analytical formula that we derived is in good quantitative agreement with fully numerical tight-binding calculations. The amplitude of the modulation of the density of states obtained by the theory is compatible with the signal observed in STM experiments. Yet the STM signal could also have a contribution coming from the ondulation of the graphene sheet. Indeed it is difficult to distinguish the distinction between a modulated signal coming from an ondulation of the plane or coming from a relative modulation of the density of states which is independent of the energy, as it is the case here. Therefore despite our efforts the physical origin of the Moiré observed in STM is not completely solved at present.

We discuss also the effect of disorder on electron lifetime and therefore on transport in rotated bilayers. More precisely a situation which is interesting is when disorder is absent (or negligible) in one plane and present in the other plane. The question is then how disorder in just one plane affects the transport of the bilayer. If the two layers were decoupled the plane with no (or very low) disorder would still have a very high conductivity dominating the conductivity of the bilayer. Yet electrons of the layers without defect will ultimately be scattered by defects of the other plane due to the coupling between the two layers. Therefore the conductivity of the bilayer is finite and dominated by the effect of

the interlayer coupling which itself depends on the angle θ .

A perturbative approach shows that for a given disorder in one plane the lifetime of electron in the other plane varies like the square of the angle θ. Starting from this estimation we can propose a simple formula for the conductivity of a rotated bilayer. We have compared this formula to essentially exact numerical calculations of transport. We found a good agreement.

Our results could be also of interest for multiwall nanotubes where a similar situation can occur. Here the external wall can be modified for example by chemical doping while the internal walls are protected and are essentially perfect. The overall conductivity can then be sensitive to the coupling between the external and internal walls . In the case of graphene bilayers the dominating parameter is the rotation angle θ between the two layers. For multiwall carbon nanotubes the equivalent parameter is the rotation between the chirality vectors of the different walls. Therefore from our study we expect that this parameter could play an essential role in the transport properties of multiwall nanotubes. Of course this analysis is in principle valid for nanotubes with sufficiently large diameters (several nanometers) and other parameters could play a role for nanotubes with smaller diameters.

We considered also in this thesis the role played by adsorbates like Hydrogen adatom on the graphene plane. A central characteristic of these adsorbates is that they are resonant scatterers for energies close to the Dirac point. Adsorbates not only can donate electrons or holes to graphene but also can play a role as defects, disrupting the lattice symmetry from which the unique properties of graphene such as the important pseudospin degree of freedom are derived. Graphene-like materials could be used in the fabrication of elec-

tronic and optoelectronic devices, gas sensors, biosensors, and batteries for energy storage. To enable many of these new technologies, it is necessary to understand and control the interaction of graphene with adsorbates.

Many studies in particular by ab-initio and by tight-binding methods have been proposed so far to study the charge transfer by resonant adsorbates. Here we started to develop a study based on a continuum model. This approach allows to study charge transfer and electrostatic potential as a function of the on-site energy of the orbital of the adsorbate and of its coupling with the graphene plane. We have presented our first results. Clearly this approach should be pursued to analyze in more detail the role of different parameters on charge transfer and potential around resonant adsorbates. Resonant adsorbates can be detected and studied experimentally in particular through scanning tunneling experiments (STM). As we showed their signature in an STM experiment should be peculiar. For this purpose we have used the formalism of the effective leads developped recently at Institut Nel. From this formalism we can derive a model that is particularly simple if one deals with the case of one conduction channel through the STM tip.

If the STM tip is sufficiently far from the adsorbate the signal dI/dV is proportional to the density of states of the resonances as expected from the Tersoff-Hamann theory. Yet if the tip is approached sufficiently close above the adsorbate the signal does not reflect anymore the resonant density of states. Instead of the resonant signal there can even exist a dip a the energy of the resonance. We showed that for s like orbital the resonance is stronger if the adsorbate is in a hollow position than if it is in a top position. This is due to the fact that resonances tend to be narrower in hollow position that in top position. We showed also that on a metallic substrate, where the higher density of states of the metal

leads to wider resonances, the original effect disappears.

To our knowledge this effect has never been predicted nor observed and resonances on graphene could be the well adapted to observe this phenomenon. For adsorbates an experimental difficulty could be that in the near field regime the current through the adsorbate is sufficiently important to heat the system or make the adatom move . In this respect resonances created by vacancies could be better suited to observe this effect. Indeed a vacancy should be a more stable structure not distroyed or displaced by the STM measurement.

APPENDICES

APPENDIX A

Perturbation Theory

In this Appendix, we set $\hbar = 1$. Here we propose to solve the wave equations (Schrödinger or Helmholtz) in the presence of Gaussian disorder. To this end, we address a method which describes the temporal evolution of a wave packet in random media. In the limit of weak disorder, which we will define properly, this expansion is expressed in the form of a series of *independent processes*, termed *collision events*, separated by a characteristic time τ_e called the *elastic collision time*. Associated with this is a characteristic length, the elastic mean free path, defined by $l_e = v\tau_e$ where v is the group velocity of the wave(for degenerate electrons, v is the Fermi velocity v_F. For waves , v is the group velocity, which we will denote by c). In order to evaluate the collision time τ_e for the case of the Schrödinger equation, we will use a representation in plane waves which correspond to the eigenstates $|\boldsymbol{k}\rangle$ of the free Hamiltonian [1]. We therefore interpret τ_e as the average lifetime of the states $|\boldsymbol{k}\rangle$. To estimate it in the presence of the potential V to lowest order in perturbation theory,we may use the *Fermi golden rule*[2]: the lifetime $\tau_{\boldsymbol{k}}$ of a state $|\boldsymbol{k}\rangle$

is given by

$$\frac{1}{\tau_{\boldsymbol{k}}} = 2\pi \sum_{\boldsymbol{k}'} |\langle \boldsymbol{k}|V|\boldsymbol{k}'\rangle|^2 \delta(\epsilon_{\boldsymbol{k}} - \epsilon_{\boldsymbol{k}'}) \ . \tag{A.1}$$

Taking for V the Gaussian disorder potential defined by ($\overline{V\boldsymbol{r}}$) and averaging over disorder, we obtain $\Omega\overline{|\langle \boldsymbol{k}|V|\boldsymbol{k}'\rangle|^2} = B(\boldsymbol{k} - \boldsymbol{k}')$ where $B(\boldsymbol{k} - \boldsymbol{k}')$ is the Fourier transform of the correlation function $\overline{V(\boldsymbol{r})V(\boldsymbol{r}')}$, where $\overline{\cdots}$ denotes the disorder average. τ_e is the volume of the system and the wave functions are normalized in this volume. The average lifetime τ_e of a state of energy ϵ is (we first show that $\frac{1}{\tau_e} = \frac{2\pi}{\Omega} \sum_{\boldsymbol{k}'} B(\boldsymbol{k} - \boldsymbol{k}')\delta(\epsilon_{\boldsymbol{k}} - \epsilon_{\boldsymbol{k}'})$) then:

$$\frac{1}{\tau_e} = 2\pi\rho_0\gamma_e \ . \tag{A.2}$$

where ρ_0 is the density of states per unit volume at the energy considered and where the parameter γ_e which characterizes the disorder is equal to

$$\gamma_e = \langle B(\boldsymbol{k} - \boldsymbol{k}')\rangle \ . \tag{A.3}$$

$\langle \cdots \rangle$ indicates the angular average of $B(\boldsymbol{k} - \boldsymbol{k}')$ with the constraint $\epsilon_{\boldsymbol{k}} = \epsilon_{\boldsymbol{k}'}$.

A.1 Green's Functions

The Fermi golden rule describes the temporal evolution of the system only for times less than τ_e. To go beyond this regime, we now introduce the Green function and the resolvant operator formalism.We will not seek to describe this formalism in all its generality, but we shall introduce several essential notions [Economou]. The cases of the Schrödinger

equation, which is first order in time, and the Helmholtz equation, which is second order, will be treated separately.

A.1.1 Green's Functions for the Schrödinger equation

Consider the Schrödinger equation with a potential V

$$i\frac{\partial\psi}{\partial t} = \mathcal{H}\psi = (\mathcal{H}_0 + V)\psi \ . \tag{A.4}$$

where $\mathcal{H}_0 = -(1/2m)\partial^2$ and V is the disorder potential. This describes free spinless electrons. The time evolution of a state $|\psi(t)\rangle$ initially in $|\psi(t = 0)\rangle$ is described by the unitary evolution operator $\mathcal{U}(t)$

$$|\psi(t)\rangle = \mathcal{U}(t)|\psi_0(0)\rangle = e^{-i\mathcal{H}t}|\psi_0(0)\rangle \ . \tag{A.5}$$

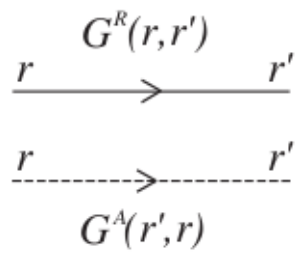

Figure A.1: Convention employed in this book for the representation of Greens functions. We take $\mathcal{G}^A(\boldsymbol{r'},\boldsymbol{r}) = \mathcal{G}^R(\boldsymbol{r},\boldsymbol{r'})^*$.

In spatial representation

$$\psi_f(\boldsymbol{r},t) = \langle\boldsymbol{r}|\psi_f(t)\rangle = \int d\boldsymbol{r}_i \, \langle\boldsymbol{r}|e^{-i\mathcal{H}t}\psi_0(\boldsymbol{r}_i,0)\boldsymbol{r}_i\rangle \ . \tag{A.6}$$

Following the convention of Figure B.1, the Green function is defined by

$$\mathcal{G}(\boldsymbol{r}_i, \boldsymbol{r}, t) = \langle \boldsymbol{r}| e^{-i\mathcal{H}t} |\boldsymbol{r}_i\rangle = \sum_n \phi_n^*(\boldsymbol{r}_i)\, \phi_n(\boldsymbol{r})\, e^{-i\epsilon_n t} \ . \tag{A.7}$$

where ϵ_n and ϕ_n are respectively the eigenenergies and the normalized eigenstates of $\mathcal{H}$. Thus defined, $\mathcal{G}(\boldsymbol{r}_i, \boldsymbol{r}, t)$ describes the evolution of a state $|\boldsymbol{r}_i\rangle$ at time $t = 0$ to the state $\boldsymbol{r}$ at a time t whose sign is not specified. If, on the other hand, we wish to describe the evolution of a state created at $t = 0$ to positive or negative times, we are led to define the operators

$$\hat{\mathcal{G}}^R(t) = -i\theta(t)\, e^{-i\mathcal{H}t} \ .$$

$$\hat{\mathcal{G}}^A(t) = i\theta(-t)\, e^{-i\mathcal{H}t} \ . \tag{A.8}$$

whose spatial representations correspond to retarded $\mathcal{G}^R$ and advanced $\mathcal{G}^A$ Greens functions

$$\mathcal{G}^R(\boldsymbol{r}_i, \boldsymbol{r}, t) = -i\theta(t)\, \langle \boldsymbol{r}| e^{-i\mathcal{H}t} |\boldsymbol{r}_i\rangle = -i\theta(t) \sum_n \phi_n^*(\boldsymbol{r}_i)\, \phi_n(\boldsymbol{r})\, e^{-i\epsilon_n t}$$

$$\mathcal{G}^A(\boldsymbol{r}_i, \boldsymbol{r}, t) = i\theta(-t)\, \langle \boldsymbol{r}| e^{-i\mathcal{H}t} |\boldsymbol{r}_i\rangle = i\theta(-t) \sum_n \phi_n^*(\boldsymbol{r}_i)\, \phi_n(\boldsymbol{r})\, e^{-i\epsilon_n t} \ . \tag{A.9}$$

The Fourier transforms

$$\mathcal{G}^{R,A}(\boldsymbol{r}_i, \boldsymbol{r}, \epsilon) = \int_{-\infty}^{\infty} dt\, e^{i\epsilon t}\, \mathcal{G}^{R,A}(\boldsymbol{r}_i, \boldsymbol{r}, t) \ . \tag{A.10}$$

are written as

$$\mathcal{G}^{R,A}(\boldsymbol{r}_i, \boldsymbol{r}, \epsilon) = \sum_n \frac{\phi_n^*(\boldsymbol{r}_i)\,\phi_n(\boldsymbol{r})}{\epsilon - \epsilon_n \pm i0} \ . \tag{A.11}$$

The convergence of the integrals (B.10) at long times necessitates the addition of an imaginary part to the energy $\epsilon \pm i0$, whose sign $\pm$ corresponds to the advanced and retarded parts, respectively. Equation (B.11) allows the formal introduction of operators which are the Fourier transforms of $\mathcal{G}^{R,A}(t)$:

$$\hat{\mathcal{G}}^{R,A}(\epsilon) = \frac{1}{\epsilon - \mathcal{H} \pm i0} \ . \tag{A.12}$$

Likewise, we define the free particle Green operators associated with the Hamiltonian $\mathcal{H}_0$

$$\hat{\mathcal{G}}_0^{R,A}(\epsilon) = \frac{1}{\epsilon - \mathcal{H} \pm i0} \ . \tag{A.13}$$

The Schrödinger equation (B.4) is therefore expressed as a relation between the operators $\hat{\mathcal{G}}$ and $\hat{\mathcal{G}}_0$. Multiplying by $\hat{\mathcal{G}}_0$ relation (B.12) written in the form

$$(\epsilon - \mathcal{H})\hat{\mathcal{G}} = \mathbb{1} \ , \tag{A.14}$$

and using (B.13) in the form $(\epsilon - \mathcal{H}_0)\hat{\mathcal{G}}_0 = \mathbb{1}$, we have

$$\hat{\mathcal{G}} = \hat{\mathcal{G}}_0 + \hat{\mathcal{G}}_0 V \hat{\mathcal{G}} \ , \tag{A.15}$$

which lends itself to the iterative expansion we will discuss in next sections.

A.1.2 Some properties of Green's functions

We introduced the Green function using the time evolution operator. It also measures the response to a pulse associated with the Schrödinger equation (B.4). Indeed, in the spatial representation, equation (B.12) is written

$$(\epsilon - \mathcal{H} \pm i0)\, \mathcal{G}^{R,A}(\boldsymbol{r}_i, \boldsymbol{r}, \epsilon) = \delta(\boldsymbol{r} - \boldsymbol{r}_i) \ . \tag{A.16}$$

and relation (B.15) between the operators $\hat{\mathcal{G}}$ and $\hat{\mathcal{G}}_0$ becomes

$$\mathcal{G}(\boldsymbol{r}_i, \boldsymbol{r}, \epsilon) = \mathcal{G}_0(\boldsymbol{r}_i, \boldsymbol{r}, \epsilon) + \int \mathcal{G}(\boldsymbol{r}_i, \boldsymbol{r}, \epsilon)\, V(\boldsymbol{r}')\, \mathcal{G}_0(\boldsymbol{r}', \boldsymbol{r}, \epsilon)\, d\boldsymbol{r}' \ . \tag{A.17}$$

Moreover, the Green function satisfies the following properties:

$$\mathcal{G}^A(\boldsymbol{r}, \boldsymbol{r}_i, \epsilon) = \mathcal{G}^R(\boldsymbol{r}_i, \boldsymbol{r}, \epsilon)^* \ . \tag{A.18}$$

and

$$\mathcal{G}^A(\boldsymbol{r}, \boldsymbol{r}_i, -t) = \mathcal{G}^R(\boldsymbol{r}_i, \boldsymbol{r}, t)^* \ . \tag{A.19}$$

where * indicates the complex conjugates. We also define the imaginary part of $\hat{\mathcal{G}}^R$ by

$$\Im \hat{\mathcal{G}}^R = \frac{\hat{\mathcal{G}}^R - \hat{\mathcal{G}}^A}{2i} \ . \tag{A.20}$$

We should notice that we use the notation:

$$\Im \mathcal{G}^R(\boldsymbol{r}, \boldsymbol{r}') = \langle \boldsymbol{r}' | \Im \hat{\mathcal{G}}^R | \boldsymbol{r} \rangle = \frac{\mathcal{G}^R(\boldsymbol{r}, \boldsymbol{r}') - \mathcal{G}^A(\boldsymbol{r}, \boldsymbol{r}')}{2i} \ . \tag{A.21}$$

and not

$$\Im\mathcal{G}^R(\boldsymbol{r},\boldsymbol{r}') = \frac{\mathcal{G}^R(\boldsymbol{r},\boldsymbol{r}') - \mathcal{G}^A(\boldsymbol{r},\boldsymbol{r}')^*}{2i} = \frac{\mathcal{G}^R(\boldsymbol{r},\boldsymbol{r}') - \mathcal{G}^A(\boldsymbol{r}',\boldsymbol{r})}{2i} \ . \tag{A.22}$$

A.1.3 Green's function and density of states

All information about the solutions of the Schrdinger equation is contained in the Green function. In particular, it is related to the density of states $\nu(\epsilon)$ defined by

$$\nu(\epsilon) = \sum_n \delta(\epsilon - \epsilon_n) \ . \tag{A.23}$$

We shall also use the density of states per unit volume, denoted $\rho(\epsilon) = \frac{\nu(\epsilon)}{\Omega}$. It is also convenient to define the following.

♣ The local density of states at a point $\boldsymbol{r}$

$$\rho_\epsilon(\boldsymbol{r}) = \rho(\boldsymbol{r},\epsilon) = \sum_n |\phi_n(\boldsymbol{r})|^2 \, \delta(\epsilon - \epsilon_n) \ , \tag{A.24}$$

♣ The non-local density of states

$$\rho_\epsilon(\boldsymbol{r},\boldsymbol{r}') = \rho(\boldsymbol{r},\boldsymbol{r}',\epsilon) = \sum_n \phi_n^*(\boldsymbol{r})\phi_n(\boldsymbol{r}') \, \delta(\epsilon - \epsilon_n) \ , \tag{A.25}$$

Starting rom equation (B.11), the expression

$$\frac{1}{x+i0} = pp\frac{1}{x} - i\pi\delta(x) \ , \tag{A.26}$$

then we can do

$$\rho_\epsilon(\boldsymbol{r},\boldsymbol{r}') = -\frac{1}{\pi}\Im\mathcal{G}^R(\boldsymbol{r},\boldsymbol{r}',\epsilon) = -\frac{1}{\pi}\langle\boldsymbol{r}'|\Im\hat{\mathcal{G}}^R|\boldsymbol{r}\rangle = \frac{i}{\pi}\Big[\mathcal{G}^R(\boldsymbol{r},\boldsymbol{r}',\epsilon) - \mathcal{G}^A(\boldsymbol{r},\boldsymbol{r}',\epsilon)\Big] \ , \tag{A.27}$$

as well as

$$\rho_\epsilon(\boldsymbol{r}) = -\frac{1}{\pi}\Im\mathcal{G}^R(\boldsymbol{r},\boldsymbol{r},\epsilon) \ , \tag{A.28}$$

and to obtain the density of states per unit volume in the form

$$\rho(\epsilon) = \frac{\nu(\epsilon)}{\Omega} = -\frac{1}{\pi\Omega}\Im\int d\boldsymbol{r}\,\mathcal{G}^R(\boldsymbol{r},\boldsymbol{r}',\epsilon) \ , \tag{A.29}$$

Thus $\rho_\epsilon(\boldsymbol{r})$ and $\rho_\epsilon(\boldsymbol{r},\boldsymbol{r})$ is the spatial average of $\rho_\epsilon(\boldsymbol{r})$

We can also introduce the Green function in momentum representation

$$\mathcal{G}^{R,A}(\boldsymbol{k_i},\boldsymbol{k},\epsilon) = \langle\boldsymbol{k}|\hat{\mathcal{G}}^{R,A}|\boldsymbol{k}_i\rangle \ . \tag{A.30}$$

Translation invariance, when it exists, implies the $\mathcal{G}(\boldsymbol{r_i},\boldsymbol{r},\epsilon) = \mathcal{G}(\boldsymbol{r}-\boldsymbol{r}_i,\epsilon)$. In this case, $\mathcal{G}^{R,A}(\boldsymbol{k_i},\boldsymbol{k},\epsilon) = \mathcal{G}^{R,A}(\boldsymbol{k},\epsilon)\delta_{\boldsymbol{k},\boldsymbol{k}_i}$, with

$$\mathcal{G}^{R,A}(\boldsymbol{k},\epsilon) = \int \mathcal{G}^{R,A}(\boldsymbol{r},\epsilon)\,e^{-i\boldsymbol{k}\cdot\boldsymbol{r}}d\boldsymbol{r} \ . \tag{A.31}$$

and the density of states per unit volume may be written as

$$\rho(\epsilon) = -\frac{1}{\pi\Omega}\sum_{\boldsymbol{k}} \Im\mathcal{G}^R(\boldsymbol{k},\epsilon) \ , \tag{A.32}$$

We see that this expression is analogous to (B.29). The density of states does not depend on the representation under consideration. More generally, we may write

$$\nu = -\frac{1}{\pi}\Im\hat{\mathcal{G}}^R \ , \tag{A.33}$$

A.2 Multiple scattering expansion

A.2.1 Dyson equation

We now seek to construct a perturbative expansion starting from equation (B.15) connecting $\hat{\mathcal{G}}$ and $\hat{\mathcal{G}}_0$. Formally, we may write this expansion as [Mahan and Fetter's books]

$$\hat{\mathcal{G}} = \hat{\mathcal{G}}_0 + \hat{\mathcal{G}}_0 V\hat{\mathcal{G}}_0 + \hat{\mathcal{G}}_0 V\hat{\mathcal{G}}_0 V\hat{\mathcal{G}}_0 + \cdots \ , \tag{A.34}$$

In spatial representation this is

$$\begin{aligned}\mathcal{G}(\boldsymbol{r},\boldsymbol{r}') = \mathcal{G}_0(\boldsymbol{r},\boldsymbol{r}') &+ \int d\boldsymbol{r_1}\mathcal{G}_0(\boldsymbol{r},\boldsymbol{r_1})V(\boldsymbol{r_1})\mathcal{G}_0(\boldsymbol{r_1},\boldsymbol{r}') \\ &+ \int d\boldsymbol{r_1}d\boldsymbol{r_2}\mathcal{G}_0(\boldsymbol{r},\boldsymbol{r_1})V(\boldsymbol{r_1})\mathcal{G}_0(\boldsymbol{r_1},\boldsymbol{r_2})V(\boldsymbol{r_2})\mathcal{G}_0(\boldsymbol{r_2},\boldsymbol{r}') \\ &+ \int d\boldsymbol{r_1}d\boldsymbol{r_2}d\boldsymbol{r_3}\mathcal{G}_0(\boldsymbol{r},\boldsymbol{r_1})V(\boldsymbol{r_1})\mathcal{G}_0(\boldsymbol{r_1},\boldsymbol{r_2})V(\boldsymbol{r_2})\mathcal{G}_0(\boldsymbol{r_2},\boldsymbol{r_3})V(\boldsymbol{r_3})\mathcal{G}_0(\boldsymbol{r_3},\boldsymbol{r}') \\ &+ \cdots \ .\end{aligned} \tag{A.35}$$

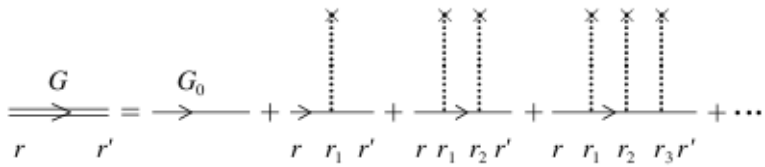

Figure A.2: Diagrammatic expansion of the Green function before averaging over disorder[From [1]] .

This expansion may be expressed pictorially as in Figure B.2. Upon averaging over disorder and using the particular form of the Gaussian potential, the expansion of the average Green function $\overline{\mathcal{G}}$ simplifies considerably. The term linear in V and all other odd power terms vanish, while the quadratic term yields the correlation function $B(\boldsymbol{r_1} - \boldsymbol{r_2})$, leaving us with [1]

$$\overline{\mathcal{G}}(\boldsymbol{r}, \boldsymbol{r'}) = \mathcal{G}_0(\boldsymbol{r}, \boldsymbol{r'}) + \int d\boldsymbol{r_1} d\boldsymbol{r_2} B(\boldsymbol{r_1} - \boldsymbol{r_2}) \mathcal{G}_0(\boldsymbol{r}, \boldsymbol{r_1}) \mathcal{G}_0(\boldsymbol{r_1}, \boldsymbol{r_2}) \mathcal{G}_0(\boldsymbol{r_2}, \boldsymbol{r'}) + \cdots \ . \tag{A.36}$$

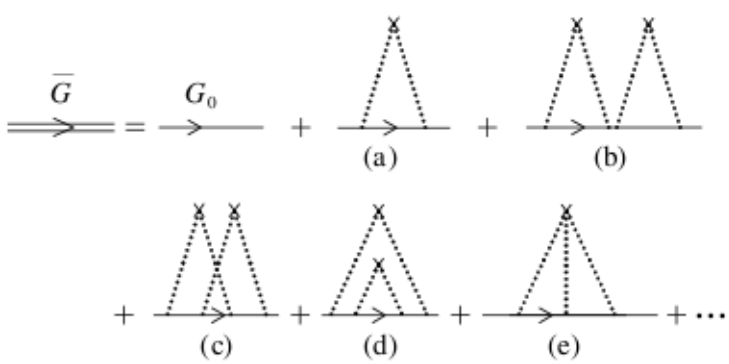

Figure A.3: Diagrammatic expansion of the average Green function. From [1] .

This expansion is represented in Figure B.3, where the pairings of impurity lines represent the different products $\overline{V(\mathbf{r}_i)V(\mathbf{r}_j)}$. Upon averaging over disorder, translational invariance is recovered, and the Green function depends only on the difference in position: $\overline{\mathcal{G}}(\boldsymbol{r}, \boldsymbol{r}') = \overline{\mathcal{G}}(\boldsymbol{r} - \boldsymbol{r}')$. The Fourier transform of (B.36) is of the form

$$\overline{\mathcal{G}}(\boldsymbol{k}) = \mathcal{G}_0(\boldsymbol{k}) + \frac{1}{\Omega}\sum_{\boldsymbol{q}} B(\boldsymbol{q})\mathcal{G}_0(\boldsymbol{k})\mathcal{G}_0(\boldsymbol{k}-\boldsymbol{q})\mathcal{G}_0(\boldsymbol{k}) + \cdots \ . \tag{A.37}$$

Upon averaging, we generate all the diagrams corresponding to all possible pairings of interaction lines with the impurities which appear in Figure B.2. These diagrams are of two types (Figure B.3). The first are called separable or reducible, that is, they may be separated into two diagrams without cutting an impurity line. All other diagrams are called irreducible. The reducible diagrams may be factorized into a product of irreducible diagrams. This is possible because the integrals over the intermediate wave vectors are independent. For example, diagram (b) of Figure B.3 may be written

$$\begin{aligned}\frac{1}{\Omega^2}\sum_{\boldsymbol{q}}\sum_{\boldsymbol{q}'} &\mathcal{G}_0(\boldsymbol{k})B(\mathbf{q})\mathcal{G}_0(\boldsymbol{k}-\boldsymbol{q})\mathcal{G}_0(\boldsymbol{k})\mathcal{G}_0(\boldsymbol{k})B(\mathbf{q}')\mathcal{G}_0(\boldsymbol{k}-\boldsymbol{q}')\mathcal{G}_0(\boldsymbol{k}) \\ &= \mathcal{G}_0(\boldsymbol{k})\left[\sum_{\boldsymbol{q}}\frac{B(\boldsymbol{q})}{\Omega}\mathcal{G}_0(\boldsymbol{k}-\boldsymbol{q})\mathcal{G}_0(\boldsymbol{k})\right]^2 \ .\end{aligned} \tag{A.38}$$

The sum of the contributions of all the diagrams reduces to the calculation of the geometric series

$$\overline{\mathcal{G}}(\boldsymbol{k},\epsilon) = \mathcal{G}_0(\boldsymbol{k},\epsilon) + \mathcal{G}_0(\boldsymbol{k},\epsilon)\sum_{n=1}^{\infty}\left[\Sigma(\boldsymbol{k},\epsilon)\mathcal{G}_0(\boldsymbol{k},\epsilon)\right]^n \ . \tag{A.39}$$

The function $\Sigma(\boldsymbol{k},\epsilon)$, called the *self-energy*, is by construction the sum over an infinity

of irreducible diagrams (Figure B.4).

For the Schrödinger equation, the free Green function $\mathcal{G}_0(\boldsymbol{k},\epsilon)$ is given by $\mathcal{G}_0^{R,A}(\boldsymbol{k},\epsilon) = \dfrac{1}{\epsilon - \epsilon(\boldsymbol{k}) \pm i0}$. The corresponding Dyson equation (B.39) may be written in the form

$$\overline{\mathcal{G}}^{R,A}(\boldsymbol{k},\epsilon) = \frac{1}{\epsilon - \epsilon(\boldsymbol{k}) - \Sigma^{R,A}(\boldsymbol{k},\epsilon)} \ . \tag{A.40}$$

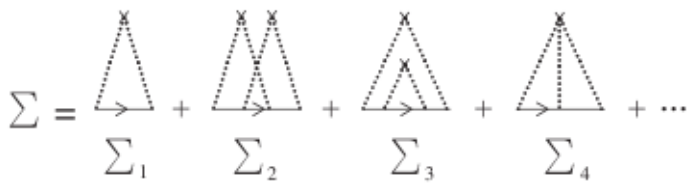

Figure A.4: Diagrammatic expansion of the self-energy as a sum of irreducible diagrams . From [1] .

A.2.2 Self-Energy

The calculation of the self-energy is in principle a difficult problem since it contains an infinite number of terms. The first, ${\Sigma_1}^{R,A}(\boldsymbol{k},\epsilon)$, may be written as (Figure B.4)

$$\Sigma_1^{R,A}(\boldsymbol{k},\epsilon) = \frac{1}{\Omega}\sum_{k'} B(\boldsymbol{k}-\boldsymbol{k}')\mathcal{G}_0^{R,A}(\boldsymbol{k}') \ . \tag{A.41}$$

The real part of the self-energy gives an unimportant shift of the zero of energies (or of frequencies for the Helmholtz equation) and will not be considered further. In the Schrödinger case, equation (B.33) which relates the Green function to the density of states leads to

$$\Im\Sigma_1^{R,A}(\boldsymbol{k},\epsilon) = -\frac{\pi}{\Omega}\sum_{k'} B(\boldsymbol{k}-\boldsymbol{k}')\delta(\epsilon-\epsilon(\boldsymbol{k}')) \ . \tag{A.42}$$

Denoting $\boldsymbol{k} = k\hat{\mathbf{e}}$ where $\hat{\mathbf{e}}$ is a unit vector, and separating the radial and angular summations, we get

$$\Im\Sigma_1^{R,A}(\boldsymbol{k},\epsilon) = -\pi\rho_0(\epsilon)\,\langle B(k,\hat{\mathbf{e}}-\hat{\mathbf{e}}')\rangle \ . \tag{A.43}$$

where we have used the angular average $\langle\cdots\rangle$ of B and the relation $k = \sqrt{2m\epsilon}$.

The self-energy defines a characteristic time τ_e called the *elastic collision time* such that

$$\frac{1}{2\tau_e} = -\Im\Sigma_1^{R,A}(\boldsymbol{k},\epsilon) = \pi\rho_0(\epsilon)\,\gamma_e \qquad \textbf{Schrödinger} \tag{A.44}$$

where

$$\gamma_e = \langle B(\boldsymbol{k}-\boldsymbol{k}')\rangle \tag{A.45}$$

This time, which has already been obtained using the Fermi golden rule (B.2), is the average lifetime of an eigenstate of wave vector $\boldsymbol{k}$ and energy ϵ. Within the Gaussian model it is independent of the wave vector. The existence of a finite imaginary part for the self-energy implies that the density of states, proportional to the imaginary part of the Green function (relation B.29), appears as a series of Lorentzians each of which describes an energy eigenstate with a broadening $\frac{1}{2\tau_e}$.

Bibliography

[1] Eric Akkermans, Gilles Montambaux.: *Mesoscopic Physics of Electrons and Photons*; Cambridge University (2007)

[2] Alexander L. Fetter.: *Quantum Theory of Many-Particle Systems*, Dover Books on Physics, (2003)

APPENDIX B

Calculation of LDOS and Self-energy of twisted Bilayer Graphene

B.1 Tight-Binding Model and Hamiltonian

In this appendix we rewrite all calculations in Chapter 2 and do supplementary derivations. We start calculations from equation 2.18

$$H_c|\varepsilon\,\vec{k}\rangle_+ = \sum_i t(\varepsilon_i\,\vec{k}_i\,,\varepsilon\,\vec{k})\;|\varepsilon_i\,\vec{k}_i\rangle_- \tag{B.1}$$

Where $t(\varepsilon_i\,\vec{k}_i\,,\varepsilon\,\vec{k})\,\vec{k}_i \equiv t_i$ is the transfer matrix. Which means that coupling Hamiltonian H_c it couples the upper state $|\varepsilon\,\vec{k}\rangle_+$ to lower state $|\varepsilon\,\vec{k}\rangle_-$, by applying of the transfer matrix t_i

By multiplying of ${}_-\langle\varepsilon'\,\vec{k'}|$ to left-side of equation B.1 and using of orthonormality property we find:

$$_{-}\langle \varepsilon' \vec{k}' | H_c | \varepsilon \vec{k} \rangle_{+} = \sum_i t(\varepsilon_i \vec{k}_i , \varepsilon \vec{k}) \; _{-}\langle \varepsilon' \vec{k}' | \varepsilon_i \vec{k}_i \rangle_{-}$$

$$_{-}\langle \varepsilon' \vec{k}' | \varepsilon_i \vec{k}_i \rangle_{-} = \delta_{\varepsilon_i, \varepsilon'} \sum_{\vec{R}} e^{i(\vec{k}_i - \vec{k}') \cdot \vec{R}'} = \delta_{\varepsilon_i, \varepsilon'} \frac{4\pi^2}{S} \sum_{\vec{K}'_r} \delta(\vec{K}' - \vec{k}_i - \vec{K}'_r)$$

$\Rightarrow$

$$H_c(\vec{k}' \varepsilon' ; \vec{k} \varepsilon) = \sum_i t_i \; \delta_{\varepsilon_i, \varepsilon'} \; \frac{4\pi^2}{S} \sum_{\vec{K}'_r} \delta(\vec{K}' - \vec{k}_i - \vec{K}'_r) \tag{B.2}$$

Finally for $\vec{k}_i = \vec{k} + \vec{K}_r = \vec{k}'(mod \;\; \vec{K}'_r)$ we have:

$$t_i(\vec{k} + \vec{K}_r) = \frac{4\pi^2}{S} H_c(\vec{k} + \vec{K}_r) \;\; e^{i(\vec{k} + \vec{K}_r) \cdot (\eta' \vec{u}' - \eta \vec{u} + \vec{\Delta})} \tag{B.3}$$

We are interested to calculate numerical value of coupling hamiltonian:

$$eq : couplingHamiltonianH_c(\vec{k} + \vec{K}_r) \equiv H_c(|\vec{k} + \vec{K}_r|) \tag{B.4}$$

$\vec{k} = \vec{K}_d + \delta \vec{k} \;\; and \;\; \|\delta \vec{k}\| \ll \|\vec{K}_d\| , \|\vec{K}_r\| \;\; \Rightarrow$

$$H_c(\vec{k} + \vec{K}_r) \sim \; H_c(|\vec{K}_d + \vec{K}_r|)$$

The smallest modulus of $|\vec{K}_d + \vec{K}_r|$, is the $|\vec{K}_d|$ which its modulus is:

$$|\vec{K}_d| = \frac{4\pi}{3a_0}$$

then by substituing the modulus of the transmission matrix is the:

$$t_i \cong \frac{4\pi^2}{S} H_c(|\vec{K}_d|) \cong 0.12\, eV \tag{B.5}$$

Now we shall adopt following approximation:

$$t_i \cong \frac{4\pi^2}{S} H_c(|\vec{k} + \vec{K}_r|) \cong \frac{4\pi^2}{S} H_c(|\vec{K}_d|) \cong 0.12\, eV$$

or

$$t_i = 0 \qquad if \qquad |\vec{K}_d + \vec{K}_r| > |\vec{K}_d|$$

There are only three possibilities for $\vec{K}_r$ which are :

$$\vec{K}_r = \begin{cases} 0 \\ \vec{K}_{d_+} - \vec{K}_{d_0} \\ \vec{K}_{d_-} - \vec{K}_{d_0} \end{cases} \tag{B.6}$$

or in a compact we can say:

$$\vec{K}_r = \vec{K}_{d_\varepsilon} - \vec{K}_{d_0} \quad ; \quad \varepsilon = -1, 0, 1 \tag{B.7}$$

B.2 Effective Hamiltonian:

The effective Hamiltonian of rotated-bliayer grapheme in general for can be written as:

$$H_{eff} = H_0(z) + \sum_{j=1}^{6} H_{\vec{G}} \;\; e^{i\vec{G}_j \cdot \vec{r}} \tag{B.8}$$

where

$H_0(z)$: Is homogeneous and no variation of DOS that gives self-energy and normalized velocity .

$\sum_{j=1}^{6} H_{\vec{G}} \;\; e^{i\vec{G}_j \cdot \vec{r}}$: Gives moiré pattern and variation of DOS

$$H_{eff} = H_+ + \widetilde{\Sigma}_+ \tag{B.9}$$

where $\widetilde{\Sigma}_+$ is the self-energy:

$$\widetilde{\Sigma}_+ = H_c \frac{1}{z - H_-} H_c$$

Now we apply the last equation to $|\varepsilon \vec{k}\rangle_+$ then we have

$$\widetilde{\Sigma}_+ |\varepsilon \vec{k}\rangle_+ = H_c \frac{1}{z - H_-} H_c |\varepsilon \vec{k}\rangle_+$$

from equation B.1 we can write:

$$\widetilde{\Sigma}_+|\varepsilon\,\vec{k}\rangle_+ = H_c \frac{1}{z - H_-} \sum_{\vec{K}_i,\,\varepsilon_i} t(\varepsilon_i,\ \vec{K}_i + \vec{k}\,;\varepsilon\,,\vec{k})\ |\varepsilon_i,\ \vec{K}_i + \vec{k}\rangle_-$$

$$\frac{1}{z - H_-}|\varepsilon_i,\ \vec{k}_i + \vec{k}\rangle_- = \sum_{\varepsilon_j} G_-(z,\, j\,\vec{k} + \vec{K}_i,\ i\,\vec{k} + \vec{K}_i|\varepsilon_i,\ \vec{K}_j + \vec{k}\rangle$$

$\Rightarrow$

$$\widetilde{\Sigma}_+|\varepsilon\,\vec{k}\rangle_+ = H_c \sum_{\varepsilon_j,\varepsilon_j,\vec{K}_i} t(\varepsilon_i,\ \vec{K}_i + \vec{k}\,;\varepsilon\,,\vec{k})\, G_-(z;\varepsilon_j,\ \vec{k} + \vec{K}_i;\ \varepsilon_i\,\vec{k} + \vec{K}_i)|\varepsilon_i,\ \vec{K}_j + \vec{k}\rangle \qquad \text{(B.10)}$$

Now we want to calculate $H_c|\varepsilon_j\,,\ \vec{k} + \vec{K}_r\rangle$: This vector will be coupled to vector of the form $\vec{k} + \vec{K}_r + \vec{K}'_r$ Where $\vec{K}'_r$ is a vector of the reciprocal lattice of the lower plane - This means that the self-energy couples a state $|\vec{k}\rangle$ to the state $|\vec{k} + \vec{K}_+ + \vec{K}_-\rangle$, where $\vec{K}_+$ and $\vec{K}_-$ are vectors of the reciprocal lattice of the planes + and -

$\vec{K}_+ + \vec{K}_-$ belongs to the reciprocal lattice of the moir structure: $\vec{K}_r + \vec{K}'_r = \vec{G}$

One has to compute matrix elements from plane - to plane + :

$$\vec{R}' = \vec{\Delta} + \mathcal{R}_\theta(\vec{R}) \quad \text{and} \quad \mathcal{R}_\theta(\vec{R}) = \vec{R}' - \vec{\Delta}$$

by applying of $\mathcal{R}_{-\theta}$ to left-side of above equation we have:

$$\mathcal{R}_{-\theta}\,\mathcal{R}_\theta(\vec{R}) = \mathcal{R}_{-\theta}(\vec{R}') - \mathcal{R}_{-\theta}\vec{\Delta}$$

Finally we have:

$$\vec{R} = \mathcal{R}_{-\theta}(\vec{R'}) - \mathcal{R}_{-\theta}\,\vec{\Delta} \tag{B.11}$$

we want to calculate following term:

$$e^{i(\vec{k}+\vec{K_r}+\vec{K'_r})\cdot(\eta'\,\vec{u'}-\eta\,\vec{u}-\mathcal{R}_{-\theta}\,\vec{\Delta})} \times H_c(\vec{k}+\vec{K_r}+\vec{K'_r})$$

$$= e^{i(\vec{k}+\vec{K_r})\cdot\vec{\Delta}}\; e^{-i(\vec{k}+\vec{K_r}+\vec{K'_r})\cdot\mathcal{R}_{-\theta}\,\vec{\Delta}} \times H_c(\vec{k}+\vec{K_r}+\vec{K'_r})$$

$$e^{i(\vec{k}+\vec{K_r})\cdot\vec{\Delta}}\; e^{-i(\vec{k}+\vec{K_r}+\vec{K'_r})\cdot\mathcal{R}_{-\theta}\,\vec{\Delta}} = e^{i(\vec{k}+\vec{K_r})\cdot(\vec{\Delta}-\mathcal{R}_{-\theta}\,\vec{\Delta})}\; e^{-i\vec{K'_r}\cdot\mathcal{R}_{-\theta}\,\vec{\Delta}}$$

If $\vec{K'_r} = 0$ then:

$$e^{i(\vec{k}+\vec{K_r})\cdot(\vec{\Delta}-\mathcal{R}_{-\theta}\,\vec{\Delta})} \approxeq 1$$

Because θ weakes and $||\vec{\Delta}|| < a_0$

There is no dependence of $\vec{\Delta}$ for $|vecK'_r = 0$ i.e for coupling between $\vec{k} \equiv \vec{R}$

We can say that:

$\widetilde{\Sigma}_{\vec{G}=0}$ is independent of $\vec{\Delta}$

$\widetilde{\Sigma}_{\vec{G}\neq 0}$ is dependent of $\vec{\Delta}\ \sim\ e^{-i\vec{K'_r}\cdot\vec{\Delta}}$

For small angles

$$\simeq e^{+i\vec{K_{r_+}}\cdot\vec{\Delta}}$$

Because $||\vec{G}|| = ||\vec{K_{r_+}} + \vec{K_{r_-}}|| \ll ||\vec{K_r}||$

Now we can establish coupling Matrix as following:

$$T = t\ e^{i(\vec{k}+\vec{K}_r)\cdot\vec{\Delta}} \begin{pmatrix} 1 & e^{i(\vec{k}+\vec{K}_r)\cdot(-\eta\,\vec{u'})} \\ e^{i(\vec{k}+\vec{K}_r)\cdot(\eta'\,\vec{u'})} & e^{i(\vec{k}+\vec{K}_r)\cdot(\eta'\,\vec{u'}-\eta\,\vec{u'})} \end{pmatrix} \tag{B.12}$$

$$e^{i(\vec{k}+\vec{K}_r)\cdot(\eta'\,\vec{u'}-\eta\,\vec{u'})} \approx 1$$

$$T \approx t\ e^{i(\vec{K}_d+\vec{K}_r)\cdot\vec{\Delta}} \begin{pmatrix} 1 & e^{i(\vec{K}_d+\vec{K}_r)\cdot(-\vec{u})} \\ e^{i(\vec{K}_d+\vec{K}_r)\cdot(\vec{u'})} & 1 \end{pmatrix} \approx t \begin{pmatrix} 1 & e^{-i\vec{K}\cdot\vec{u}} \\ e^{i\vec{K}\cdot\vec{u'}} & 1 \end{pmatrix} \tag{B.13}$$

B.3 Self-Energy

Now we introduce two simple matrices with their algebraic properties:

$$M(\alpha) = \begin{pmatrix} 0 & e^{i\alpha} \\ e^{-i\alpha} & 0 \end{pmatrix} \quad ; \quad N(\beta) = \begin{pmatrix} e^{i\beta} & 0 \\ 0 & e^{-i\beta} \end{pmatrix} \tag{B.14}$$

Easily we can show:

$$M(\alpha)\,N(\beta) = \begin{pmatrix} 0 & e^{i(\alpha-\beta)} \\ e^{-i(\alpha-\beta)} & 0 \end{pmatrix} = M(\alpha-\beta) \quad ; \quad N(\beta)\,M(\alpha) = M(\alpha+\beta) \tag{B.15}$$

We are very interested to calculate self-energy $\widetilde{\Sigma}$ for $\vec{G} = 0$:

$$\widetilde{\Sigma}_0(z) = \sum_{\vec{K}_r} T_+(\vec{K}_r)\ \mathcal{G}_0^-\ (\vec{K}_d + \vec{K}_r)\ T_-(\vec{K}_r) \tag{B.16}$$

By combining of equations (2.38) and (2.40) we have:

$$T(\theta_\nu) = t\ [1 + M(\theta_\nu)] \quad ;\ M(\theta_\nu) = \begin{pmatrix} 0 & e^{i\theta_\nu} \\ e^{-i\theta_\nu} & 0 \end{pmatrix} \tag{B.17}$$

$$\mathcal{G}_0^-\ (z, \theta\,\vec{\zeta} \times\ \vec{K}_\mu) = \frac{1}{z - H_-(\theta\,\vec{\zeta} \times\ \vec{K}_\mu)} \tag{B.18}$$

and for the Hamiltonian:

$$H_-(\theta\,\vec{\zeta} \times\ \vec{K}_\mu) = \begin{pmatrix} -\gamma_1\, g(\theta\,\vec{\zeta} \times\ \vec{K}_\mu) + \frac{\Delta}{2} & -f\ (\theta\,\vec{\zeta} \times\ \vec{K}_\mu) \\ -f^*\ (\theta\,\vec{\zeta} \times\ \vec{K}_\mu) & -\gamma_1\, g(\theta\,\vec{\zeta} \times\ \vec{K}_\mu) - \frac{\Delta}{2} \end{pmatrix} \tag{B.19}$$

Where Δ is potential difference between two layers, $g = \frac{1}{\gamma_0}(|f/\gamma_0|^2 - 3)$ [54]and:

$$f\ (\theta\,\vec{\zeta} \times\ \vec{K}_\mu) = |f\ (\theta\,\vec{\zeta} \times\ \vec{K}_\mu)|\ e^{i(\theta_\mu + \frac{\pi}{2}\,\varepsilon_\theta\,)}\ e^{i\alpha_-(\theta)} \tag{B.20}$$

where:

$$|f\ (\theta\,\vec{\zeta} \times\ \vec{K}_\mu)| = \left|\gamma_0 e^{i\,\frac{2\pi}{\sqrt{3}}\theta}\left(1 - e^{-i\,\frac{2\pi}{\sqrt{3}}\theta}\right)\right| = 2\gamma_0 \sin\frac{\pi\theta}{\sqrt{3}} \tag{B.21}$$

So we can analyze our last formula for Hamiltonian:

$$H\,(\theta\vec{\zeta}\times\vec{K_\mu}) = [g_-(\theta) \pm \frac{\Delta}{2}]\,\mathbf{I} + |f\,(\theta\vec{\zeta}\times\vec{K_\mu})| \begin{pmatrix} 0 & e^{i\alpha_-(\theta)}\,e^{i\theta_\mu}\,e^{i\frac{\pi}{2}\varepsilon_\theta} \\ e^{-i\alpha_-(\theta)}\,e^{-i\theta_\mu}\,e^{-i\frac{\pi}{2}\varepsilon_\theta} & 0 \end{pmatrix}$$

where $e^{-i\frac{\pi}{2}\varepsilon_\theta} = i \;or\; -i = \varepsilon_\theta\, i$

$$\Rightarrow\; H\,(\theta\vec{\zeta}\times\vec{K_\mu}) = [g_-(\theta) \pm \frac{\Delta}{2}]\,\mathbf{I} + f_-\,(\theta)\;N(\alpha_-(\theta) + \frac{\pi}{2})\;M(\theta_\mu)$$

Therefore for Green's function we have:

$$\mathcal{G}_0^-\,(E,\theta\vec{\zeta}\times\vec{K_\mu}) = \frac{1}{det(z-H_-)}\left[\left(z - g_-(\theta) \pm \frac{\Delta}{2}\right)\mathbf{I} + f_-(\theta)\,N\left(\alpha_-(\theta) + \frac{\pi}{2}\right)\;M(\theta_\mu)\right] \quad \text{(B.22)}$$

Now we continue our calculations for self-energy (2.43) and by relation (2.47) :

$$\widetilde{\Sigma}_0(z) = \sum_\mu T(\mu)\;\mathcal{G}_0^-(z,\mu)\;\;T(\mu) =$$

$$\sum_\mu t\;[1 + M(\theta_\mu)]\;\;\frac{1}{det(z-H_-)}\left[\left(z - g_-(\theta) \pm \frac{\Delta}{2}\right)\mathbf{I} + f_-(\theta)\,N\left(\alpha_-(\theta) + \frac{\pi}{2}\right)\;M(\theta_\mu)\right]$$

$$= \frac{t^2}{det(z-H_-)}\sum_\mu\Big([1 + M(\theta_\mu)]\;\left[A_-(z,\theta,\Delta)\mathbf{I} + f_-(\theta)N\;M(\theta_\mu)\right]\;[1 + M(\theta_\mu)]\Big) \text{ where } A_-(z,\theta,\Delta) = z - g_-(\theta) \pm \tfrac{\Delta}{2}$$

$$\Rightarrow$$

$$\widetilde{\Sigma}_0(z) = \overbrace{\frac{t^2}{det(z-H_-)}A_-\;\sum_\mu\Big([1 + M(\theta_\mu)]\;[1 + M(\theta_\mu)]\Big)}^{\widetilde{\Sigma}_0^1(z)}$$

$$+\underbrace{\frac{t^2}{det(z-H_-)} f_-(\theta) \sum_{\mu} \Big([1+M(\theta_\mu)]\ N\ M(\theta_\mu)\ [1+M(\theta_\mu)]\Big)}_{\widetilde{\Sigma}_0^2(z)}$$

From equation (2.40) it is clear that: $M^2(\theta) = 1$; then we are going to calculate the terms $\widetilde{\Sigma}_0^1(z)$ and $\widetilde{\Sigma}_0^2(z)$:

$\widetilde{\Sigma}_0^1(z): \quad \mathbf{I} + M(\theta_\mu) + M(\theta_\mu) + M^2(\theta_\mu) = 2\,\mathbf{I} + 2\,M(\theta_\mu)$ and $\theta_\mu = -\frac{2\pi}{3}, 0, \frac{2\pi}{3}$ then:

$\sum_{\mu=1}^{3} M(\theta_\mu) = e^{-\frac{2i\pi}{3}} + e^0 + e^{\frac{2i\pi}{3}} = 0$

$$\widetilde{\Sigma}_0^1(z) = \frac{t^2}{det(z-H_-)} A_- \sum_{\mu=1}^{3} 2\,\mathbf{I} = \frac{6\,t^2}{det(z-H_-)} A_-\ \mathbf{I} \tag{B.23}$$

Where:

$A_- \equiv z - g_-(\theta) - \Delta$

And for the second term:

$\widetilde{\Sigma}_0^2(z): \quad \sum_{\mu=1}^{3} \Big([1+M(\theta_\mu)]\ N\ M(\theta_\mu)\ [1+M(\theta_\mu)]\Big) = N \sum_{\mu=1}^{3} (1+M(\theta_\mu))$

$$+\sum_{\mu=1}^{3} M(\theta_\mu)\, N\, (1+M(\theta_\mu))$$

It is easy too proof:

$N \sum_{\mu=1}^{3} (1+M(\theta_\mu)) = 3\,N$

Since $MN = N^{-1}M$, we have:

$$\sum_{\mu=1}^{3} M(\theta_\mu)\, N\,(1 + M(\theta_\mu)) = N^{-1} \sum_{\mu=1}^{3} M(\theta_\mu)\,(1 + M(\theta_\mu)) = N^{-1} \sum_{\mu=1}^{3} M(\theta_\mu) + M^2(\theta_\mu) = 3N^{-1}$$

We can summarize as following:

$$\widetilde{\Sigma}_0^2(z) = \frac{t^2}{det(z - H_-)}\, f_-(\theta)\ [3N + 3N^{-1}]$$

Again by using of equation (2.40) we have:

$$N + N^{-1} = \begin{pmatrix} e^{i\beta} & 0 \\ 0 & e^{-i\beta} \end{pmatrix} + \begin{pmatrix} e^{-i\beta} & 0 \\ 0 & e^{i\beta} \end{pmatrix} = 2\, cos(\beta)\, \mathbf{I}$$

$\Rightarrow$

$$\widetilde{\Sigma}_0^2(z) = \frac{6t^2}{det(z - H_-)}\, f_-(\theta)\, cos\left(\alpha_-(\theta) + \frac{\pi}{2}\right) \mathbf{I} \tag{B.24}$$

So now we can right a perfect relation for self-energy:

$$\widetilde{\Sigma}_0(z) = \frac{6t^2}{det(z - H_-)}\ \{[z - g_-(\theta) - \Delta] - f_-(\theta)\, sin\,(\alpha_-(\theta))\,\}\, \mathbf{I} \tag{B.25}$$

By introducing of $\widetilde{\Sigma}_0(z) = \sigma(z)\, \mathbf{I}$ we have:

$$\sigma(z) = \frac{6t^2}{det(z - H_-)}\ \{[z - g_-(\theta) - \Delta] - f_-(\theta)\, sin\,(\alpha_-(\theta))\} \tag{B.26}$$

B.4 Calculations of DOS

We start by following equation:

$$\Delta\rho(E,\vec{R},\varepsilon) = -\frac{1}{\pi}\Im\langle\vec{R}\,\varepsilon|\mathcal{G}_0\,\widetilde{\Sigma}\,\mathcal{G}_0|\vec{R}\,\varepsilon\rangle \tag{B.27}$$

$$\mathcal{G}_0\,\widetilde{\Sigma}\,\mathcal{G}_0 = \sum_{j=1}^{6}(\mathcal{P}_j\,\mathcal{G}_0\,\widetilde{\Sigma}\,\mathcal{G}_0\,\mathcal{P}_0 + \mathcal{P}_0\,\mathcal{G}_0\,\widetilde{\Sigma}\,\mathcal{G}_0\,\mathcal{P}_j)$$

$$\Delta\rho(E,\vec{R},\varepsilon) = -\frac{1}{\pi}\Im\ \left\{\langle\vec{R},\varepsilon|\mathcal{P}_j\,\mathcal{G}_0\,\widetilde{\Sigma}\,\mathcal{G}_0\,\mathcal{P}_0 + \mathcal{P}_0\,\mathcal{G}_0\,\widetilde{\Sigma}\,\mathcal{G}_0\,\mathcal{P}_j|\vec{R},\varepsilon\rangle\right\}$$

$$\Im\ \langle\vec{R},\varepsilon|\mathcal{P}_j\,\mathcal{G}_0\,\widetilde{\Sigma}\,\mathcal{G}_0\,\mathcal{P}_0 + \mathcal{P}_0\,\mathcal{G}_0\,\widetilde{\Sigma}\,\mathcal{G}_0\,\mathcal{P}_j|\vec{R},\varepsilon\rangle = -\Im\ \langle\vec{R},\varepsilon|\mathcal{P}_j\,\mathcal{G}_0\,\widetilde{\Sigma}\,\mathcal{G}_0\,\mathcal{P}_0 + \mathcal{P}_0\,\mathcal{G}_0\,\widetilde{\Sigma}\,\mathcal{G}_0\,\mathcal{P}_j|\vec{R},\varepsilon\rangle^*$$
$$= -\Im\ \langle\vec{R},\varepsilon|(\mathcal{P}_j\,\mathcal{G}_0\,\widetilde{\Sigma}\,\mathcal{G}_0\,\mathcal{P}_0 + \mathcal{P}_0\,\mathcal{G}_0\,\widetilde{\Sigma}\,\mathcal{G}_0\,\mathcal{P}_j)^\dagger|\vec{R},\varepsilon\rangle$$

We can write:

$$\Delta\rho(E,\vec{R},\varepsilon) = \sum_{j=1}^{6} -\frac{1}{\pi}\Im\ \left\{\langle\vec{R},\varepsilon|\mathcal{P}_j\,\mathcal{G}_0\,\widetilde{\Sigma}\,\mathcal{G}_0\,\mathcal{P}_0 - \mathcal{P}_j\,{\mathcal{G}_0}^\dagger\ \widetilde{\Sigma}^\dagger\ {\mathcal{G}_0}^\dagger\,\mathcal{P}_0|\vec{R},\varepsilon\rangle\right\}$$

$$= \sum_{j=1}^{6} -\frac{1}{\pi}\Im\ \left\{\langle\vec{R},\varepsilon|\mathcal{P}_j\,(\mathcal{G}_0\,\widetilde{\Sigma}\,\mathcal{G}_0\ -\ {\mathcal{G}_0}^\dagger\ \widetilde{\Sigma}^\dagger\ {\mathcal{G}_0}^\dagger)\,\mathcal{P}_0|\vec{R},\varepsilon\rangle\right\} \tag{B.28}$$

Using the identity

$$\lim_{y\to 0^+}\frac{1}{x\pm iy} = P\frac{1}{x} \mp i\pi\delta(x) \tag{B.29}$$

and

$$\mathcal{G}(\vec{r},\vec{r'};z) = \sum_n \frac{\Phi_n(\vec{r})\ {\Phi_n}^*(\vec{r})}{z-\lambda_n} + \int dc\,\frac{\Phi_n(\vec{r})\ {\Phi_n}^*(\vec{r})}{z-\lambda_c} \tag{B.30}$$

we can express the discontinuity, $\widetilde{\mathcal{G}}(\lambda)$, in terms of delta function

$$\widetilde{\mathcal{G}}(\lambda) \equiv \mathcal{G}^{+}(\lambda) - \mathcal{G}^{-}(\lambda) = -2\pi i \delta(\lambda - L) \tag{B.31}$$

Since L is a hermitian operator, all of its eigenvalues $\{\lambda_n\}$ are real. Hence, if $\Im z \neq 0$, then $z \neq \{\lambda_n\}$, which means that $\mathcal{G}(z)$ is an analytic function in the complex z-plane except at those points or portions of the real z-axis that correspond to the eigenvalues of L.

Now by using of equation (2.46) in (2.43) we have:

$$\Delta\rho(E, \vec{R}, \varepsilon) = -\frac{1}{\pi}\, \Im \sum_{j=1}^{6} \left\{ \langle \vec{R}, \varepsilon | \mathcal{P}_j\, \mathcal{G}_0\, \widetilde{\Sigma}\, (-2i\pi) \delta(E - H)\, \mathcal{P}_0 | \vec{R}, \varepsilon \rangle \right\}$$

$$= 2 \sum_{j=1}^{6} \Re \left\{ \langle \vec{R}, \varepsilon | \mathcal{P}_j\, \mathcal{G}_0\, \widetilde{\Sigma}\, \delta(E - H)\, \mathcal{P}_0 | \vec{R}, \varepsilon \rangle \right\}$$

$$\delta(E - H) = \int \frac{d^2\vec{k}}{(2\pi)^2/S}\, |\Phi(E, \vec{k})\rangle\langle\Phi(E, \vec{k})| = \int \frac{d^2\vec{k}}{(2\pi)^2/S}\, \delta(E - \varepsilon_{\vec{k}})\, |\Phi(\vec{k})\rangle\langle\Phi(\vec{k})| = n(E) \tag{B.32}$$

Finally we have:

$$\Delta\rho(E, \vec{R}, \varepsilon) = 2n(E) \sum_{j=1}^{6} \Re \left\{ e^{i\vec{G}_j \cdot \vec{R}} \langle \varepsilon |\, \mathcal{G}_0(\vec{G}_j)\, \widetilde{\Sigma}\, | \varepsilon \rangle \right\} \tag{B.33}$$

Where:

$$\vec{G}_j = \vec{k}\,\theta \times (\vec{K}_\mu - \vec{K}_\nu) = |\sqrt{3}\, \vec{K}_d\ \theta|\ sgn[\theta(\nu - \mu)]\ \ \vec{v}\,[\frac{\pi}{3}(\mu + \nu)]\,; v(\vec{\theta}) = \vec{u_x} cos\theta + \vec{u_y} sin\theta \tag{B.34}$$

and

$$\theta_\nu = \frac{2\pi}{3}\nu - \frac{\pi}{3} \tag{B.35}$$

$$\widetilde{\Sigma} = H_c(\vec{K}_\mu)\ \mathcal{G}_-(-\vec{k}\,\theta \times \vec{K}_\mu)\, H_c(\vec{K}_\mu)$$

$$\mathcal{G}(-\vec{k}\theta \times \vec{K}_\nu) = -\begin{pmatrix} \Delta & E(\vec{K}_d\theta)e^{i\theta_\nu} \\ E(\vec{K}_d\theta)e^{-i\theta_\nu} & \Delta \end{pmatrix}^{-1}$$

$$\mathcal{G}_+(\vec{G}_j) = -\begin{pmatrix} 0 & E(\vec{G}_j)e^{i\theta_j} \\ E(\vec{G}_j)e^{-i\theta_j} & 0 \end{pmatrix}^{-1} = \frac{1}{E(\vec{G}_j)}\begin{pmatrix} 0 & e^{i\theta_j} \\ e^{-i\theta_j} & 0 \end{pmatrix}$$

in which

$$\theta_j = \frac{\pi}{2} + \theta(\vec{K}_\mu - \vec{K}_\nu) \tag{B.36}$$

it will be nice to have a compact form:

$$\begin{cases} e^{i\theta_j} = e^{i\frac{\pi}{3}(\mu+\nu)}\ sgn[\theta(\nu-\mu)] \\ e^{i\theta_\nu} = -i\, e^{2i\frac{\pi}{3}\nu}\ sgn(\theta) \end{cases} \tag{B.37}$$

Now we are going to continue calculation of variation of DOS:

$$\Delta\rho(E,\vec{R},\varepsilon) = 2n(E)\,\Re\ \sum_{j=1}^{6} e^{i\vec{G}_j\cdot\vec{R}}\langle\varepsilon|\frac{1}{E(\vec{G}_j)}\begin{pmatrix} 0 & e^{i\theta_j} \\ e^{-i\theta_j} & 0 \end{pmatrix} \times t$$

$$\begin{pmatrix} 1 & e^{2i\frac{\pi}{3}\nu} \\ e^{-2i\frac{\pi}{3}\nu} & 1 \end{pmatrix} \times \frac{1}{\Delta^2 - E^2(\vec{K_d}\,\theta)} \times \begin{pmatrix} -\Delta & E(\vec{K_d}\theta)e^{i\theta_\nu} \\ E(\vec{K_d}\,\theta)e^{-i\theta_\nu} & -\Delta \end{pmatrix}^{-1}$$

$$\times t \begin{pmatrix} 1 & e^{2i\frac{\pi}{3}\mu} \\ e^{-2i\frac{\pi}{3}\mu} & 1 \end{pmatrix} |\varepsilon\rangle$$

For simplicity we suppose $\Delta = 0$ and after some computations we have:

$$\Delta\rho(E,\vec{R},\varepsilon) = \frac{2n(E)}{\sqrt{3}} \frac{t^2}{(E(\vec{K_d}\,\theta))^2} \times \sum_{j=1}^{6} \Re\,[e^{i\vec{G_j}\cdot\vec{R}}\ 2\ sgn(\nu-\mu)\ sin(\frac{\pi}{3}(\nu-\mu))]$$

$$\Rightarrow\ \frac{\Delta\rho(E,\vec{R},\varepsilon)}{n(E)} = \frac{2t^2}{(\hbar\,c\,K_d\,\theta)^2} \sum_{j=1}^{6} \Re\,[e^{i\vec{G_j}\cdot\vec{R}}] = \frac{2t^2}{(\hbar\,c\,K_d\,\theta_{rad})^2} \sum_{j=1}^{6} cos(\vec{G_j}\cdot\vec{R})$$

Finally by using of numerical values: $\hbar\,c\,K_d \approx 10eV$ and $t \approx 0.12eV$ we drive final relation for DOS:

$$\Rightarrow\ \frac{\Delta\rho(E,\vec{R},\varepsilon)}{n(E)} \cong \frac{1}{\theta_{deg}^2} \sum_{j=1}^{6} cos(\vec{G_j}\cdot\vec{R}) \tag{B.38}$$

APPENDIX C

Theory of elastic collisions and single scattering

In this appendix, we review, the theory of scattering of a scalar wave by a single localized obstacle described by a potential $V(\boldsymbol{r})$ [1]. Having defined some basic quantities, we consider the scattering of electrons by a spherically symmetric potential barrier [2]. For scalar waves, the main results apply to different wave equations. We shall consider these in the framework of the Helmholtz equation.

Consider the problem of the scattering of a wave by a *localized* potential $V(\boldsymbol{r})$, that is, a potential which obeys the condition $\lim_{r\to+\infty} rV(\boldsymbol{r}) = 0$.We seek solutions to the Helmholtz equation by setting of $\hbar^2/2m = 1$

$$(\nabla^2 + k_0^2)\psi(\boldsymbol{r}) = V(\boldsymbol{r})\psi(\boldsymbol{r})\,, \tag{C.1}$$

which satisfy the boundary condition

$$\psi(\boldsymbol{r}) \propto \frac{e^{ik_0 r}}{r} \quad r \to +\infty\,, \tag{C.2}$$

corresponding to an asymptotically emergent spherical wave. The solutions of (A.1) are obtained from the associated Green function $\mathcal{G}_0(\boldsymbol{r}, \boldsymbol{r}', k_0) = \delta(\boldsymbol{r} - \boldsymbol{r}')$, defined by

$$(\partial_r^2 + k_0^2)\mathcal{G}_0(\boldsymbol{r}, \boldsymbol{r}', k_0) = \delta(\boldsymbol{r} - \boldsymbol{r}')\,, \tag{C.3}$$

such that the general solution of (A.1) may be written as

$$\psi(\boldsymbol{r}) = \int d\boldsymbol{r}' \mathcal{G}_0(\boldsymbol{r}, \boldsymbol{r}', k_0) V(\boldsymbol{r}')\psi(\boldsymbol{r}'), \tag{C.4}$$

To this solution, we may add the solution of the homogeneous equation

$$(\nabla^2 + k_0^2)\,\phi(\boldsymbol{r}) = 0\,, \tag{C.5}$$

which describes the incident wave, which we choose to be a plane wave $\psi(\boldsymbol{r}) = e^{i\boldsymbol{k}\cdot\boldsymbol{r}}$ with $|\boldsymbol{k}| = k_0$. Using expression (Appendix B) for the free Green function:

$$\mathcal{G}_0(\boldsymbol{r}, \boldsymbol{r}', k_0) = -\frac{1}{4\pi}\frac{e^{ik_0|\boldsymbol{r}-\boldsymbol{r}'|}}{|\boldsymbol{r} - \boldsymbol{r}'|}\,, \tag{C.6}$$

we obtain

$$\psi(\boldsymbol{r}) = e^{i\boldsymbol{k}\cdot\mathbf{r}} - \frac{1}{4\pi}\int dr' \frac{e^{ik_0|\boldsymbol{r}-\boldsymbol{r}'|}}{|\boldsymbol{r} - \boldsymbol{r}'|} V(\boldsymbol{r}')\psi(\boldsymbol{r}')\,. \tag{C.7}$$

Asymptotic form of the solutions

In order to study the asymptotic form ($r \to \infty$) of the solution (A.7), we write, for

$r \gg r'$ (Figure A.1)

$$k_0|\boldsymbol{r} - \boldsymbol{r}'| = k_0 r \sqrt{1 + (\frac{r'}{r})^2 - 2\frac{\boldsymbol{r}\cdot\boldsymbol{r}'}{r^2}} \approx k_0 r - \boldsymbol{k}' \cdot \boldsymbol{r}' \,. \tag{C.8}$$

where $\boldsymbol{k}' = k_0\boldsymbol{r}/r$.We thus obtain an approximate form for the free Green function (known as the Fraunhoffer approximation),

$$\mathcal{G}_0(\boldsymbol{r}, \boldsymbol{r}', k_0) \approx -\frac{e^{ik_0 r}}{4\pi r} e^{-i\boldsymbol{k}'\cdot\boldsymbol{r}'} \,, \tag{C.9}$$

which we substitute into (A.6):

$$\psi(\boldsymbol{r}) \approx e^{i\boldsymbol{k}\cdot\mathbf{r}} - \frac{e^{ik_0 r}}{4\pi r} \int d\boldsymbol{r}' e^{-i\boldsymbol{k}'\cdot\boldsymbol{r}'} V(\boldsymbol{r}')\psi(\boldsymbol{r}') \,. \tag{C.10}$$

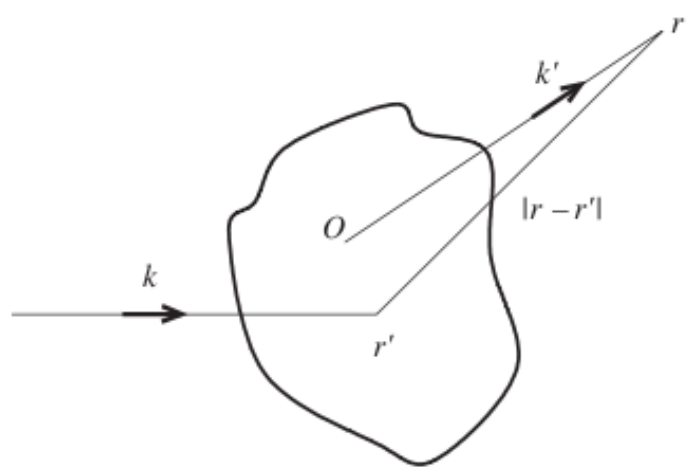

Figure C.1: Scattered wave after interaction with the potential at point $\boldsymbol{r}'$. In the Fraunhoffer approximation, we have $|\boldsymbol{r}'| \ll |\boldsymbol{r}|$.

Written in the form

$$\psi(\boldsymbol{r}) = e^{i\boldsymbol{k}\cdot\mathbf{r}} + \frac{e^{ik_0 r}}{r} f(\boldsymbol{k}, \boldsymbol{k}') \,. \tag{C.11}$$

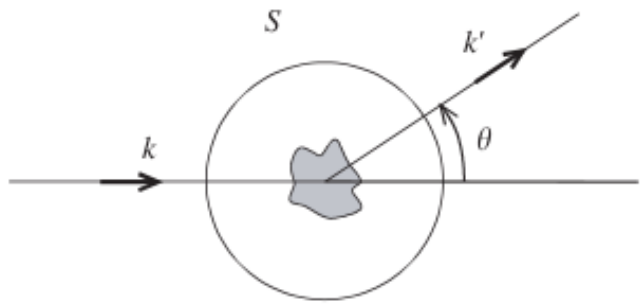

Figure C.2: Scattering by a localized potential. The total flux $F = F_{int} + F_{out} + F_s$ crossing the surface S is zero. Since $F_{in} = \int \boldsymbol{k} \cdot dS = 0$ must vanish. This result constitutes the optical theorem [adopted form [1]] .

this relation defines the *scattering amplitude*

$$f(\boldsymbol{k}, \boldsymbol{k}') = -\frac{1}{4\pi} \int d\boldsymbol{r}' e^{-i\boldsymbol{k}'\cdot\boldsymbol{r}'} V(\boldsymbol{r}')\psi(\boldsymbol{r}') \,. \tag{C.12}$$

which has the dimensions of a length. Since the modulus k_0 of the wave vector $\boldsymbol{k}$ is conserved in an elastic collision, the scattering amplitude only depends on $k_0 = |\boldsymbol{k}| = |\boldsymbol{k}'|$ and on the scattering angle θ between the directions $\boldsymbol{k}$ and $\boldsymbol{k}'$ (Figure A.2), hence $f(\boldsymbol{k}, \boldsymbol{k}') = f(k_0, \theta)$. The expression (A.12) for the scattering amplitude has been defined for the Helmholtz equation. For the Schrödinger equation with a potential $V(\boldsymbol{r})$, it takes the equivalent form:

$$f(\boldsymbol{k}, \boldsymbol{k}') = -\frac{m}{2\pi\hbar^2} \int d\boldsymbol{r}' e^{-i\boldsymbol{k}'\cdot\boldsymbol{r}'} V(\boldsymbol{r}')\psi(\boldsymbol{r}') \,. \tag{C.13}$$

In the *low energy* limit, that is, for $k_0 r_0 \ll 1$ where r_0 is the range of the potential $V(\boldsymbol{r})$, the phase factor of equation (A.12) may be taken equal to 1, and the scattering amplitude is independent of $\boldsymbol{k'}$: *the scattering is isotropic*.We thus define the *scattering length* a_s by the limit

$$a_s = -\lim_{k_0 \to 0} f(\boldsymbol{k}, \boldsymbol{k'}) \,. \tag{C.14}$$

or equivalently,

$$a_s = \frac{1}{4\pi} \int d\boldsymbol{r'} V(\boldsymbol{r'}) \psi(\boldsymbol{r'}) \,. \tag{C.15}$$

Scattering cross section and scattered flux

Starting with a function $\psi(\boldsymbol{r})$ solution of the Helmholtz equation (A.1), we define the flux associated with the current through a surface S by the expression (Figure A.2):

$$F = \Im \int d\boldsymbol{S} \cdot \psi^*(\boldsymbol{r}) \partial^2 \psi(\boldsymbol{r}) \,. \tag{C.16}$$

For an incident flux on the potential $V(\boldsymbol{r})$, we measure the emergent flux in a given direction, characterized by an angle θ, in an element of solid angle $d\Omega$. More precisely, we define the *differential scattering cross section* by the ratio between the flux emerging in an element of solid angle $d\Omega$ and the incident flux per unit surface:

$$\sigma(\theta) = \frac{dF_{out}/d\Omega}{dF_{int}/dS} \,. \tag{C.17}$$

This relation is quite general, and applies to other types of waves.3 The normalization of the flux in equation (A.16) contains a prefactor which depends on the specific physical problem we consider. For a quantum particle whose evolution is governed by the Schrödinger equation, the flux is defined through the probability amplitude [economu book]. The differential scattering cross section thus describes the ratio between the number of particles scattered in a solid angle $d\Omega$ and the incident particle flux per unit surface. In the case of an electromagnetic field, we may use this definition of the scattering cross section where F describes the energy flux $nc\hbar\omega$ of photons, and where n is the photon density [46]. In the classical limit, this is the flux of the Poynting vector.

From expression (A.11), we deduce that the incident flux per unit surface equals $dF_{int}/dS = k_0$. The total flux of the scattered wave is

$$F_{out} = \Im \int d\boldsymbol{S} \cdot f^*(k_0, \theta) \frac{e^{ik_0 r}}{r} \partial^2 \Big[f(k_0, \theta) \frac{e^{ik_0 r}}{r} \Big] . \tag{C.18}$$

which, for large distances ($k_0 r \gg 1$), becomes

$$F_{out} = 2\pi k_0 \int_0^2 |f(k_0, \theta)|^2 \sin\theta \, d\theta . \tag{C.19}$$

so that the differential scattering cross section in the direction θ is equal to the square of the modulus of the scattering amplitude:

$$\sigma(\theta) = |f(k_0, \theta)|^2 . \tag{C.20}$$

We define the total scattering cross section

$$\sigma = 2\pi \int_0^\pi \sigma(\theta)\ \sin\theta\, d\theta\,. \tag{C.21}$$

which is related by (A.19) to the total scattered flux F_{out}in all directions:

$$F_{out} = k_0\sigma\,. \tag{C.22}$$

In the low energy limit, the scattering amplitude has no angular dependence, and the total scattering cross section may be written in terms of the scattering length (A.14):

$$\sigma = 4\pi {a_s}^2\,. \tag{C.23}$$

We also define the transport scattering cross section σ^* which measures the flux projected along the direction of the incident wave, which is

$$\sigma^* = 2\pi \int_0^\pi \sigma(\theta)(1-\cos\theta)\sin\theta\, d\theta\,. \tag{C.24}$$

The scattering cross sections σ and σ^* are equal if the differential scattering cross section has no angular dependence. The transport scattering cross section σ^* plays an important role in multiple scattering since it is related to the diffusion coefficient.

Scattering matrix and optical theorem

Define first the scattering operator or $\mathcal{S} - matrix$ which relates the incident $|\psi_{in}\rangle$ and emergent $|\psi_{out}\rangle$ states(here we will use $\hbar^2/2m = 1$):

$$|\psi_{out}\rangle = \mathcal{S}|\psi_{in}\rangle\,. \tag{C.25}$$

The incident state $|\psi_{in}\rangle|\boldsymbol{k}\rangle$ is an eigenstate of the free Hamiltonian $\mathcal{H}_0 = \partial^2$, of energy $E = k_0^2$, that is,

$$\mathcal{H}_0|\psi_{out}\rangle = E|\psi_{in}\rangle\,. \tag{C.26}$$

The emergent state $|\psi_{out}\rangle =$ is an eigenstate of the total Hamiltonian $\mathcal{H} = \mathcal{H}_0 + V$ with the same energy, namely

$$\mathcal{H}|\psi_{in}\rangle = E|\psi_{out}\rangle\,. \tag{C.27}$$

At infinity, the two states $|\psi_{in}\rangle$ and $|\psi_{out}\rangle$ only differ by the scattered wave, whose amplitude tends to zero. As a consequence, the two states are identical up to a phase difference. Subtracting equations (A.26) and (A.27) and using the definition (A.25) of the $\mathcal{S} - matrix$, we obtain

$$V\mathcal{S} = (E - \mathcal{H}_0)(\mathcal{S} - \mathbb{1})\,. \tag{C.28}$$

which yields $\mathcal{S} = \mathbb{1}$ for$V = 0$. Using the resolvant operator $\mathcal{G}_0$ associated with the free problem and defined by $(E - \mathcal{H}_0)\mathcal{G}_0 = \mathbb{1}$, we can rewrite a Dyson equation:

$$\mathcal{S} = \mathbb{1} + \mathcal{G}_0 V\mathcal{S}\,. \tag{C.29}$$

Projecting this equation on an incident state $|\boldsymbol{k}\rangle$ we recover relation (A.7) in the form

$$|\psi_{out}\rangle = |\boldsymbol{k}\rangle + \mathcal{G}_0 V|\psi_{out}\rangle\,. \tag{C.30}$$

Let us now define the *scattering operator* $T = V\mathcal{S}$ which satisfies what is known as the Lippman-Schwinger equation:

$$|\psi_{out}\rangle = (\mathbb{1} + \mathcal{G}_0 T)|\psi_{in}\rangle\,. \tag{C.31}$$

Applying this equality to the state $|\boldsymbol{k}\rangle$, we obtain

$$|\psi_{out}\rangle = |\boldsymbol{k}\rangle + \mathcal{G}_0 T|\boldsymbol{k}\rangle\,. \tag{C.32}$$

whose projection on $|\boldsymbol{r}\rangle$ yields equation (A.7). Indeed, by using the closure relation, we get

$$\langle \boldsymbol{r}|\psi_{out}\rangle = e^{i\boldsymbol{k}\cdot\boldsymbol{r}} + \int d\boldsymbol{r}'\langle \boldsymbol{r}|\mathcal{G}_0|\boldsymbol{r}'\rangle\langle \boldsymbol{r}'|T|\boldsymbol{k}\rangle\,. \tag{C.33}$$

and the asymptotic expansion (A.9) of $\langle \boldsymbol{r}|\mathcal{G}_0|\boldsymbol{r}'\rangle$ leads to (A.11) with

$$f(|\boldsymbol{k},\boldsymbol{k}'\rangle) = -\frac{1}{4\pi}\langle \boldsymbol{k}'|T|\boldsymbol{k}\rangle\,. \tag{C.34}$$

To derive the optical theorem, we start with the Lippman-Schwinger equation (A.32). Multiplying by $T^\dagger$ and projecting on the state $\boldsymbol{k}$, we obtain for the imaginary part

$$\Im\langle \boldsymbol{k}|T^\dagger|\boldsymbol{k}\rangle = -\Im\langle \boldsymbol{k}|T^\dagger \mathcal{G}_0 T|\boldsymbol{k}\rangle\,. \tag{C.35}$$

since $\Im\langle\psi_{out}|V|\psi_{out}\rangle = 0$. Then

$$\Im\langle \boldsymbol{k}|T^{\dagger}|\boldsymbol{k}\rangle = \frac{\pi}{2k_0}\sum_{\boldsymbol{k}'}|\langle \boldsymbol{k}'|T|\boldsymbol{k}\rangle|^2\delta(k'-k_0)\,. \tag{C.36}$$

or

$$-\Im\langle \boldsymbol{k}|T|\boldsymbol{k}\rangle = \frac{k_0}{8\pi}\int_0^{\pi}|\langle \boldsymbol{k}'|T|\boldsymbol{k}\rangle|^2\sin\theta\, d\theta\,. \tag{C.37}$$

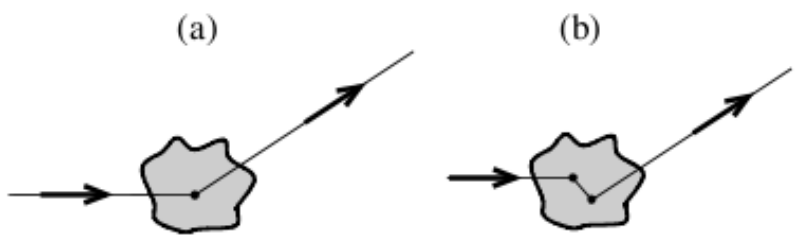

Figure C.3: (a) In the Born approximation, the wave interacts with the potential only once. (b) Beyond this approximation, the wave is scattered many times by the potential .

Finally, from (A.21) and (A.34), we deduce that

$$\sigma = \frac{4\pi}{k_0}\Im f(\theta=0) = -\frac{1}{k_0}\Im\langle \boldsymbol{k}|T|\boldsymbol{k}\rangle\,. \tag{C.38}$$

which is the optical theorem $\sigma = \frac{4\pi}{k_0}\Im f(k_0,\theta=0)$.

Bibliography

[1] Eric Akkermans, Gilles Montambaux.: *Mesoscopic Physics of Electrons and Photons*; Cambridge University (2007)

[2] Eleftherios N. Economou.: *Green's Functions in Quantum Physics*, (Springer Series in Solid-State Sciences), 3rd edition (2006)

Abstract

Graphene, a material made of a one-atom-thick carbon layer, is a major topic of modern condensed-matter research. Graphene exhibits exciting properties such as massless Dirac electronic structure, high mobility anomalous quantum Hall effects, strength, stiffness and extraordinary high thermal conductivity. This thesis deals with electronic structure and transport properties of graphene.

We consider in particular the case of twisted bilayers of graphene. These systems have been discovered especially in graphene produced on Silicon Carbide and present original properties when compared with standard AB bilayers that occur for example in graphite. We analyze by perturbative theory and by numerical methods the density of states. We show that the electronic density of states presents periodic oscillations with the period of the geometric Moir produced by these systems. We analyze also the role of defects on transport properties and in particular we consider the case where the defects are on one layer only : the layer exposed to the air. We show how defects on this layer affects the conductivity of the bilayer. Here also we use simple analytical models and numerical approaches.

We consider also the role played by atomic impurities like Hydrogen adatom on the graphene plane. We analyze the modification of density of states induced around the adatom and the corresponding modifications of charge density and electrostatic potential. These systems tend to produce a resonant state close to the Dirac energy which depends much on whether the adatom is in a top or hollow position. For hydrogen like orbital (s orbital) the resonance is stronger in the hollow position. We show that the image obtained

through STM experiments for these resonant state depends very much on the distance of the STM tip to the adatom. In a near field regime the resonance can even appear as a dip in the STM signal dI/dV.

Résumé

Le graphène est un matériau constitué d'une seule couche atomique de carbone et représente un sujet majeur de la physique de la matière condensée. Le graphène possède de nombreuses propriétés remarquables : structure électronique décrite par une equation de Dirac sans masse, forte mobilité électronique, effet Hall quantique anormal, résistance, rigidité et conductivité thermique élevée. Cette these concerne la structure électronique et le transport dans le graphène.

Nous considérons en particulier le cas des bicouches tournées de graphène. Ces systèmes ont été découverts en particulier dans le graphène produit sur le carbure de silicium et pré sentent des propriété s originales par rapport aux bicouches dans l'empilement AB qui existe par exemple dans le graphite. Nous analysons au moyen d'une théorie perturbative et aussi par des approches numé riques la densité d'états dans ces systé mes. Nous montrons que la densité d'états pré sente des oscillations avec la même période que celle du Moiré produit par ces bicouches. Nous analysons aussi le rôle des défauts sur les propriétés de transport en particulier dans le cas ou les défauts sont répartis uniquement sur une des deux couches. Ici aussi notre approche combine théorie perturbative du couplage interplans et approches purement numérique en liaisons fortes.

Nous considérons aussi le role joué par les adatomes comme l'hydrogène par exemple. Nous analysons la modification de la densité d'états induite autour de l'adatome et les variations correspondantes de densité de charge et de potentiel électrostatique. Ces systémes tendent à produire des états resonants pr és de l' énergie de Dirac qui dependent beaucoup aussi de la position top ou hollow de l' adsorbat. Pour des orbitales de type "s" la resonance est plus marquée si l'adatome est en position hollow. Nous montrons que l'image par experience STM (microscopie à effet tunnel) depend beaucoup de la distance entre l'adsorbat et la pointe du STM. Dans un régime de champ proche la résonance de l'adsorbat peut même apparaître comme un creux dans le signal dI/dV du STM.

Résumé

Le graphène est un matériau constitué d'une seule couche atomique de carbone et représente un sujet majeur de la physique de la matière condensée. Le graphène possède de nombreuses propriétés remarquables : structure électronique décrite par une equation de Dirac sans masse, forte mobilité électronique, effet Hall quantique anormal, résistance, rigidité et conductivité thermique élevée. Cette these concerne la structure électronique et le transport dans le graphène.

Nous considérons en particulier le cas des bicouches tournées de graphène. Ces systèmes ont été découverts en particulier dans le graphène produit sur le carbure de silicium et pré sentent des propriété s originales par rapport aux bicouches dans l'empilement AB qui existe par exemple dans le graphite. Nous analysons au moyen d'une théorie perturbative et aussi par des approches numé riques la densité d'états dans ces systé mes. Nous montrons que la densité d'états pré sente des oscillations avec la même période que celle du Moiré produit par ces bicouches. Nous analysons aussi le rôle des défauts sur les propriétés de transport en particulier dans le cas ou les défauts sont répartis uniquement sur une des deux couches. Ici aussi notre approche combine théorie perturbative du couplage interplans et approches purement numérique en liaisons fortes.

Nous considérons aussi le role joué par les adatomes comme l'hydrogène par exemple. Nous analysons la modification de la densité d'états induite autour de l'adatome et les variations correspondantes de densité de charge et de potentiel électrostatique. Ces systémes tendent à produire des états resonants pr és de l' énergie de Dirac qui dependent beaucoup aussi de la position top ou hollow de l' adsorbat. Pour des orbitales de type "s" la resonance est plus marquée si l'adatome est en position hollow. Nous montrons que l'image par experience STM (microscopie à effet tunnel) depend beaucoup de la distance entre l'adsorbat et la pointe du STM. Dans un régime de champ proche la résonance de l'adsorbat peut même apparaître comme un creux dans le signal dI/dV du STM.